Copyright
by
Yiwei Wang
2013

The Dissertation Committee for Yiwei Wang
certifies that this is the approved version of the following dissertation:

Effects of Intermetallic Compound Formation on Reliability of Pb-Free Sn-Based Solders for Flip Chip and Three-Dimensional Interconnects

Committee:

Paul S. Ho, Supervisor

Llewellyn K. Rabenberg

Rui Huang

Jang-Hi Im

Minhua Lu

Effects of Intermetallic Compound Formation on Reliability of Pb-Free Sn-Based Solders for Flip Chip and Three-Dimensional Interconnects

by

Yiwei Wang, B.E.; M.S.E.

DISSERTATION

Presented to the Faculty of the Graduate School of

The University of Texas at Austin

in Partial Fulfillment

of the Requirements

for the Degree of

DOCTOR OF PHILOSOPHY

THE UNIVERSITY OF TEXAS AT AUSTIN

December 2013

To my family

Acknowledgments

First, My thanks go to my dissertation committee: Prof. Paul Ho, Prof. Llewellyn Rabenberg, Prof. Rui Huang, Dr. Jang-Hi Im, and Dr. Minhua Lu. I would like to express my deep gratitude towards my adviser, Prof. Paul Ho for his initiation, guidance, and support during my years at the University of Texas at Austin. I want to thank Prof. Rui Huang, who has introduced me to the challenging and interesting field of mechanics and offered tremendous help in the formulation of the kinetic analysis. The experimental data for the kinetics study reported in this dissertation were provided by Dr. Minhua Lu from IBM. I also want to thank Minhua for her insightful discussion and for pointing me to many papers related to my research. I greatly appreciate Prof. Llewellyn Rabenberg for teaching me structure of materials and for his instructive suggestions on my dissertation. Special thanks goes to Dr. Jang-Hi Im who has helped me tremendously in many aspects of my research.

I truly appreciate the generous support from Texas Instruments on the electromigration work. Most importantly, Dr. Seung-Hyun Chae has provided constant guidance and support towards the completion of the project. He was always willing to spend extra time discussing details of the experimental results.

I want to acknowledge the members from the Interconnect and Packaging group for helpful discussions and support. At the initial stages of my studies, the help from Dr. Kuan-Hsun Lu was indispensable. I learned from him the experimental skills for electromigration reliability testing. I also want to thank Dr. Huang-Lin Chao for helping me out on understanding the simulated annealing method. Thanks also goes to Jo Ann Smith, who has helped me patiently on various administrative matters.

Last but not least, I am deeply indebted to my parents, Maogong Wang and Yuhua Jin, who have provided boundless love and unconditional support. Their encouragement has given me the strength and freedom to pursue my goal. I would also like to thank my husband, Yihua Chen, for his love, support and inspiring discussions on research.

Effects of Intermetallic Compound Formation on Reliability of Pb-Free Sn-Based Solders for Flip Chip and Three-Dimensional Interconnects

Publication No. _____

Yiwei Wang, Ph.D.
The University of Texas at Austin, 2013

Supervisor: Paul S. Ho

The effects of intermetallic compound (IMC) formation on reliability of Pb-free Sn-based solders for flip chip and three-dimensional (3D) interconnects were studied. The dissertation is organized into four parts. In the first part, the effect of Sn grain orientation on electromigration (EM) reliability of Pb-free Sn-based flip chip solder joints was studied. The Sn grain microstructure in flip chip solder joints was characterized using the electron backscatter diffraction (EBSD) technique, and was found to be closely related to the EM failure mechanisms. The approach to grain structure optimization for improved EM reliability was also explored. In addition to the experimental work, a kinetic analysis was formulated to investigate the early EM degradation mechanism in Sn-based solder joints with Ni under-bump metallization (UBM).

In the aforementioned kinetic analysis, the intrinsic diffusion coefficients were not readily available in the literature. In the second part of the work, a Monte Carlo method known as simulated annealing was applied to estimate the unknown diffusion coefficients using a multi-parameter optimization method by fitting to experimental measurements. The intrinsic diffusion coefficients of Ni and Sn in Ni_3Sn_4 between 150 and 200°C, and those of Cu and Sn in Cu_3Sn and Cu_6Sn_5 between 120 and 200°C were estimated. The activation energies for these diffusion coefficients were also determined. Together, this provides the diffusivity parameters to predict the intermetallic growth as a function of temperature.

The third objective focused on the EM reliability of Sn-based microbump joints in 3D interconnects with through-silicon vias (TSVs). No EM-induced bump failure was observed, showing a robust EM reliability in microbumps. High temperature thermal annealing test was also performed on microbumps with three different metallizations in an effort to explore structural and process optimization.

Finally, interfacial reaction induced stress in IMC microbumps was investigated. A numerical analysis was formulated to study the concurrent diffusion, phase transformation, and deformation in the process of IMC formation. Stress generation due to unbalanced diffusion rates and volumetric change upon phase transformation was considered. The coupled analysis was applied to investigate Ni_3Sn_4 growth in the Ni-Sn microbumping system. A simulation approach based on finite difference method with

moving boundaries was employed to numerically solve the stress evolution in Ni_3Sn_4. The equilibrium stress was also investigated using a modified model with a finite thickness of solder. Simulation predictions were found to be in good qualitative agreement with experimental observations.

Table of Contents

List of Tables

List of Figures

Chapter 1

Introduction

The number of transistors per chip that yields the minimum cost per transistor has increased at a rate of roughly a factor of two per year.

Gordon Moore

In the past four decades, the microelectronics industry has mainly been driven by Moore's law, which states that the number of transistors on integrated circuits (ICs) doubles approximately every two years. The transistor count increased from 2,300 in 1971 to 2.5 billion in 2012 (Fig. 1.1). Moore's law has an immediate impact on the packaging technology. This has led to the formulation of the Rent's rule [2] which provides an estimation of the number of terminal pins, T, by knowing the transistor counts,

$$T = tg^p \tag{1.1}$$

where g is the number of internal components, t and p are the constants ($p < 1.0$, and generally $0.5 < p < 0.8$). As the number of transistor increases, the number of interconnects between the die and the package increases. This has led to flip chip technology that substantially outstrips the conventional wire bonding in form factor, input/output (I/O) density, and bus speed.

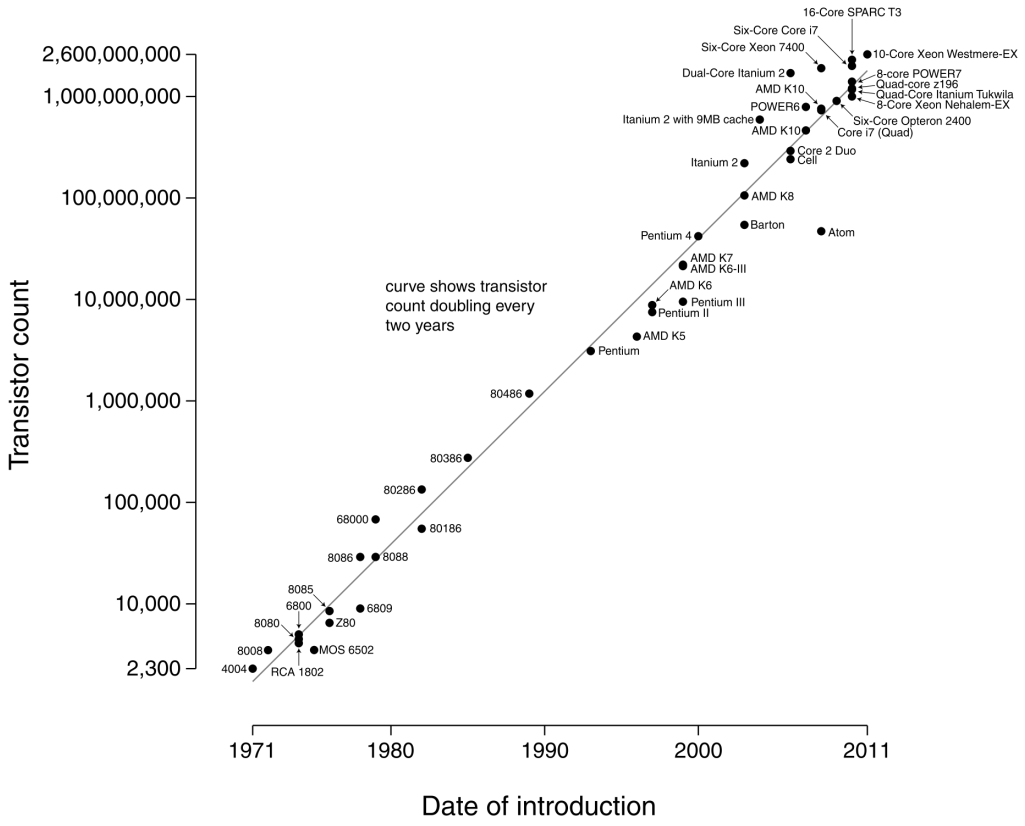

Figure 1.1: Microprocessor transistor counts against dates of introduction [1].

However, the scaling of the transistor size and thus transistor count per die are bounded by quantum physical effects. As the trend of device miniaturization on the silicon technology is approaching the limit of Moore's law, packaging innovations offer an alternative route. In recent years, three-dimensional (3D) integration incorporating through-silicon vias (TSVs) has emerged as an effective approach to overcome the wiring limit beyond 32 nm node.

Whether in flip chip technology or 3D integration, Sn-based solder joints are commonly used as die-to-substrate, die-to-die, or die-to-interposer interconnection. In this chapter, a brief overview of flip chip technology, 3D integration, and reliability challenges in solder joints are reviewed, and research objectives and approaches for this dissertation are described.

1.1 Flip Chip Technology

The flip chip technology was first introduced by IBM in 1964 for ceramic substrates, and is also known as the Controlled Collapse Chip Connection (C4) [85]. This process uses solder bumps as the first-level interconnection to electrically connect the die to the package carrier.

Figure 1.2 schematically shows the process sequence of flip chip bumping. An under-bump metalization (UBM) layer is first deposited on the wafer (Fig. 1.2 (a)). The UBM needs to provide several functions such as good adhesion, good diffusion barrier, and solder wetability. The next step

is the solder bumping process (Fig. 1.2 (b)). Solder bumping methods include evaporation, electroplating, and stencil printing. Which method to use depends on the size and material of the solders to be deposited for specific applications. Followed is a solder reflow process, during which spherical solder balls are formed due to the high surface tension of solder (Fig. 1.2 (c)). The bumped wafer is then diced and ready to be joined to a pre-solder laminate substrate (Figs. 1.2 (d) and (e)). During the laminate joining, both the solder on the laminate and the solder in the chip are melted and combined under reflow temperature. Lastly, underfill materials are dispensed and cured to fill the gap between the chip and the organic carrier as shown in Figure 1.2 (f). Underfill is an encapsulant used to reinforce the solder joints and relieve stresses induced by the mismatch of coefficient of thermal expansion (CTE) between the chip and the organic carrier.

1.2 3D Integration

3D integration, in which two or more chips are stacked vertically, is a well accepted approach to overcome the performance bottleneck and simultaneously shrink the form factor. Key technology elements in 3D integration include [65]: (i) TSVs with thinned silicon wafers, (ii) fine pitch wiring or signal redistribution, (iii) fine pitch silicon to silicon interconnections, (iv) fine pitch test for known-good die (KGD) and (v) power delivery, distribution and thermal cooling solutions. These new technologies offer the ability to reduce circuit to circuit interconnection length, improve power efficiency

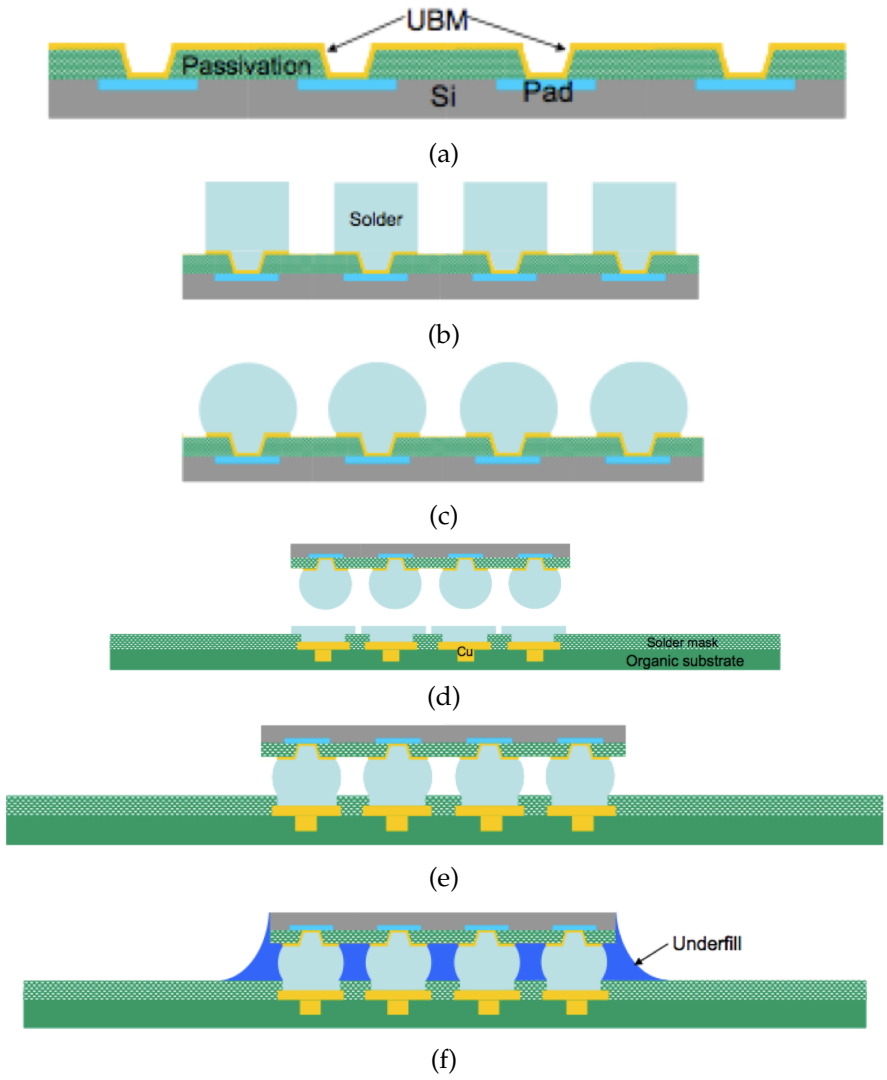

Figure 1.2: Schematic of flip chip packaging assembly process [116]: (a) wafer repassivation and UBM deposition; (b) bumping; (c) solder reflow; (d) and (e) laminate joining; (f) underfill encapsulation.

and provide higher bandwidth similar to on-chip interconnection.

1.2.1 Applications

Although the advantages of 3D TSV technology are widely accepted, mass production of commercial 3D IC products is not expected until manufacturing costs are reduced and reliability issues are solved. Among various potential applications, CMOS image sensors for mobile phones become the first industrial application using the TSV technology [47, 27] mainly driven by form factor. 3D stacking of memory chips has also been developed [90, 62], as shown in Fig. 1.3 as an example. Applying 3D TSV technology to wide I/O memory on logic devices can benefit from lower power consumption, higher data bandwidth, and smaller form factor [90]. Figure 1.4 shows two structures under development, one with chips on a silicon interposer, also known as 2.5D integration, while the other with a memory chip sitting on a microprocessor. Other applications include MEMS and sensors, power, analog and RF devices, LED modules, and logic and analog integration. The ultimate goal of 3D integration is to repartition ICs to realize heterogeneous integration. Figure 1.5 shows the global roadmap for 3D integration as predicted by Yole Development.

1.2.2 3D Integration Process Flow

Figure 1.6 shows a typical process flow of 3D integration using TSV via middle processing, where TSVs are fabricated from the active device

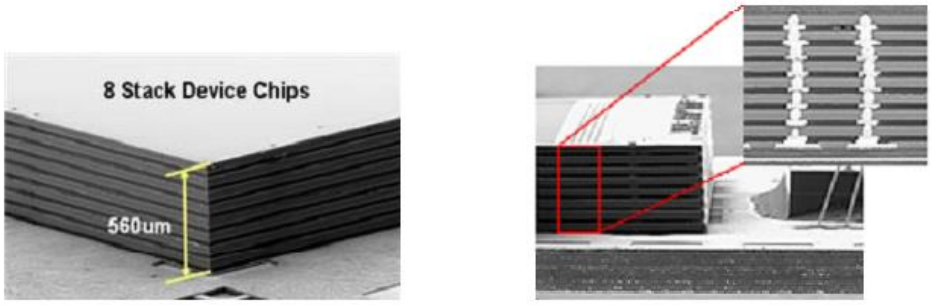

Figure 1.3: Samsung [24] demonstrated high density memory chips using TSV technology.

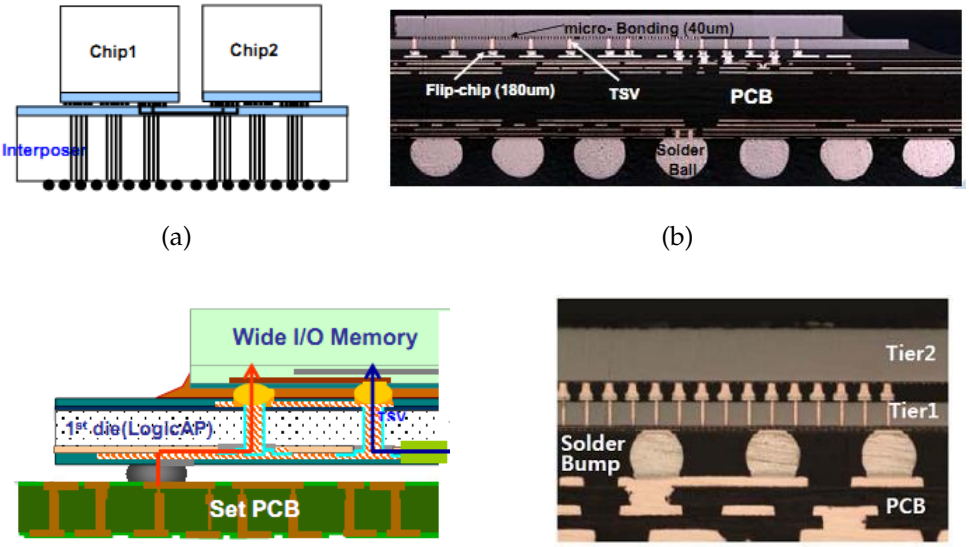

(a) (b)

(c) (d)

Figure 1.4: TSV technology for system on chip (SoC) applications [24]: (a) & (b) chip on interposer; (c) & (d) memory on logic.

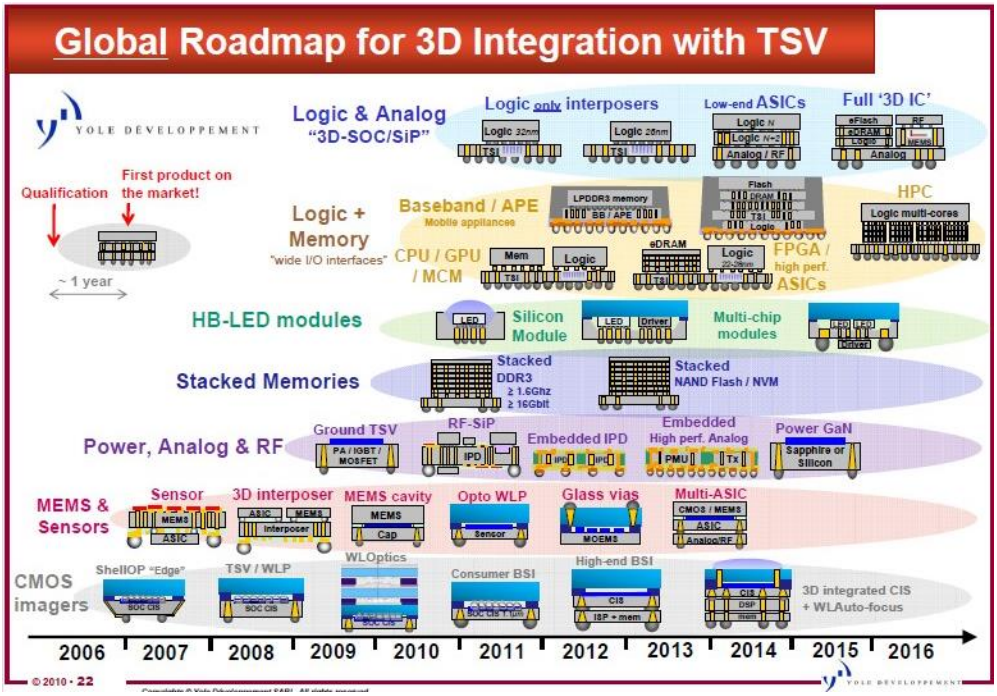

Figure 1.5: Roadmap for 3D integration with TSVs [3].

side right after the contact formation and before the formation of back-end-of-line (BEOL) damascene interconnects. There's also the option of via last processing where TSVs are created after the BEOL interconnects are formed. The choice between via middle and via last flow is mainly driven by device design and process considerations [66]. As illustrated in Fig. 1.6, after TSVs are formed at the device side of a full thickness wafer, the wafer is attached to a carrier wafer and thinned down from the back side to expose the TSV on the other side. It then goes through backside passivation, redistribution layer formation and Cu or Cu/Sn microbump deposition. The wafer is then aligned and bonded to a second wafer using Cu-Cu bonding or Cu/Sn microbump solder bonding. Finally, the carrier wafer is removed.

1.3 From Flip Chip Solder Joints to 3D IC Microbumps

Solder joints have long been used in electronic packages as first-level interconnects. Recently, Sn-based Pb-free solders have been adopted to replace the Pb-based solders following the Europe Union Directive for Reduction of Hazardous Substances [31] due to environmental concerns. The size of a flip chip solder joint is about 80 to 100 μm in diameter. As the packaging technology is advanced to 3D integration, the Sn-based microbumps that are used to stack Si chips are significantly reduced in size. Currently the diameter of microbumps in 3D ICs are 20 μm, and the size is projected to be further reduced in order to increase the I/O density [104]. However, other parameters, such as bonding temperature, times of reflow, UBM thick-

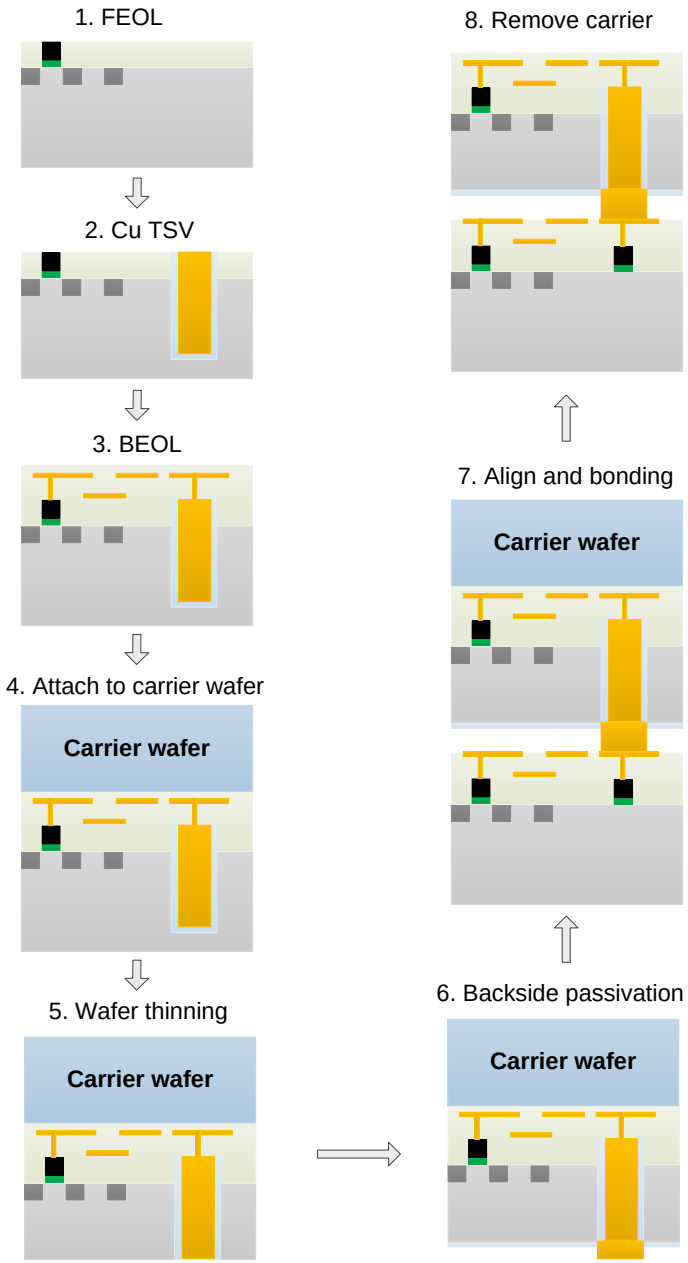

Figure 1.6: Illustration of 3D integration process flow using TSV via middle processing.

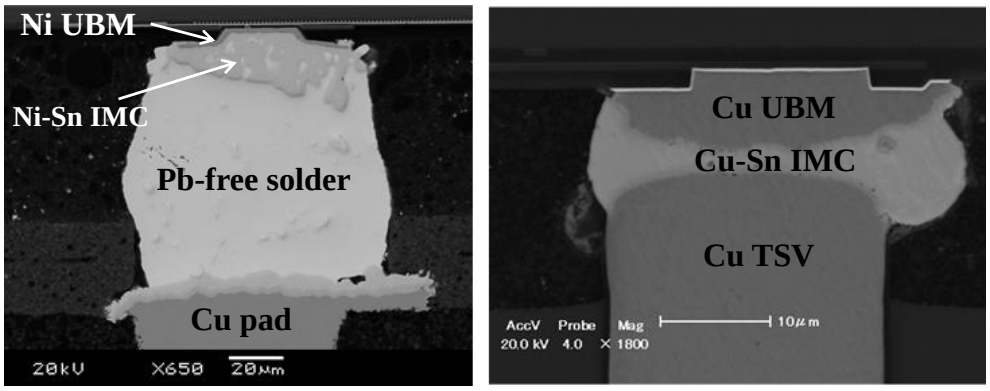

(a) (b)

Figure 1.7: SEM images of (a) a flip chip solder joint with Ni UBM under current stressing, and (b) a TSV microbump joint with Cu UBM.

ness, etc., remain largely unchanged [104], which leads to a more extensive intermetallic compound (IMC) formation compared with that in the conventional flip chip solder joints. Figure 1.7 shows the difference in configuration between a flip chip solder joint and a 3D IC microbump joint. The flip chip solder joint is mainly composed of Pb-free solder, while the microbump has no Sn left as shown in Fig. 1.7(b), where the entire bump is converted into IMC after the assembly. Since the physical properties of IMCs are very different from Pb-free solders, the reliability issues associated with the microbumps could be different from flip chip solder joints, and have to be reassessed.

1.3.1 Pb-based vs. Pb-free Solders

The Pb-free solder joints that have been widely implemented by the industry are Sn-based alloys with minor alloying elements [60]. These include binary eutectic solders, Sn-Cu or Sn-Ag, and ternary Sn-Ag-Cu solder systems [97]. Other minor alloying elements such as Bi, In, Sb, and Zn have also been proposed [14] in an effort to improve the mechanical integrity and mitigate the reliability risks of the solder joints.

Removing Pb changes the physical properties of the solder, which leads to different reliability concerns for the Pb-free solder joints. First, Pb provides the ductility of the solder, as evidenced by the Young's modulus of eutectic Sn-37Pb solder being 35 GPa, compared to 56 GPa for the Sn-3.5Ag solder [80]. Second, the Pb-free solders have a higher melting point than that of eutectic SnPb solders. The melting temperature of Pb-free solders are compared with the eutectic SnPb solder in Table 1.1. This requires a higher reflow temperature of Pb-free packages and increases the dissolution rate of Cu and Ni in the molten solder. Third, Sn has a body-centered tetragonal crystal structure, and hence many of its properties are anisotropic. Finally, the higher Sn content in Pb-free solders increases the amount of IMC formation with under-bump metals and alloying elements.

1.3.2 Intermetallic Compound Formation

During the joining process when solder joints are melted, the solder materials react with UBM and the surface metallization. The interfacial

Table 1.1: Melting temperature of Pb-free and eutectic SnPb solders [97].

Composition (wt%)	Melting temperature (°C)
Sn-0.7Cu	227
Cu-3.5Ag	221
Cu-3.5Ag-3Bi	208-215
Cu-3.0Ag-0.5Cu (SAC305)	217
Cu-3.8Ag-0.7Cu (SAC3807)	217
Cu-3.9Ag-0.6Cu (SAC3906)	217
Cu-3.0Ag-0.9Cu (SAC309)	217
Sn-37Pb (eutectic)	183

reactions continue during testing and field service of the electronic package. Proper interfacial reactions are desired to provide a good wetting of the molten solder. However, factors such as excessive IMC formation, UBM dissolution, interfacial void or crack formation would negatively affect the reliability of solder joints. Failure mechanisms identified in electromigration and drop impact tests of solder joints are often associated with the IMC formation.

The two kinds of UBM materials investigated in this dissertation are Cu-based and Ni-based, and the Cu-Sn and Ni-Sn phase diagrams are shown in Figs. 1.8 [79] and 1.9 [92]. For the Cu-Sn reaction, Cu_3Sn and Cu_6Sn_5 are the two stable phases that will form according to the phase diagram in Fig. 1.8. It has been reported that Cu_3Sn would not appear until

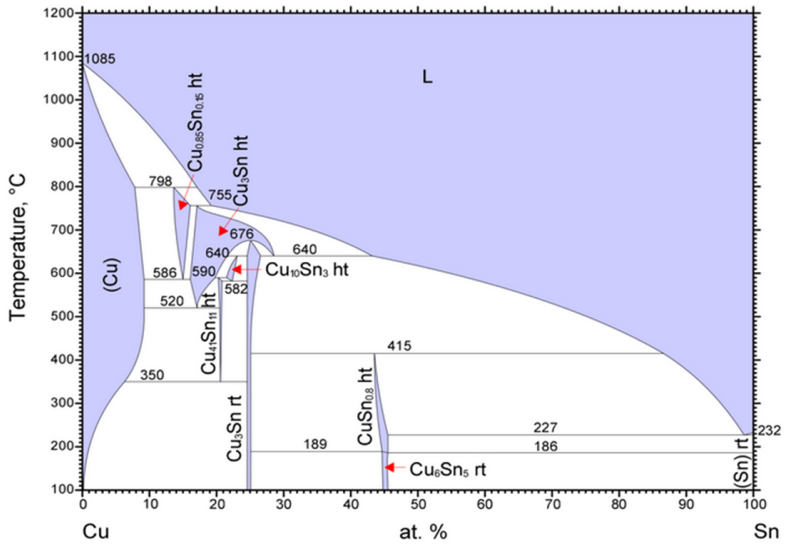

Figure 1.8: Cu-Sn phase diagram [79].

after a certain amount of reflow or solid-state annealing [103]. For the Ni-Sn system, three thermodynamically favorable phases, Ni_3Sn, Ni_3Sn_2, and Ni_3Sn_4 are present according to the phase diagram in Fig. 1.9. However, only Ni_3Sn_4 has been observed at the Ni/Sn interface [6, 11, 69] in solder joints. By using numerical thermodynamical calculations, Choi *et al.* [25] predicted Ni_3Sn_4 as the primary IMC to form.

1.3.3 EM Reliability of Pb-free Flip Chip Solder Joints

The reliability of flip chip solder joints can be traced to electrical, thermal and mechanical aspects and their complex interactions. Literatures have reported extensive findings on fundamental issues of Sn-based Pb-free

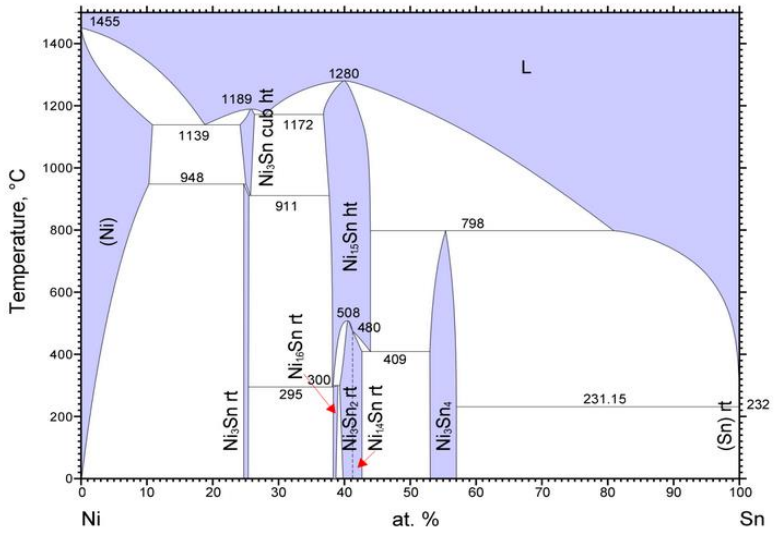

Figure 1.9: Ni-Sn phase diagram [92].

solder joints, including severe interfacial reactions during reflow or thermal annealing [59, 112], large Ag_3Sn plate formation [61], large undercooling during Sn solidification [58, 4], anisotropic physical and mechanical properties of Sn crystals [9], and fast diffusion of Cu, Ag, and Ni solute atoms along the *c*-axis of β-Sn crystal [34, 109]. These properties are closely related to the reliability issues of the flip chip solder joints, such as grain orientation effects on electromigration (EM) [76, 107] and thermal fatigue [9], void or crack formation in drop impact failure [94, 23, 81], fast fatigue crack growth along large Ag_3Sn plates [57], chip joining issues due to large undercooling [44], and excessive Cu consumption [29]. Among these, EM is one of the key reliability issues for Pb-free flip chip solder joints.

EM was identified as the cause of failure of aluminum interconnects in early integrated circuits [10]. The observation stimulated a great deal of research activities, and the study in EM has since been focused on practical problems related to damage formation in interconnects and its reliability implications.

EM describes the mass transport of atoms in a metal subject to an applied electric field. The drift velocity of the metal ions can be expressed by the Nernst-Einstein equation:

$$v_d = \mu F = \frac{D}{kT} F \tag{1.2}$$

where μ is the mobility, D is the diffusivity, k is the Boltzman constant, T is the absolute temperature in degrees Kevin, and F is the EM driving force. The Nernst-Einstein equation is a general description of the diffusion of a species induced by an external force. The study on the EM driving force can be categorized into two types, physical and phenomenological. The phenomenological description of EM is more useful because it offers a direct correlation between the applied electric field and the measurable observation of the atomic diffusion. The effective EM driving force was first proposed by Huntington [52],

$$F_{\text{eff}} = eZ^*E = e\left(Z^e + Z^w\right)E \tag{1.3}$$

where e is the electronic charge, E is the electric field, Z^e is the valence of the ion in the lattice and Z^w is a virtual charge number that accounts for the

electron wind force. The sum of the two, Z^*, known as the effective charge number, provides a measure of the EM driving force.

By substituting Eq. (1.3) into Eq. (1.2), the drift velocity of the metal ions can then be expressed as

$$v_d = \frac{D}{kT} eZ^* E \tag{1.4}$$

The atomic flux induced by EM is the product of the drift velocity, v_d, and the atomic density, C_0,

$$J = C_0 v_d = C_0 \frac{D}{kT} eZ^* E \tag{1.5}$$

In the 1960s, Black [10] developed a lifetime prediction model to estimate the mean time to failure (MTTF) of a wire under current stressing,

$$\text{MTTF} = Aj^{-n} \exp\left(\frac{E_a}{kT}\right) \tag{1.6}$$

where A is a constant, j is the current density, n is the current exponent, E_a is the activation energy, k is the Boltzmann constant and T is the temperature in degrees Kelvin. The values of A, n, and E_a are determined by fitting the model with experimental data. Eq. (1.6) was first proposed for BEOL Al interconnects, but has since then used for estimating failure time of solder joints.

Although EM lifetime in solder alloys can be characterized by a similar empirical model as in BEOL Al and Cu interconnects, EM in solder joints

is different in several aspects. First, lattice diffusion is the dominant diffusion mechanism in solder materials due to the low melting point. Second, typical UBM materials such as Cu and Ni are fast diffusion species in Sn operating in interstitial diffusion mechanism. Interfacial reactions and IMC kinetics are therefore critical in controlling the EM reliability of solder joints, whereas IMC formation is largely absent in Al or Cu interconnects. In addition, the anisotropic diffusion properties of Cu and Ni in Sn makes the problem more complicated. Thirdly, the EM-enhanced diffusion takes place in multiple phases. IMC growth is enhanced by EM, and controls the mass transport.

1.3.4 Reliability of 3D IC Microbumps

Microbumping is one of the key technologies in 3D integration, since it provides physical and electrical inter-chip connections. The reliability issues of the microbumps are therefore critical in stacked chip packages as well as during the wafer level integration processes. Sn-based Pb-free microbumps with various UBM structures are being developed by the microelectronics industry [115, 50, 73]. Due to the significant reduction in size of the microbumps compared with the conventional flip chip solder joints, the reliability issues and failure mechanisms of 3D IC microbumps can be different from flip chip solder joints.

As the pitch size reduces and the current density increases, the joule heating can be serious [22, 100]. Tu *et al.* [104] concluded that thermal man-

agement due to joule heating as one of the significant reliability problems for microbumps. Since thermal conduction requires thermal gradient, he also stressed that a large enough thermal gradient can trigger thermomigration in the microbumps. However, there's no experimental observations yet to prove the statement. Whether or not electromigration will be a reliability issue for microbumps has been studied by several research groups, which will be part of the study in this dissertation. Besides, Yu and his coworkers [111] reported crack propagation at the interface after highly accelerated temperature and humidity stress tests. Dunne *et al.* [33] have observed crack formation in Cu-Sn-Cu and Cu-Sn-Ni microbumps after thermal cycling tests. Son *et al.* [96] investigated the reliability of microbumps through thermal cycling and high temperature storage tests. Various failure modes have been observed such as pop-up failure, interface delamination, and IMC crack formation.

The results reported from the literature indicate that IMC formation is important in controlling the microbump reliability. Hence it would be important to generate more kinetic data of IMC growth in microbumps with different UBM systems. In addition, IMC formation accompanies significant amount of volume change due to density mismatch from the reacting phases. In general, tensile stresses will be generated if there is a net decrease in volume. The stress can be coupled into mass transport to either enhance or suppress interdiffusion. Voids or cracks can form to relieve the stress induced by phase transformation, which eventually leads to failure. In spite

of recent interest in TSV/microbump reliability and 3D integration in general, the problems in this study have mostly not been investigated and are important for the reliability of 3D integrated circuits.

1.4 Objective and Approach

In this dissertation, effects of IMC formation on reliability of Pb-free Sn-based solders for flip chip and 3D interconnects are studied. The objective of this work is four-fold. The first is to study the Sn crystal orientation effect on the electromigration reliability of Pb-free Sn-based flip chip solder joints. Both experimental and numerical approaches will be demonstrated. The second is to estimate the diffusion coefficients of the diffusing species in Cu-Sn and Ni-Sn IMCs using simulated annealing technique. The third one is to investigate the electromigration realibility of microbumps, and the last one is to establish an analytical model to study concurrent diffusion, phase transformation, and deformation in 3D IC microbumps. The future work and recommendations are summarized in the final chapter. The key contributions of this dissertation are as follows.

Electromigration of Pb-free Sn-based flip chip solder joints

The effect of Sn grain orientation on electromigration reliability of Pb-free Sn-based flip chip solder joints was studied. The multiple solder reflow process was proposed as one of the effective solutions to optimize Sn grain structure for better EM reliability. A kinetic model

taking into account the anisotropic properties of Sn was formulated as a supplement to further study the EM failure mechanisms. This is presented in Chapter 2.

Estimation of diffusion coefficients

Quantitative modeling of the kinetic analysis requires knowledge of the intrinsic diffusion coefficients of Cu and Sn atoms in the Cu-Sn IMCs, and Ni and Sn atoms in the Ni-Sn IMC. However, these critical parameters are not available from literature. In this study, the simulated annealing technique was applied to estimate these temperature-dependent parameters from experimentally observed measurements. The activation energies of each parameter were then calculated. Numerical approaches, results, and discussions are described in Chapter 3.

Reliability of 3D IC microbumps

The electromigration reliability of 3D IC microbumps were studied for Sn-based microbumps with three different UBM systems. This will be covered in Chapter 4 Then a numerical model was established to study concurrent diffusion, phase transformation, and deformation in the microbumps. The model is capable of coupling the stress effect into the kinetic analysis in order to study the stress induced by both interdiffusion and phase transformation. This is described in Chapter 5.

Chapter 2

Effect of Sn Grain Structure on Electromigration Reliability of Pb-free Flip Chip Solder Joints

Axis orientation affected the rate of spread of crops and livestock, and possibly also of writing, wheels, and other inventions.

Jared Diamond

2.1 Introduction

As stated in Chapter 1, electromigration (EM) is a persistent reliability concern for Pb-free flip chip solder joints. In this chapter, the effect of Sn grain structure on the solder EM reliability will be further studied.

One important characteristic in addressing EM reliability of Pb-free solder joints is the formation and growth of intermetallic compounds (IMCs) induced by material reaction between Sn and the contact metallization. A uniform IMC layer promotes adhesion. Excessive IMC formation, on the other hand, can lead to complete consumption of the under-bump metallization (UBM) to cause failure. Chao *et al.* [16] found that the IMC growth can be significantly enhanced under EM, while Gan *et al.* [40] investigated

the polarity effect of EM on IMC formation. Their study showed that the growth of the IMC layer was enhanced by EM at the anode end and inhibited at the cathode end. These results suggest that the kinetics of EM-enhanced IMC formation is critical in controlling the EM reliability of solder joints.

β-tin has a body-centered tetragonal structure with lattice parameters $a = b = 5.83$Å and $c = 3.18$Å, and is highly anisotropic. The Young's modulus and coefficient of thermal expansion (CTE) of β-Sn along a- and c-axes are summarized in Table 2.1. The anisotropic mechanical properties can lead to substantial internal stresses near grain boundaries due to heterogeneous deformation during thermal cycling [9]. The influence of Sn grain size and orientation on the thermo-mechanical reliability of Pb-free solder joints has been extensively studied [9, 72, 118]. The diffusion properties associated with the EM reliability are highly anisotropic as well. For instance, the interstitial diffusivity of Cu along the c-axis of Sn is 40 times faster than that along the a-axis at 150°C [34]. The difference is even more remarkable for Ni, where the diffusivity along the tetragonal axis at 120°C is about 7×10^4 times that perpendicular to the axis [109]. As the UBM is typically made of Cu or Ni, the extraordinary anisotropic diffusion behavior of these fast diffusing species in Sn is critical to the understanding of IMC formation and growth kinetics, which would in turn affect the EM reliability.

The effect of Sn grain orientation on EM reliability of Sn-based Pb-free solders has generated a great deal of interest and has been widely in-

Table 2.1: Young's modulus and CTE of β-Sn.

	Young's modulus (GPa)	CTE (ppm/°C)
a-axis	23 [9]	30.5 [89]
c-axis	69 [9]	15.45 [89]

vestigated [76, 75, 71]. Recently Lu *et al.* [76] has identified two distinct EM failure mechanisms in Sn-based solders, both strongly correlated with the Sn crystal orientations with respect to the current flow direction. Lee *et al.* [71] examined the EM behavior of Sn-Ag-Cu solder joints with Cu UBM. They reported a fast failure mode due to Cu UBM dissolution when the *c*-axis of Sn was parallel to the electron flow. Therefore, it would be important to study how the Sn grain structure would affect EM lifetime and statistics, and to develop possible approaches to control the grain structure for better EM performance.

In this chapter, the microtexture analysis technique used in this study, i,e, the electron backscatter diffraction (EBSD) technique, will first be introduced in Section 2.2. In Section 2.3, experimental results will be presented to investigate the effect of Sn grain structure on Pb-free solder EM reliability as well as to explore the use of multiple solder reflows for structural optimization for improvement in EM reliability. Section 2.4 will focus on a kinetic analysis of IMC formation incorporating anisotropic mass transport in order to study the EM degradation mechanisms. Finally, a summary will be given in Section 2.5.

2.2 Microstructure Analysis using EBSD Technique

Most techniques for texture analysis in materials science are based on diffraction by a crystal lattice. Texture analysis can be categorized by the type of radiation, e.g., X-rays, neutrons or electrons. A detailed introduction and discussion of this topic can be found in [36]. Electron backscatter diffraction (EBSD) is a scanning electron microscopy (SEM) - based technique for microtexture analysis, using the backscattered electron signals generated when an electron beam is diffracted from a crystalline sample. The principles for EBSD texture analysis are based on Kikuchi patterns first observed in the 1930s [83]. Following the commercialization of SEMs in 1960s, the development of real time computer indexing in 1980s, and further improvements to automatic pattern analysis in 1990s, now a state-of-the-art EBSD system can achieve [36]:

- An angular resolution of 200-500 nm
- An accuracy of $< 1^{\circ}$
- A pattern solving algorithm which takes a fraction of a second

This section describes the fundamental of a Kikuchi diffraction pattern, the experimental set-up of an EBSD system, and sample preparation for EBSD investigation.

2.2.1 Kikuchi Diffraction Pattern

Diffraction occurs when an incident electron beam onto a crystalline sample is scattered by the lattice plane. The scattered waves are interfered constructively according to the Bragg's law:

$$2d \sin\theta = n\lambda \tag{2.1}$$

where d is the spacing between the atomic planes, θ is the angle between the incident radiation and the scattering planes, n is an integer, and λ is the wavelength of the incident radiation.

When an electron beam enters a specimen, it is inelastically scattered, which results in a divergent source in all directions. Therefore there always exists some electrons that satisfy the Bragg's law for each set of lattice planes, and these electrons are subject to elastic scattering to give a reinforced beam. Since diffraction occurs in three dimensions, the locus of the diffracted electron beam is the surface of a cone with half apex angle $(90^\circ - \theta)$. A recording screen intercepts the diffracted cone to produce a pair of conic sections, as illustrated in Fig. 2.1. These pairs of lines are called Kikuchi band. For a typical wavelength and interplanar spacing, the Bragg angle θ for diffraction to occur is usually very small, which means that the cones intersecting a detector are nearly flat. Hence the Kikuchi bands we observe are pairs of parallel lines. For EBSD investigation, samples are usually tilted 70° with respect to the horizontal. The reason for tilting the sample

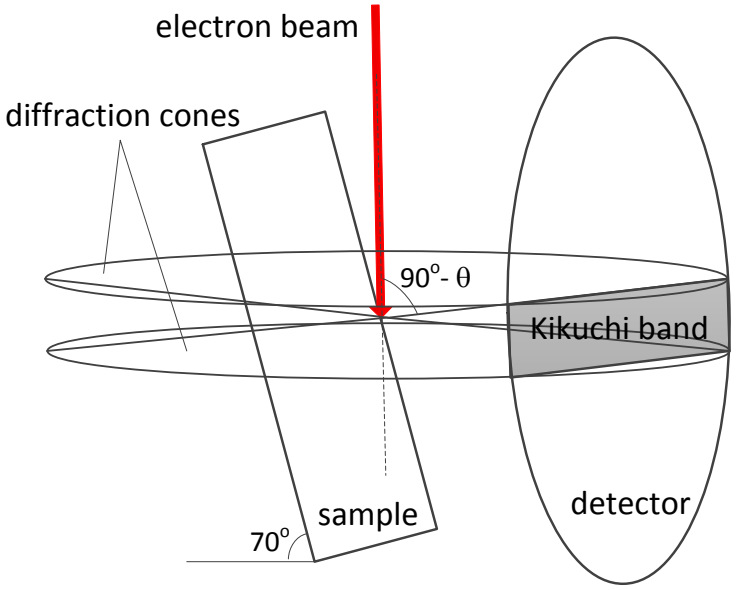

Figure 2.1: Schematic of the formation of a Kikuchi band.

is to reduce the path length of electrons that are backscattered by the lattice planes, thus allowing a greater proportion of them to escape from the sample and reach the detector instead of being absorbed. Figure 2.2 shows an EBSD Kikuchi pattern of stainless steel.

2.2.2 EBSD System

Figure 2.3 schematically shows the components of the EBSD system used in the lab. The EDAX APEX 2 EBSD system was integrated in a Zeiss Neon40 field emission SEM. The backscattered signals are collected by a phosphor screen which is interfaced to a low-light CCD camera. The diffrac-

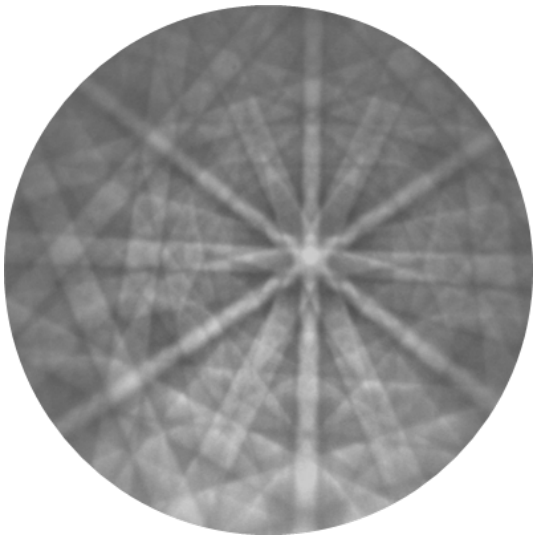

Figure 2.2: A Kikuchi pattern of stainless steel (courtesy EDAX).

tion pattern is viewed and then digitally enhanced via a processing unit which is connected to a computer for data analysis. A separate computer is used to control the microscope beam and stage movement.

There are several factors that control the spacial resolution and accuracy of an EBSD analysis.

Material

Heavy elements backscatter electrons more strongly than light elements, therefore the EBSD patterns from high atomic number elements show more clarity than those from low atomic numbers.

Working distance

For standard SEM operations, the resolution is improved by a short

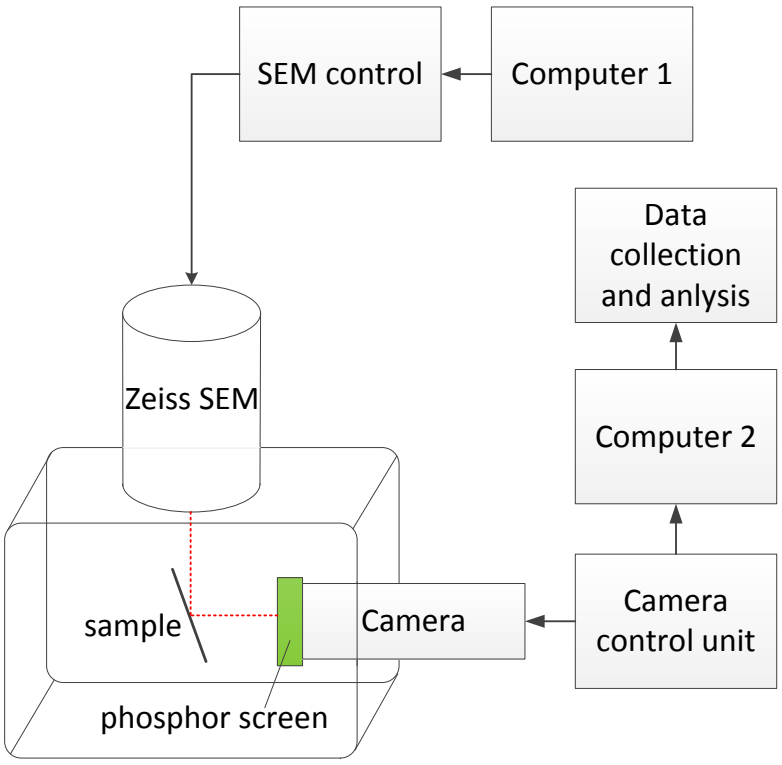

Figure 2.3: Schematic illustration of the set-up of the EBSD system.

working distance (WD). For EBSD, on the other hand, the WD is chosen to maximize the capture of backscattered electrons. Very short WD is prevented from collision risk due to the high angle tilting of the sample. A WD of $9 - 18$mm is recommended.

Accelerating voltage

The efficiency of the phosphor screen increases with accelerating voltage. However, increasing the accelerating voltage also increases the interaction volume, which results in a degradation in resolution. Hence a compromise has to be made between pattern clarity and interaction volume. A value of 20 kV is appropriate for general purposes. A low accelerating voltage should be chosen for fine grain sized analysis where resolution is critical.

Probe current

The probe current is selected in accordance with the light sensitivity of the camera, and 5nA is a good choice for a modern camera.

2.2.3 Sample Preparation for Pb-free Solders

Since the penetration depth of electrons is very small, the backscattered electrons come from the top $10 - 20$nm near the specimen surface. This means a defect-free sample surface is essential to ensure a high quality EBSD pattern index. Pb-free solders pose difficulties for EBSD sample preparation due to the softness of the solder material and high hardness

Table 2.2: EBSD sample preparation for flip chip Pb-free solder joints.

Step	Abrasive	Platen speed	Time (min)
1	320 grit SiC grinding paper	200 RPM	2
2	600 grit SiC grinding paper	200 RPM	2
3	800 grit SiC grinding paper	150 RPM	6
4	3 μm polycrystalline diamond suspension	150 RPM	3
5	1 μm polycrystalline diamond suspension	150 RPM	3
6	0.05 μm colloidal silica	150 RPM	2

mismatch among the solder alloy, the intermetallic, and the contact metal. Table 2.2 lists the sample preparation procedures used in this study. In addition to mechanical preparation, a conductive coating is required because the Pb-free solders are embedded in a flip chip electronic package consisting of non-conductive epoxy materials. A carbon sputtering method with a well controlled deposition rate was chosen for reasons that 1) the coating layer should be as thin as possible ($25 - 35$Å), and 2) carbon has a low atomic number which is associated with a larger mean free path of electrons compared to platinum or gold.

2.3 Effect of Sn Grain Structure on EM Reliability - Experimental Results

2.3.1 Experimental Details

The composition of solder joints used in this study was Sn-based alloy with 2.5 wt% of Ag. The UBM on the cathode side was a tri-layered sputtered film of TiW/Cu/Ni (2 μm). The anode side was a Cu pad with Sn plating surface finish and Sn-2.3Ag stencil printed solder-on-pad (SOP). The samples were divided into two groups, where one group was subjected to a single solder reflow process during assembly, while the other group was subjected to four additional reflow post-assembly. All reflow processes during assembly and post-assembly followed an industrial standard procedure for Pb-free solders, with a peak temperature of $240 \pm 5°C$ and a cooling rate of $0.5 - 2°C/s$. A series of accelerated EM testes were performed on a pair of solder joints in each test structure. The EM stressing conditions ranged from 1.39×10^4 to $2.19 \times 10^4 A/cm^2$, where the current densities were calculated based on the UBM opening area. The temperature increase induced by Joule heating was determined using a die metal thermistor. The oven temperature was set such that the actual temperature of the test structures ranged from 150 to 166°C. In order to detect damage formation, resistance changes were monitored by the Wheatstone bridge method, which has been described elsewhere [30]. Figure 2.4 shows the schematic of the Wheatstone bridge setup, where R1 represents the pair of solder joints under test.

Microstructure characterization was performed at several stages dur-

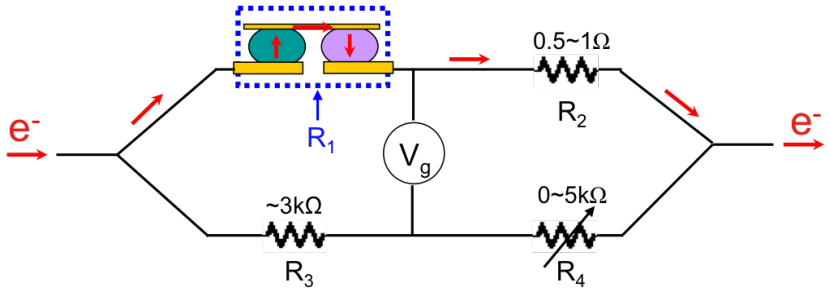

Figure 2.4: Schematic on the Wheatstone bridge method to monitor resistance change in solder joints during EM tests.

ing test: on the solder joints prior to EM tests to investigate the effect of solder reflows, on the EM-tested solder joints to determine failure mechanisms, and on solder joints subjected to thermal annealing alone to separate the thermal effect from the EM-induced effect. Solder joints under investigation were cross-sectioned and examined using the backscatter scanning electron microscopy (BS-SEM) to observe IMC growth and void formation. This was supplemented with an energy dispersed x-ray (EDX) analysis to identify the IMC phases, and finally the EBSD technique was applied to determine the Sn crystallographic orientation and grain size. The data were post analyzed using the EDAX TSL OIM^{TM} 5.0 software.

2.3.2 EM Failure Analysis

Figure 2.5 shows an example of a pair of solder joints after EM testing, with arrows indicating the electron flow direction. The anode bump where electrons flowed from the UBM side to the substrate side suffered from a more severe local current crowding, and thus failed earlier at the

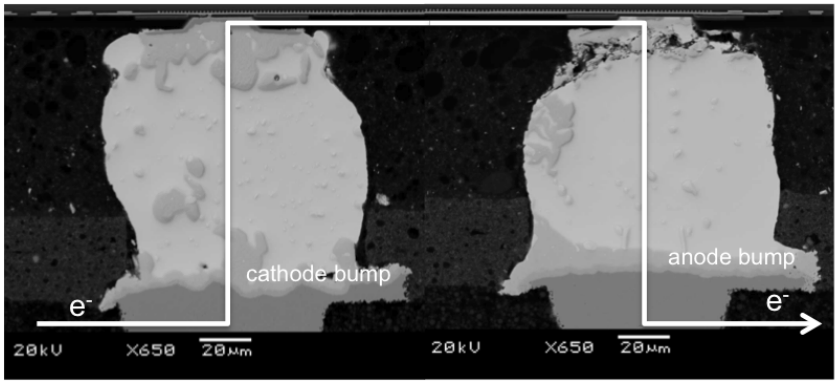

Figure 2.5: BS-SEM image of a pair of cross-sectioned solder joints after EM testing.

UBM area. Although a large amount of IMC formed in the cathode bump with extensive Cu dissolution, no crack or extended void accumulation was observed. Failure analysis hereafter will be focused on the anode bump. Figure 2.6 shows Wheatstone bridge voltage (V_g) traces as a function of EM testing time for three test vehicles, representing an early failure, a late failure, and a survivor. For the first two samples, V_g was found to increase first slowly in the initial stage, and then followed by an abrupt jump corresponding to $90-95\%$ opening of the solder joint. The first voltage jump was taken to be the time-to-failure of the test vehicle.

Figure 2.7 shows the cross-section of a solder joint, which was the first to fail in the test. The BS-SEM image (Fig. 2.7(a)) reveals that most of the Ni UBM was consumed to form $(\mathrm{Ni,Cu})_3\mathrm{Sn}_4$ IMCs, most of which were observed to be swept away from the UBM side to the substrate side. Figure 2.7(b) shows the EBSD mapping of Sn of the same joint, indicating

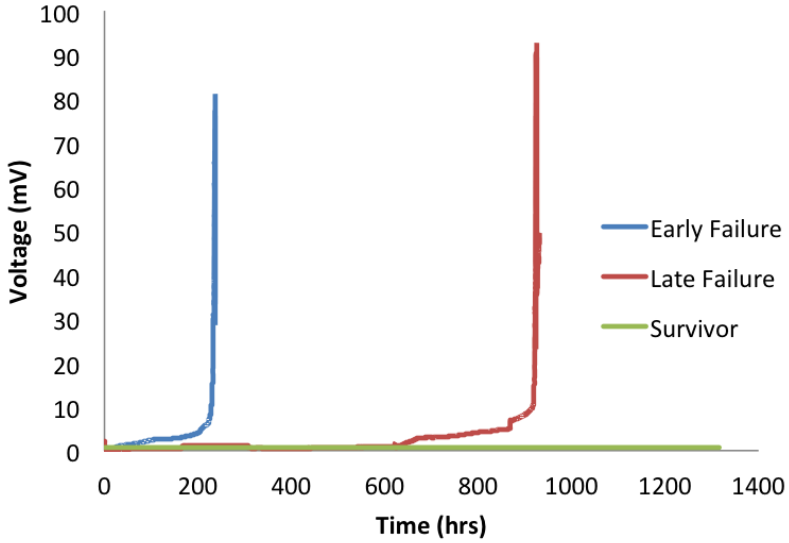

Figure 2.6: Voltage change across the Wheatstone bridge (V_g) versus EM testing time for three test vehicles.

that the solder joint was composed of a single grain. The angle between the c-axis of the Sn crystal and the electron flow direction was calculated using a mathematical relationship between the Euler angle of the crystal orientation $(\varphi_1, \varphi_2, \varphi_3)$ given by the software and the Cartesian coordinate system transformation matrix g. The value of the angle ranges from 0 to 90° showing how closely the c-axis of the Sn crystal aligns to the electron flow. The angle goes to zero when the c-axis is parallel with the electron flow and conversely goes to 90° when it is perpendicular to the electron flow. It is worth noting that the angle offers a way to verify the effect of the interstitial diffusion of Ni in Sn on damage formation. In this particular solder joint, the Sn grain had its c-axis aligned 36° off from the electron flow

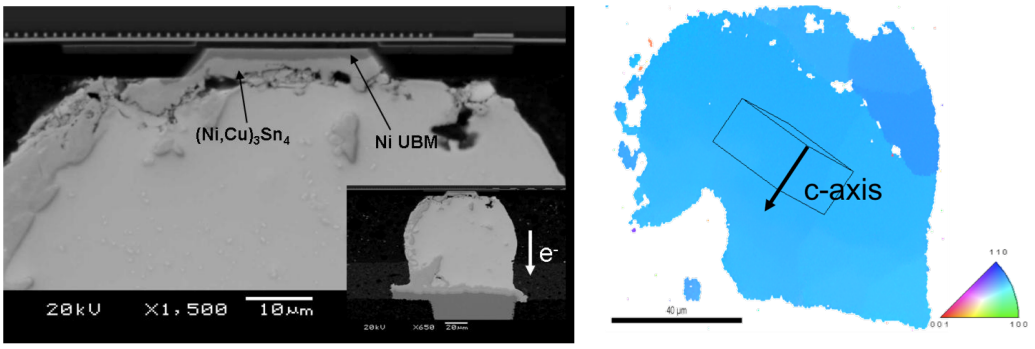

(a) (b)

Figure 2.7: Cross-sectional analysis of a solder joint that failed after 237 h of current stressing. Test conditions: $5.57 \times 10^4 \mathrm{A/cm^2}$, 158°C. (a) BS-SEM image and (b) EBSD mapping of Sn with *c*-axis alignment illustration.

direction. Fig. 2.7(a) also indicates that IMC swept away from the UBM side formed directionally at the lower left corner of the solder joint, which was approximately along the direction of the *c*-axis. These observations clarify the role of Sn grain orientation in the IMC formation kinetics during EM. The tetragonal cells provided Ni with an interstitial diffusion path that was a much faster route than that of Sn self-diffusion. The diffusion was further enhanced by EM, thus leading to excessive UBM consumption. It can be inferred that the low-angle alignment caused enhanced IMC dissolution at the UBM and accumulation at the substrate side. EM failure occurred at a fast rate due to UBM depletion.

Figure 2.8 shows the case of a late failure. The black holes inside the IMCs were believed to be embedded particles due to polishing. It can be found from Fig. 2.8(a) that Ni dissolution led to extensive IMC formation in the form of $(\mathrm{Cu,Ni})_6\mathrm{Sn}_5$ and $(\mathrm{Ni,Cu})_3\mathrm{Sn}_4$. However, IMCs in the

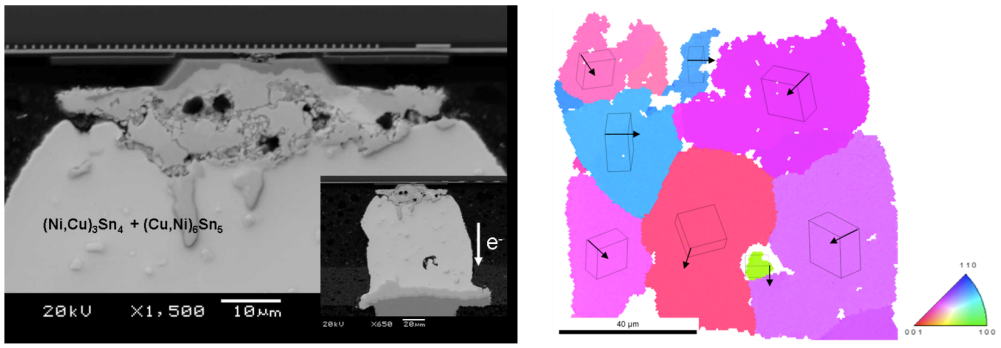

(a) (b)

Figure 2.8: Cross-sectional analysis of a solder joint that failed after 924 h of current stressing. Test conditions: $5.57 \times 10^4 \mathrm{A/cm^2}$, 158°C. (a) BS-SEM image and (b) EBSD mapping of Sn with *c*-axis alignment illustration.

joint were accumulated at the UBM side rather than being swept away toward the substrate end. This implied that the mass flux was substantially slowed down near the interface, thus preventing the IMC from further dissolution. The EM degradation mechanism was attributed to the specific Sn grain structure as shown in Fig. 2.8(b), where the EBSD mapping revealed a multi-grain structure with different grain orientations. The angles between the *c*-axis and the electron flow direction were calculated for the top three grains adjacent to the UBM region where IMC formed, and the values were found to be 58, 89, and 59°, respectively. Comparing to the early failure, the grain orientations of this solder joint displayed a relatively high angle against the electron flow. This means the fast interstitial diffusion path can be cut off by both a high angle alignment and a multi-grain structure.

Figure. 2.9 presents a solder joint that did not fail after 1295 h of EM testing under $5.57 \times 10^4 \mathrm{A/cm^2}$ at 158°C. The BS-SEM image in Fig. 2.9 re-

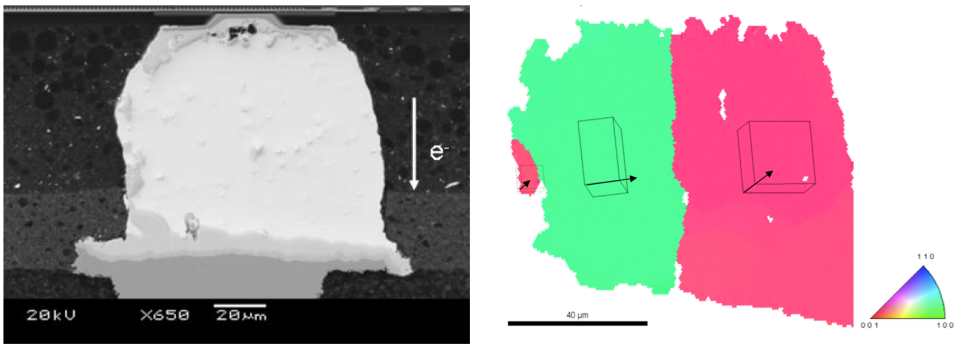

(a) (b)

Figure 2.9: Cross-sectional analysis of a solder joint that did not fail after 1295 h of current stressing. Test conditions: $5.57 \times 10^4 \mathrm{A/cm^2}$, 158°C. (a) BS-SEM image and (b) EBSD mapping of Sn with *c*-axis alignment illustration.

vealed that only part of the Ni UBM was consumed while a large portion of it remained unreacted and continued to function as an excellent electrical contact. Results calculated from the EBSD mapping in Fig. 2.9 show that the solder joint was composed of three grains, with their *c*-axes aligned 80, 83, and 80°, respectively, to the electron flow. The high resistance to EM again confirmed a strong correlation with the extremely anisotropic diffusion property where diffusivity along the *a*-axis is several orders of magnitude slower.

The failure analysis indicates that Sn grain oreintations and structures play an important role in controlling the IMC growth kinetics. Given the present observation, it would be interesting to explore solutions that are able to avoid single grain with low angle alignment along the *c* -axis with respect to the electron flow direction and instead to produce multi-grain structures with high angle alignment. For this purpose, solder joints sub-

jected to different thermal processes were further investigated using EBSD. One possible way is to to optimize the solder reflow process, since the reflow parameters, such as number of reflows, cooling rate, peak temperature, etc., may change the solidification conditions that would in turn change the grain structure. In this study, the effect of multiple reflows was of particular interest and thus was investigated. To supplement this study, the effect of thermal annealing on microstructural evolution was also studied, and the results will be discussed in the following two subsections.

2.3.3 Effects of Multiple Reflow

In order to investigate the effect of multiple reflow on Sn grain structures, thirty as-received solder joints prior to EM testing were randomly sampled from each of the single- and multiple-reflow groups. Those solder joints were cross-sectioned and characterized using the EBSD technique. Figure 2.10 is a collection of EBSD mappings of solder joints subjected to a single solder reflow during the flip chip assembly. As it is shown, after a single standard reflow process, the solder joints were found to be composed of a few large Sn grains per joint. Moreover, a significant portion of them exhibited a low angle *c*-axis alignment to the electron flow direction, as highlighted in the first row of Fig. 2.10. For solder joints with more than one grain shown in the cross-sections, the grain boundary characteristics were further studied. Grain boundaries with a 60° rotation about the (301) plane and the $\langle 100 \rangle$ axis within a tolerance of 5° were identified as highlighted in

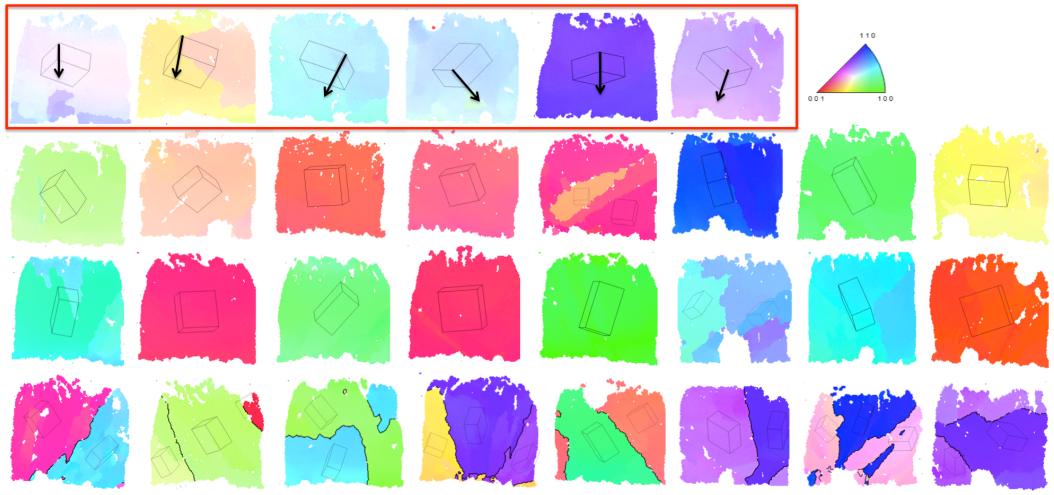

Figure 2.10: EBSD mappings of as-received solder joints subjected to a single solder reflow process.

black solid lines in Fig. 2.10. It is interesting to note that such grain boundaries satisfied the β-Sn's twin misorientation relationship, which is in good agreement with previous observations in Sn-Ag solder balls with a much larger size [93]. The cyclic twin structures are illustrated in Fig. 2.11. With the (001) pole figure projected on a Wulff net, the 60° rotational relationship is clearly demonstrated.

Figure 2.12 presents the EBSD mappings of thirty solder joints subjected to four additional reflows post-assembly. It was found that majority of the solder joints exhibited a mix of a few large grains with numerous small grains. Interestingly, the interlaced Sn grain morphology tended to accumulate near the substrate side of the solder joints. Furthermore, the extent of the interlaced structure varies from one to another, indicating some

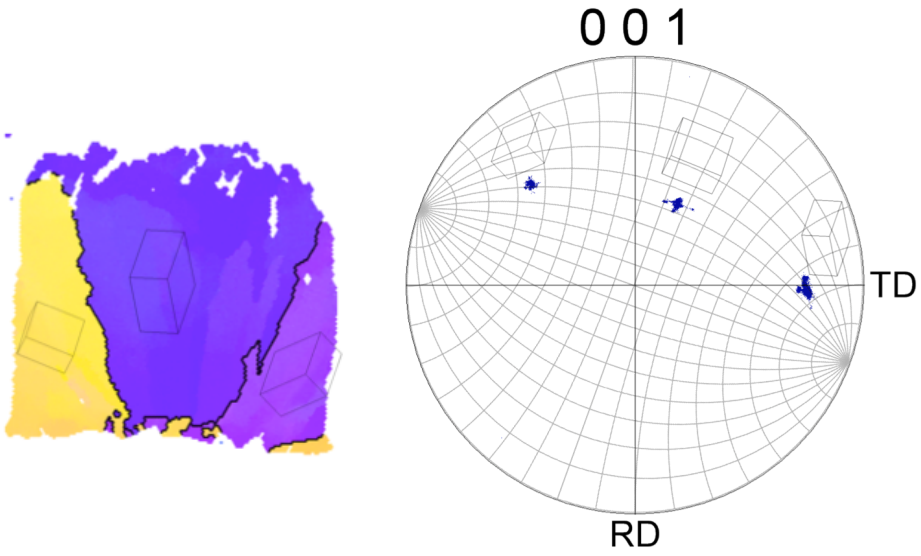

(a) (b)

Figure 2.11: Cyclic twin structure in one of the solder joints subjected to single reflow during assembly: (a) EBSD mapping and (b) (001) pole figure projected on the Wulff net.

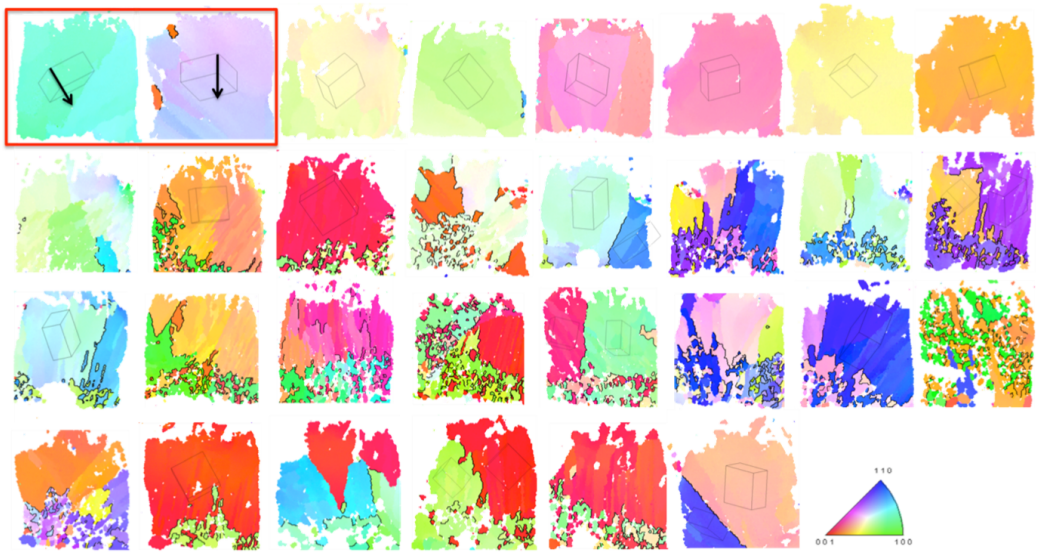

Figure 2.12: EBSD mappings of as-received solder joints subjected to four additional reflows post-assembly.

randomness of this process. Overall, two out of thirty solder joints showed a low angle alignment.

The grain size histogram for groups with and without additional solder reflows is shown in Fig. 2.13. The results compile the grain size measurement of thirty solder joints and thus show an "average" grain size distribution, where the error bars represent the standard deviation. For the single reflow group, solders tended to form large grains expanding to the whole flip chip joint with an average grain size greater than 60 µm. For solder with multiple reflows, on the other hand, interlaced morphology coexisted with large grains, leading to a wider distribution in grain size.

The misorientation histogram for both groups is shown in Fig. 2.14.

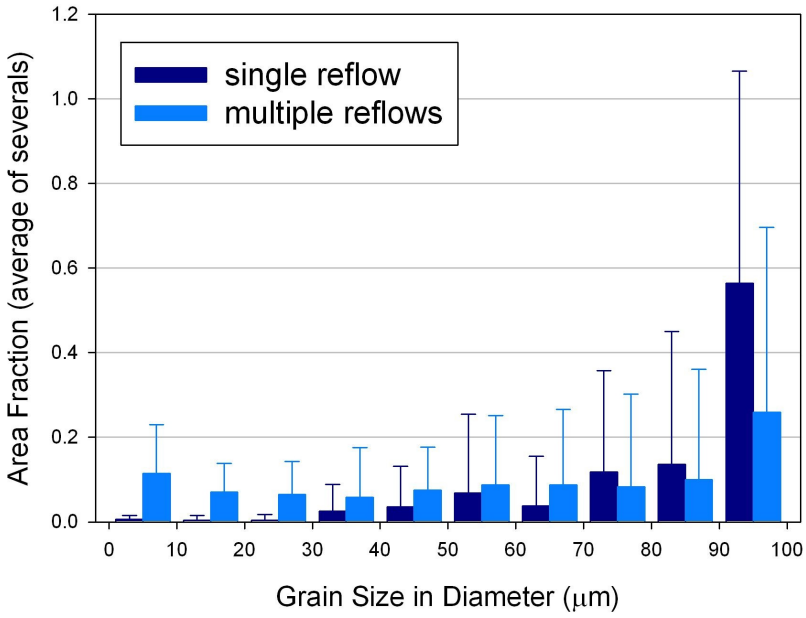

Figure 2.13: Grain size histogram for as-received solder joints with single or multiple solder reflows.

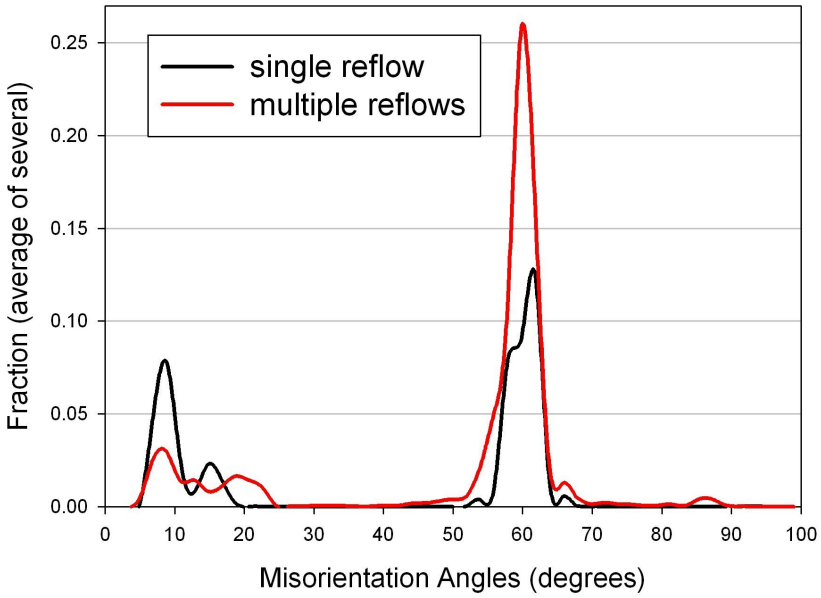

Figure 2.14: Misorientation histogram for as-received solder joints with single or multiple solder reflows.

The results revealed two types of grain boundaries, i.e., small-angle boundaries ($< 20°$) and $60°$ twin boundaries. Moreover, the multiple reflow group exhibited a smaller fraction of small-angle boundaries and a larger fraction of twin boundaries than the single reflow group. This result, combined with the EBSD mappings, showed that solder joints with a single reflow consisted of either single grain or the beach ball structure, while interlaced twin structures were more commonly observed in solder joints subjected to additional reflows. Results from Figs. 2.13 and 2.14 suggested that both grain size and grain orientation were altered after four additional solder reflows, which will be correlated to its improved EM reliability in later discussion.

Previous failure analyses showed that the presence of a single grain

with *c*-axis aligned to the electron flow direction enhanced Ni diffusion, accelerated IMC formation, and increased the probability of early failure. Hence it is suggested that the process of single solder flow would not be favorable for EM reliability. In contrast, solder joints with four additional reflows resulted in a less anisotropic microstructure by means of high-angle twin boundaries and interlaced morphologies, and therefore would reduce the risk of early failure.

2.3.4 Effects of Thermal Annealing

To investigate the effect of thermal annealing on microstructure, solder joints from each group were subjected to isothermal treatment at 150°C for 450 h. Figures 2.15 and 2.16 show EBSD mapping results. Grain structure for solders with single reflow largely remained unchanged as can be seen in Fig. 2.15. In contrast, grain growth was observed in solders with multiple reflows (Fig. 2.16) after thermal annealing. The interlaced morphology that was commonly observed in as-received samples no long existed. The change indicated that the interlaced twinning structures were not thermodynamically favorable and would reach equilibrium by grain growth, allowing a reduction in both strain energy and grain boundary energy.

Further quantitative analysis was carried out and results are shown in Figs. 2.17 and 2.18. Figure 2.17 shows the grain size histogram of solder joints subjected to either single or multiple reflows followed by ther-

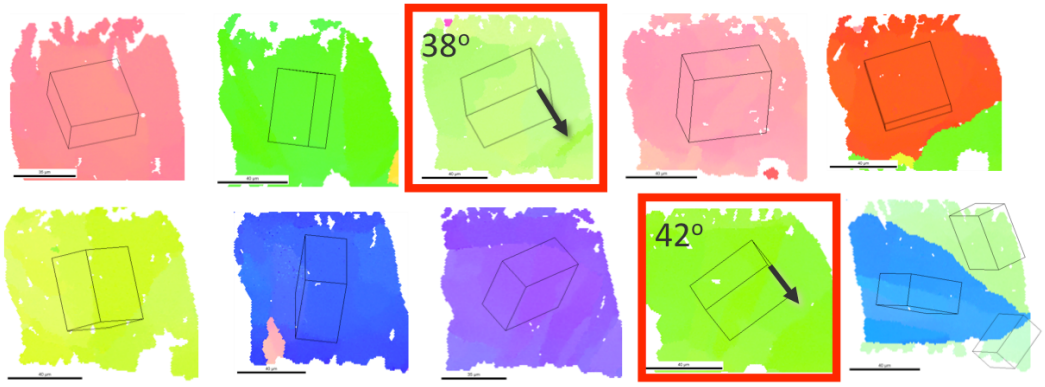

Figure 2.15: EBSD mappings of solder joints subjected to a single solder reflow followed by thermal annealing under 150°C for 450 h.

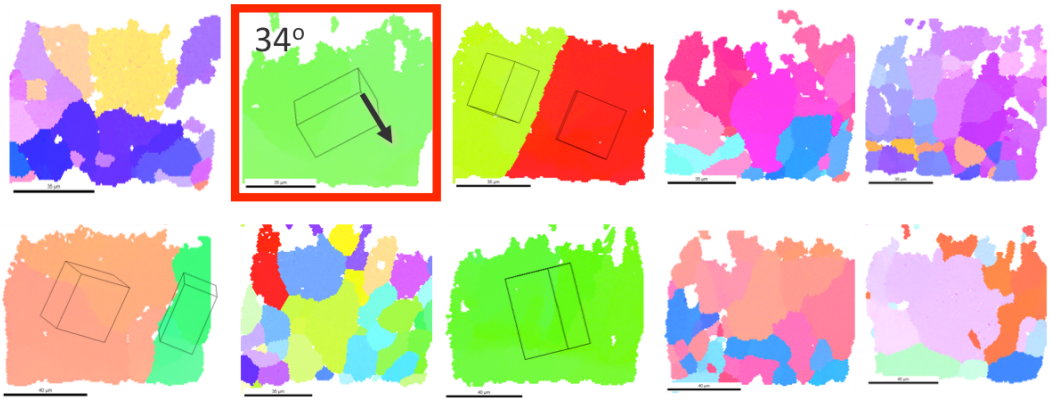

Figure 2.16: EBSD mappings of solder joints subjected to four additional solder reflows followed by thermal annealing under 150°C for 450 h.

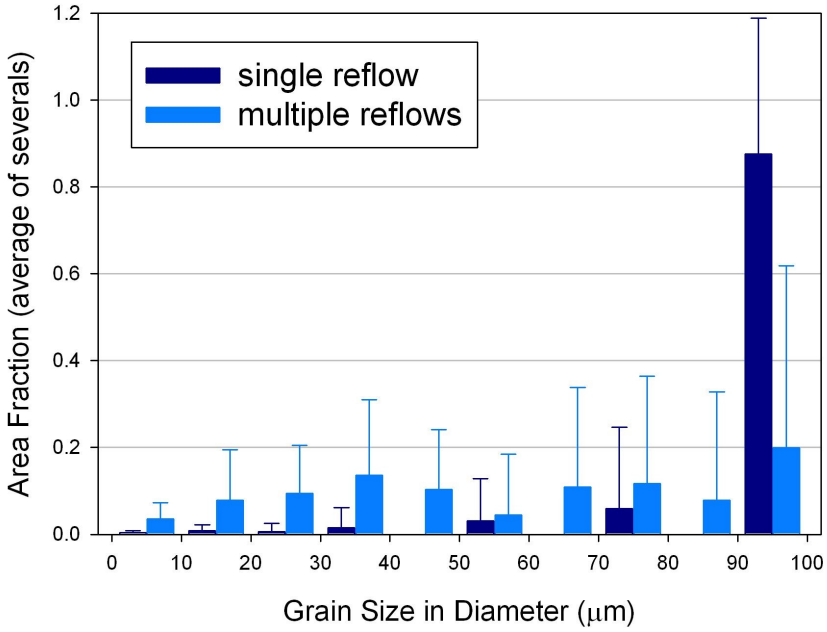

Figure 2.17: Grain size histogram of solder joints subjected to either single or multiple reflows followed by thermal annealing under 150°C for 450 h.

mal annealing. Both groups experienced some grain growth after thermal annealing. In case of solders with a single reflow, the average grain size exceeded 80 μm, whereas for the case of multiple reflowed solders, grains smaller than 10 μm were substantially reduced. The misorientation histogram of thermal annealed solder joints is shown in Fig. 2.18. In addition to small-angle boundaries and 60° twin boundaries which were observed in as-received samples, some high-angle ($> 70°$) boundaries were also present in both single and multiple reflow groups. (Add some comments on literature reports: microstructure evolution under thermal annealing!)

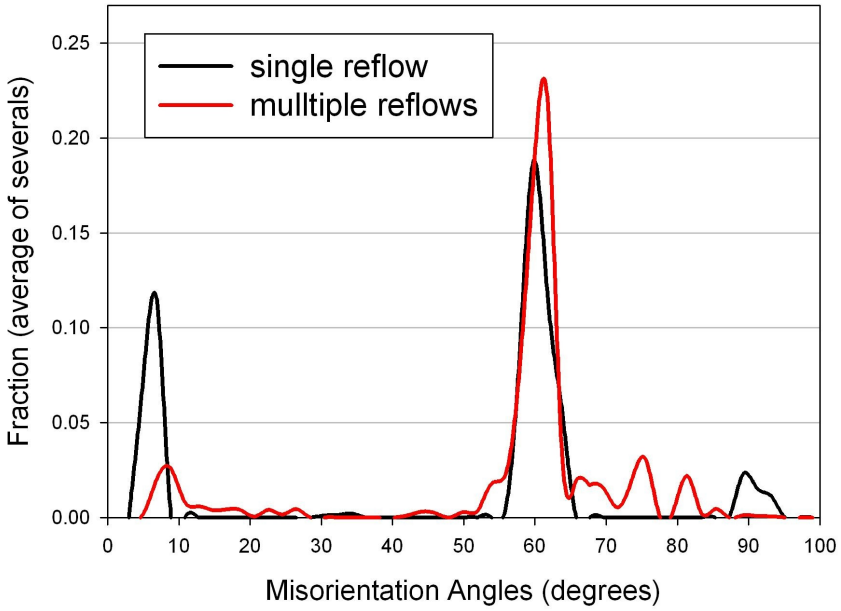

Figure 2.18: Misorientation histogram of solder joints subjected to either single or multiple reflows followed by thermal annealing under 150°C for 450 h.

2.3.5 EM Results

The EM testing results were combined with the microstructural characterization to study the effects of Sn grain structure on EM lifetime and statistics. Figure 2.19 shows a collection of microscopic analysis of EM tested solder joints. An early failure, a late failure, and a survivor from each of the single and multiple reflow groups are presented. Figure 2.20 complies the corresponding EBSD mappings of solder joints shown in Fig. 2.19. Table 2.3 summarized the grain structure in terms of size and orientation for solder joints shown in Fig. 2.20. For multi-grain structures, an averaged angle with respect to the electron flow direction was obtained by summing up the individual grain orientations weighted by their grain sizes. As can be found, both solder joints in Fig. 2.20(a) and (d) consisted of a single grain with low angle *c*-axis alignment with the electron flow. When this happens, atoms such as Ni and Cu can diffuse interstitially in the Sn matrix at an extremely fast rate, leading to UBM depletion and IMC dissolution within a short time. This failure mechanism is consistent with observation by Lu *et al.* [76] observation, and thus can be categorized as the more detrimental Mode II failure. In contrast, multi-grain structure with 60° twin boundaries effectively averaged out the anisotropic properties in solder joints, and thus were effective in avoiding Mode II failure which was confirmed by Fig. 2.20(e). Such solder joints like this are considered as Mode I failure, which is a result of enhanced Sn self diffusion under EM. The flux divergence at the IMC/solder interface leads to void accumulation and eventu-

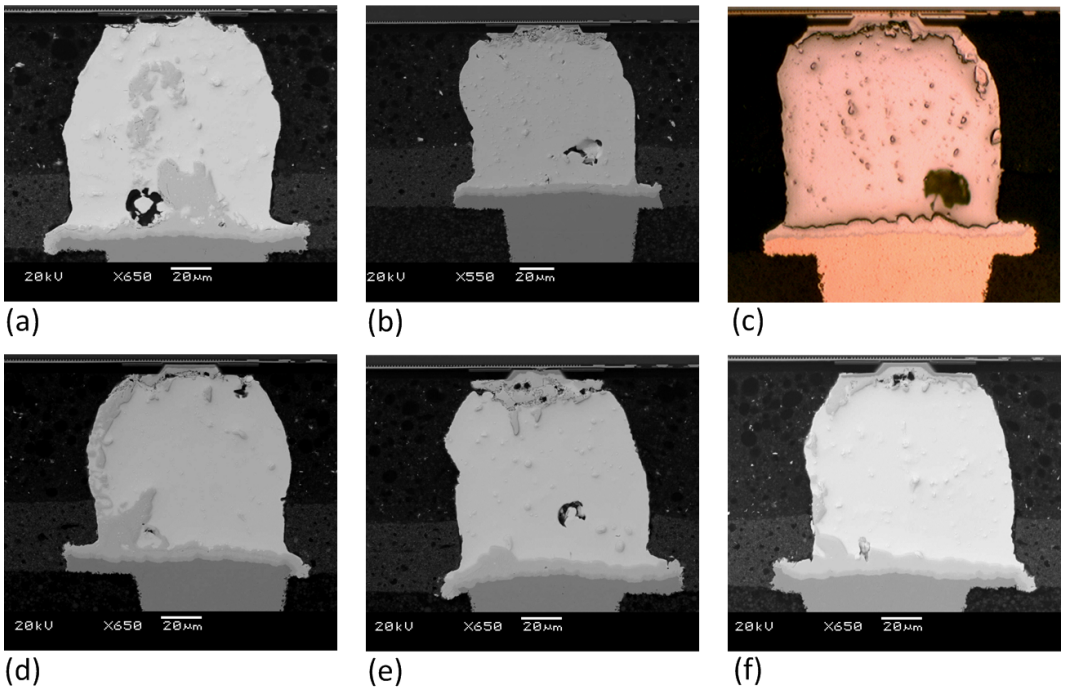

Figure 2.19: Microscopic analysis of EM tested solder joints: (a)-(c) come from the single reflow group, while (d)-(f) from multiple reflow group. (a, d) Early failures, (b, e) late failures, and (c, f) survivors.

ally an open fail but at a slower rate than the Mode II failures shown in Figs. 2.19(a) and (d). Therefore, it is clear that both Sn grain size and orientation could contribute to the IMC growth kinetics and void formation.

The statistical distribution in EM lifetime for groups with single and multiple solder reflows are shown in Fig. 2.21. The EM testing conditions along with EM statistics are summarized in Table 2.4. The single reflow group had a standard deviation, σ, larger than that of multiple reflows group, which is consistent with the Sn grain characteristics. A small standard deviation is desired in accelerated tests since the EM lifetime under

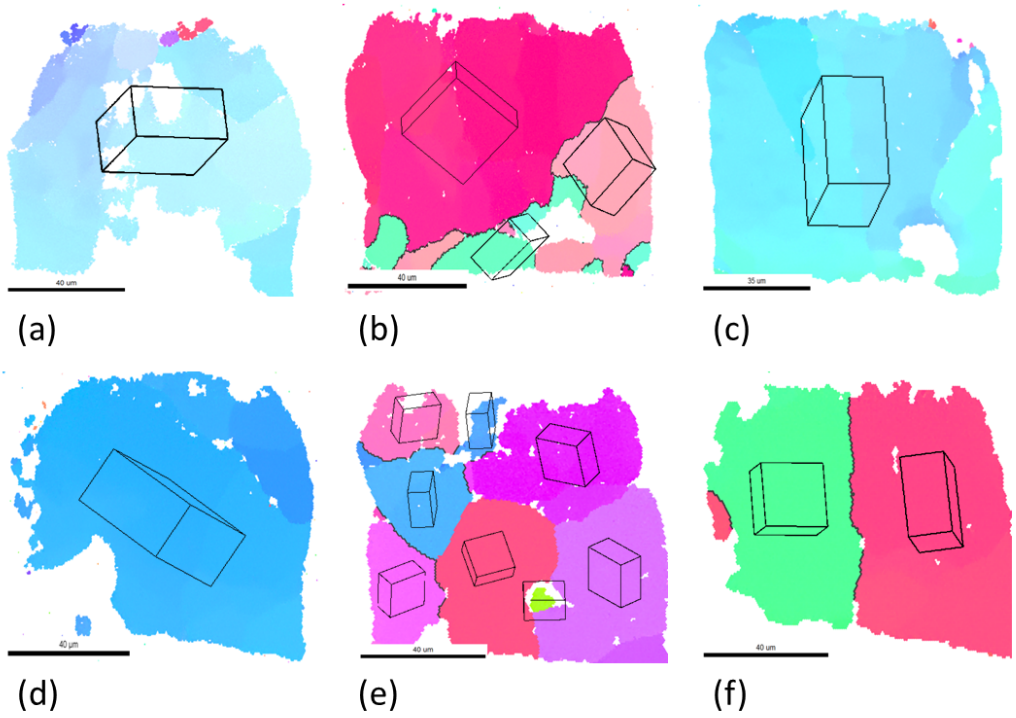

Figure 2.20: EBSD mappings of EM tested solder joints shown in Fig. 2.19.

Table 2.3: Results of angles between the *c*-axis of the Sn grain and the electron flow direction based on an area weighted average calculation for solder joints shown in Fig. 2.20.

	Early failure	Late failure	Survivor
Single reflow	20°	66°	89°
Multiple reflows	36°	67°	79°

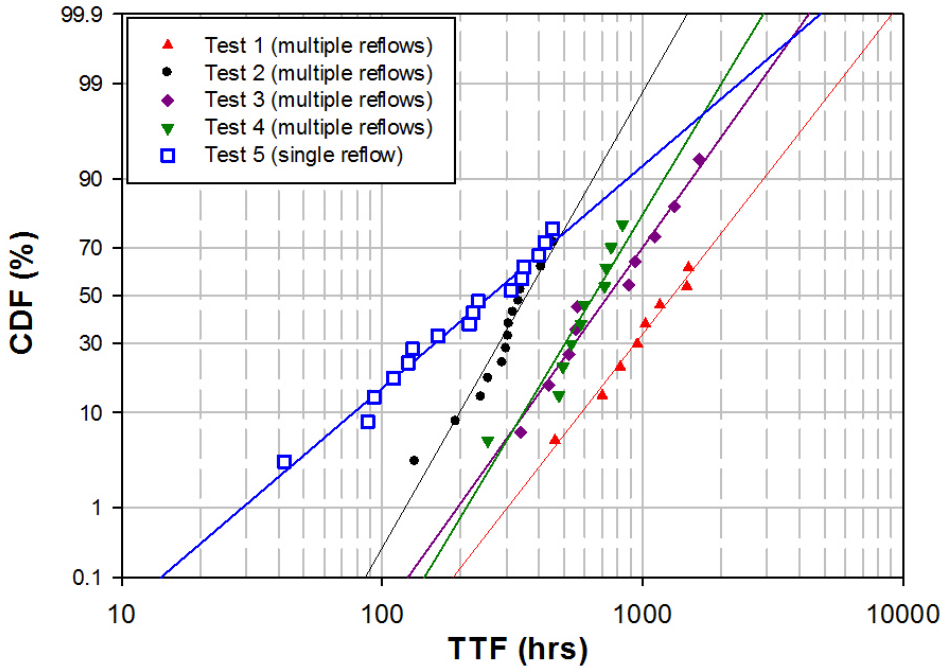

Figure 2.21: Statistical distribution in EM lifetime for solder joints with single and multiple solder reflows.

operational condition is obtained by extrapolating the experimental data under stressing conditions. The multiple solder reflow process enabled a more homogeneous Sn microstructure from one joint to another to produce a smaller σ, thus is effective in improving EM statistics.

2.3.6 Discussion

2.3.6.1 Effect of Grain Boundary Diffusion

It has been demonstrated that solder joints with multi-grain structure in general can slow down the UBM depletion rate by varying the grain

Table 2.4: Summary of the EM testing conditions and statistical results.

	Test 1	Test 2	Test 3	Test 4	Test 5
Reflow process	Multiple	Multiple	Multiple	Multiple	Single
Current density (A/cm^2)	1.69×10^4	1.69×10^4	2.19×10^4	1.39×10^4	2.19×10^4
Temperature (°C)	150	166	150	158	150
t_{50} (hours)	1300.5	357.5	737.9	649.2	260.5
Standard deviation (σ)	0.63	0.46	0.57	0.49	0.94

orientations to cut off the fast diffusion path. However, only lattice diffusion is considered so far whereas the grain boundary diffusion is ignored. In fact, an effective diffusion coefficient can be derived taking both diffusion processes into consideration:

$$D_{\text{eff}} = fD_{\text{gb}} + (1 - f)D_{\text{lattice}} \tag{2.2}$$

where D_{eff} is the effective diffusion coefficient, D_{gb} is the grain boundary diffusion coefficient, D_{lattice} is the lattice diffusion coefficient, and $f = \frac{q}{d}\delta$. Here q is a parameter ranging from 1 to 3, which depends on the grain shape, d is the averaged grain size, and δ is the grain boundary width which often assumed to be 0.5 nm. The grain size of flip chip solder joints is usually about tens of microns, and hence f is in the order of 10^{-5}. This means even though D_{gb} is considerably higher than D_{lattice}, the grain boundary diffusion can be neglected due to relatively small fraction of grain boundaries present. Thus results from previous analyses based on lattice diffusion

is justified.

2.3.6.2 Grain Structure Optimization

It can be concluded from this study that single grain with *c*-axis parallel to the substrate would result in a strong EM performance. Here, only the EM reliability is taken into account. In contrast, studies from other research groups has shown that Sn grains with *c*-axis perpendicular to the substrate is preferable in terms of thermo-mechanical reliability such as solder fatigue, due to the fact that cracks are less likely to occur when the *c*-axis is aligned in this way. Furthermore, given the fact that it is hard to control the crystal orientation using standard industrial processes, solder joints with single grain are not recommended. Alternatively, it would be more promising to explore structural optimization leading to multi-grain structures. Multiple solder reflow process is therefore a practical approach which has proven to be beneficial for EM reliability and at the same time would not degrade its mechanical integrity.

2.3.6.3 Multiple Solder Reflows

This study has shown that a single solder reflow produces one or a few large grains in a flip chip solder joint. This can probably be attributed to the fact that β-Sn is difficult to nucleate from the liquid, resulting in a large amount of undercooling during solidification. Indeed, a considerable degree of undercooling of $40 - 80^{\circ}$C has been observed in flip chip solder

joints. Due to the large amount of undercooling, rapid solidification takes place once one or two nucleation sites are formed during the first solder reflow. The amount of undercooling has been found to increase as the solder size decreases [5]. Arfaei *et al.* [5] studied the effect of solidification temperature on Sn grain morphology of Sn-Ag-Cu solders. Their results indicated that solders solidified at a higher temperature mostly exhibited beach ball structures, while those solidified at a lower temperature tended to have interlaced Sn grain morphology. In addition to size, other metallurgy parameters can also have an influence in the determination of the Sn grain morphology, such as solder alloy composition, UBM materials, impurity level of Sn, cooling rate, and holding time. The subsequent solder reflows in this study dissolves Ni (on the UBM side) and Cu (on the substrate side) into the solder joints. It may lead to more IMC formation as well as a more uniform IMC network, which would affect the nucleation and grain growth in the process of Sn solidification. Based on the present results, however, single grain structures cannot be completely prevented from multiple reflows, indicating the random nature of the nucleation event and the effect on the lifetime statistics. Further investigation on joining integrity to improve the process consistency is therefore suggested.

In addition, further research is required to better understand the microstructure evolution as a function of times in the reflow process. This is of practical importance in the industry when evaluating solder joint reliability in ball grid array packages versus land grid array packages where the time

required is different.

2.4 Effects of Sn Grain Orientation on EM Reliability - Numerical Analysis

Numerical analysis has been used by several research groups to study the EM degradation mechanism. Chao *et al.* [16, 18] studied EM-enhanced IMC growth in the Cu-Sn system. The EM damage mechanism was also investigated by considering the vacancy transport under EM stressing and estimating the crack driving force using finite element analysis (FEA). Pharr *et al.* [88] investigated the stress field in solder joints by coupling EM and creep processes. The solder joint was treated as a pure metal, ignoring the intermetallic formation, and thus their model failed to explain the Mode II failure mechanism. To the best knowledge of the author, no kinetic analysis has been reported that incorporates properties of anisotropic diffusion in the solder EM study. It is therefore the purpose of this study to establish a theoretical framework based on mass transport to study the effects of Sn grain orientation on EM degradation mechanism due to anisotropic diffusion Pb-free solder joints.

2.4.1 Model Description

The kinetic analysis of EM-enhanced IMC growth is complicated because diffusion in IMCs involves more than one type of diffusing species, and usually multiple phases. Interdiffusion takes place in IMCs where atoms

of different species can diffuse in opposite directions under concentration gradients. In addition, an electron wind force needs to be added into the diffusion analysis to account for the EM effect. Finally, phase transformation occurring between two adjacent phases determines the rate at which each phase grows or shrinks.

Consider a Ni-Sn diffusion couple subject to an EM driving force, where the electrons flow from the UBM side to the solder. An intermediate phase, Ni_3Sn_4, forms. This is illustrated by the Ni-Sn diffusion couple in Fig. 2.22(a), with the corresponding composition profiles as shown in Fig. 2.22(b). For simplicity, the derivation shown here is limited to one layer of IMC in between, although the approach can be extended to include two or more IMCs such as in the Cu-Sn system. Within the IMC phase, Ni and Sn atoms diffuse in opposite directions driven by concentration gradients. At the same time, they are subject to an EM wind force driving them along the electron flow direction. Following Darken's analysis for interdiffusion [28], the Fick's first law of diffusion can be written

$$N_{\mathrm{Ni}}^{\mathrm{Chem}} = -\widetilde{D}\frac{\partial C}{\partial z} \tag{2.3}$$

where N is the net atomic flux, C is the number of Ni atoms per unit volume, z is the direction along which diffusion takes place, and $\widetilde{D}$ is the interdiffusion coefficient first proposed by Darken [28]. $\widetilde{D}$ takes the form

$$\begin{aligned} \widetilde{D} &= (1 - \Omega C_A) D_A + \Omega C_A D_B \\ &= X_B D_A + X_A D_B \end{aligned} \tag{2.4}$$

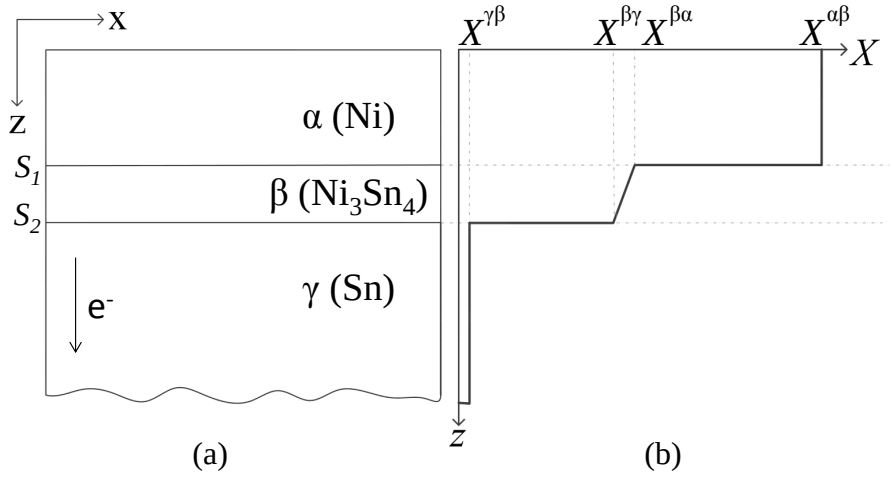

Figure 2.22: (a) Schematic of an UBM-solder material subject to EM with an electtron flow from UBM to the solder joint. A Ni_3Sn_4 IMC layer forms in between with two moving boundaries. S_1 and S_2. (b) Corresponding composition profile in atomic fraction of Ni.

where X_A and X_B are the number of fraction of atoms A and B, and Ω is the atomic volume.

It has been shown that the EM-induced atomic flux of Ni in the IMC phase can be expressed by [19]

$$N_{\mathrm{Ni}}^{\mathrm{EM}} = C\tilde{v}_d \tag{2.5}$$

$$\tilde{v}_d = \frac{D_{\mathrm{Ni}}F_{\mathrm{Ni}} - D_{\mathrm{Sn}}F_{\mathrm{Sn}}}{kT}(1 - X) \tag{2.6}$$

Here $\tilde{v}_d$ is defined as the effective drift velocity in a binary system, k is the Boltzmann constant, T is the temperature in degree Kelvin, X is the atomic fraction of Ni, D is the intrinsic diffusion coefficient, and F is EM driving

force that relates to the electric current as $F = Z^* e \rho j$, where Z^* is the effective charge number, e is the elementary charge, ρ is the resistivity, and j is the current density.

The total net atomic flux in the IMC, N, is the sum of the two fluxes driven by the concentration field and the external electric field:

$$N = N_{\mathrm{Ni}}^{\mathrm{Chem}} + N_{\mathrm{Ni}}^{\mathrm{EM}} \tag{2.7}$$

Fick's second law gives rise to the governing equation for mass transport of Ni in the IMC phase under EM,

$$\frac{\partial C}{\partial t} = -\frac{\partial N}{\partial z} = \frac{\partial}{\partial z}\left(\widetilde{D}\frac{\partial C}{\partial z} - C\tilde{v}_d\right) \tag{2.8}$$

From Eq. 2.8 it is clear that the mass flow of Ni in the IMC depends on the diffusion coefficients of both Ni and Sn and the current density. Diffusion in boundary phases, however, has to be treated differently. In the Ni UBM, diffusion of Sn is negligible because of the lack of solubility and mobility of Sn in Ni. Therefore, the UBM can be considered as a pure metal gradually dissolving into the IMC. In the solder joint, the interstitial diffusivity of Ni in Sn is so high that the characteristic length $\sqrt{D_{\mathrm{Ni}} t}$ is much larger than the length of solder even for a short amount of time (Appendix A). As a result, the solder can be treated as a phase saturated with Ni. In the lack of a concentration gradient, the atomic flux of Ni in both the UBM and the solder depends only on the EM driving force as:

$$J \cong J^{\mathrm{EM}} = C\frac{DZ^* e \rho j}{kT} \tag{2.9}$$

where all the parameters refer to the designated phases.

In addition to interdiffusion, solid-state phase transformation takes place near the phase boundaries. Here the rate at which the phase boundary migrates is critical for understanding the Mode II failure mechanism because it determines how fast the UBM material is dissolved. Based on mass conservation, the migration at the phase boundaries, S_1 and S_2 (Fig. 2.22(a)), can be expressed as,

$$dz\Big|_{S_1} = \frac{1}{X^{\alpha\beta} - X^{\beta\alpha}} \left[J_\alpha\Big|_{S_1} - J_\beta\Big|_{S_1} \right] dt \tag{2.10}$$

$$dz\Big|_{S_2} = \frac{1}{X^{\beta\gamma} - X^{\gamma\beta}} \left[J_\beta\Big|_{S_2} - J_\gamma\Big|_{S_2} \right] dt \tag{2.11}$$

where the fluxes are evaluated at their own boundaries, and the Xs are the upper and lower composition limits of Ni in atomic fraction. Detailed derivation of the interface migration due to phase transformation is described in Appendix B.

A numerical computation based on a finite difference approach was performed for Pb-free Sn-based solder joints with Ni UBM. A temperature was chosen to be 170°C with an initial UBM thickness of 2 μm, and an initial Ni_3Sn_4 thickness of 1 μm. This simulated the configuration of a typical flip chip solder joint. The simulation simulates 2000 h of testing, but stops when it detects a total consumption of the UBM material. The effective charge numbers of Ni in the pertinent phases were not readily available in the literature, so the values for Cu were used, considering that Ni has similar electronic structure as Cu. The intrinsic diffusion coefficients in Sn are

orientation dependent. For a single crystal Sn, the effective diffusion coefficient can be expressed by [109]

$$D(\theta) = D_{\parallel} \cos^2\theta + D_{\perp} \sin^2\theta \tag{2.12}$$

where $D_{\parallel}$ and $D_{\perp}$ are the diffusion coefficients along the c-axis and a or b-axes, respectively. θ is the angle between the tetragonal axis of the crystal and the z-coordinate along which diffusion takes place. In Fig. 2.23, the effective diffusion coefficients versus the Sn crystal orientation are plotted at four temperatures. The grain orientation effect on the diffusion coefficient is significant, varying by two to four orders of magnitude. The orientation dependence becomes even stronger at lower temperatures.

The physical parameters used in the simulation are listed in Table 2.5. The effect of Sn grain orientation was studied by varying θ from 0 to 90° to simulate different cyrstal orientations with respect to the elctron flow. The calculation begins with a linear concentration profile in the IMC. During a small step dt, the concentration evolves based on Eq. 2.8, and the moving interfaces are updated according to Eqs. 2.10 and 2.11. The concentration at the IMC boundaries are kept constant as the upper and lower composition limits.

2.4.2 Simulation Results

Figure 2.24 shows numerical results for Ni_3Sn_4 growth as a function of EM stressing time at four current densities when θ is 0 or 90°. The

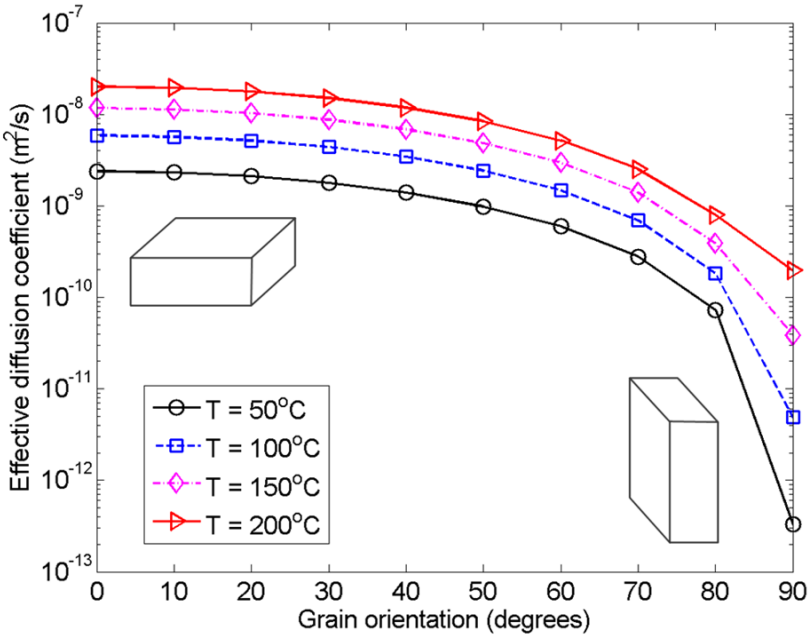

Figure 2.23: Effective diffusion coefficients of Ni in Sn versus Sn crystal orientation at four temperatures.

Table 2.5: Physical parameters used in the simulation [109, 19, 39].

	Ni	Ni_3Sn_4	Sn
Atomic volume ($10^{-29}m^3$)	1.09	1.78	2.72
Composition limit	1	0.427 - 0.44	10^{-6}
Diffusion coefficient (m^2)	1.6×10^{-37} (Ni)	1.36×10^{-17} (Ni) 6.81×10^{-18} (Sn)	$1.47 \times 10^{-8} \parallel c$ (Ni) $7.73 \times 10^{-11} \perp c$ (Ni)
Effective charge number	4.5 (Ni)	21 (Ni) 21 (Sn)	0.5 (Ni)
Resistivity (μΩ-cm)	7.8	28.5	11.5

IMC growth under thermal annealing alone was also calculated as a reference. Results in Fig. 2.24 indicate a significant difference in kinetics near the UBM interface when the Sn crystal orientation changes with respect to the electron flow. When the *c*-axis of Sn is aligned to the current direction (Fig. 2.24(a)), IMC thickness decreases with increasing EM stressing time. With a higher current density, the rate of IMC thickness decreases more rapidly. This can be attributed to the extremely fast interstitial diffusion of Ni in the open lattice of Sn, and the process is further enhanced by EM where Ni ions are driven to the anode side by the electron wind force. This can reach a point as shown in Eq. 2.11 where beyond a threshold current density, the Ni supply from the IMC phase ($J_\beta\Big|_{S_2}$) can no long keep up with the dissolution into the solder ($J_\gamma\Big|_{S_2}$). Consequently, with the Sn matrix serves as an effective sink, Ni dissolves rapidly and diffuses toward the anode side instead of forming intermetallic at the cathode side. The situation, however, is very different when the *c*-axis of Sn is normal to the current direction, as shown in Fig. 2.24(b) where the IMC growth is enhanced at the cathode side, and the growth rate changes from parabolic to linear with increasing current density. Such a phenomenon has been observed in flip chip solder joints with Cu UBM [18].

Results in Fig. 2.24 indicate only the Ni_3Sn_4 growth at the cathode side, and does not represent the total IMC growth rate. Since the solubility of Ni in Sn is very low (Table 2.5), it would be expected that most Ni which was swept away from the cathode side would precipitate to form IMC on

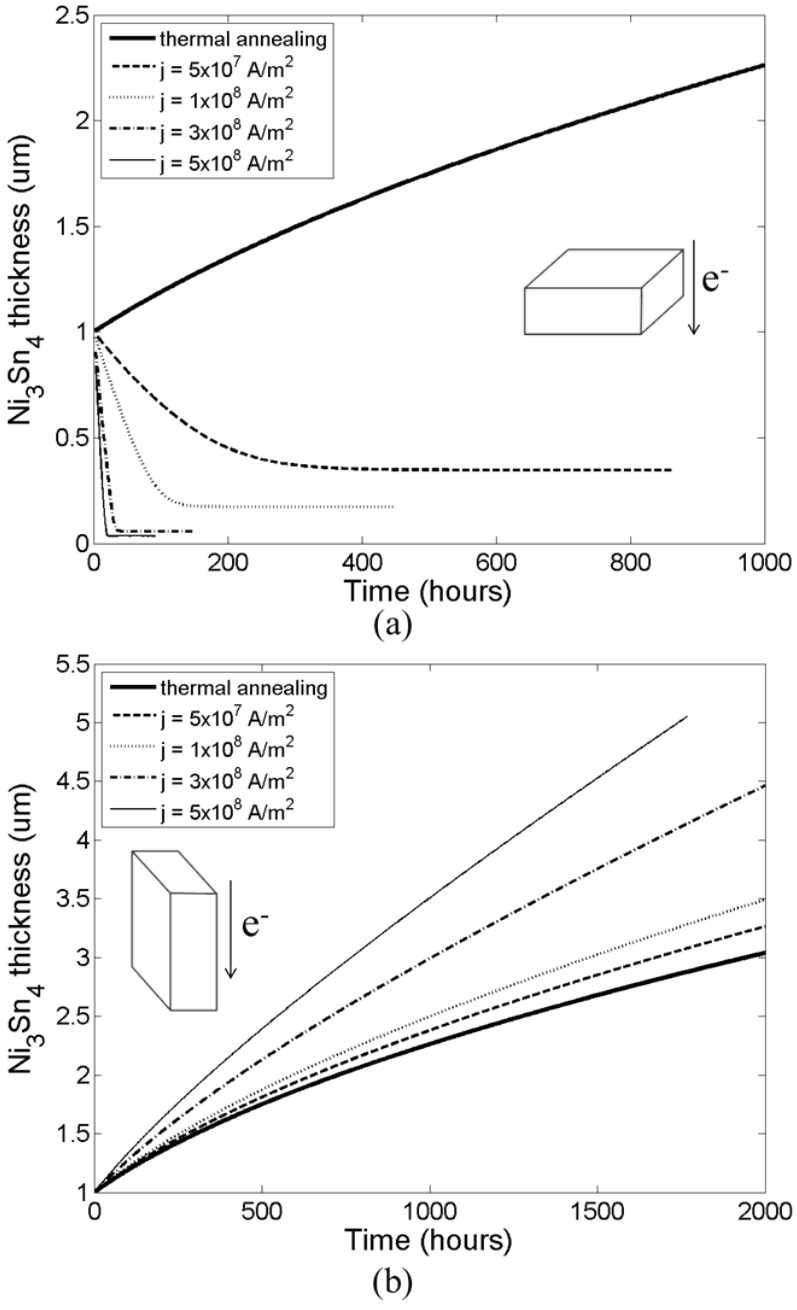

Figure 2.24: Ni_3Sn_4 growth at the UBM side as a function of stressing time at four current densities when (a) $\theta = 0$, and (b) $\theta = 90^\circ$.

the opposite side. In order to study the total IMC growth, another Ni_3Sn_4 phase was added to the model at the anode side, as illustrated in Fig. 2.25. It was assumed that an effective barrier layer existed to block any mass transport beyond the terminating phase. Figure 2.26 shows the total Ni_3Sn_4 growth when $\theta = 0$ and 90°. The results suggest that the overall IMC thickness increases as the current density increases. Moreover, the total growth rate is much faster when $\theta = 0$ under the same current density. Simulation results presented in Figs. 2.24 and 2.26 show that IMC can indeed be swept away from one side to the other by the electron wind force for Sn grains with a small θ. This has been observed experimentally as shown in Fig. 2.20(a) and (d), where IMC near the UBM was found to be depleted while a significant amount was formed toward the anode side. Observations by EBSD revealed that the solder joints in these figures had crystal orientations with an average θ of about 20° and 36°, respectively. The IMC dissolution near the UBM followed by formation towards the anode side for Sn grains with small orientation angles would degrade the adhesion strength between solder/UBM to pose a reliability risk.

Figure 2.27 shows the numerical results for UBM consumption as a function of EM stressing time at four different current densities for θ values of 0 and 90°, respectively. Results show two effects due to the EM driving force and the grain orientation. The EM effect was straightforward in that the UBM depletion rate increases as current density increases. The grain orientation effect was also clear by examining the results in Fig. 2.27 where

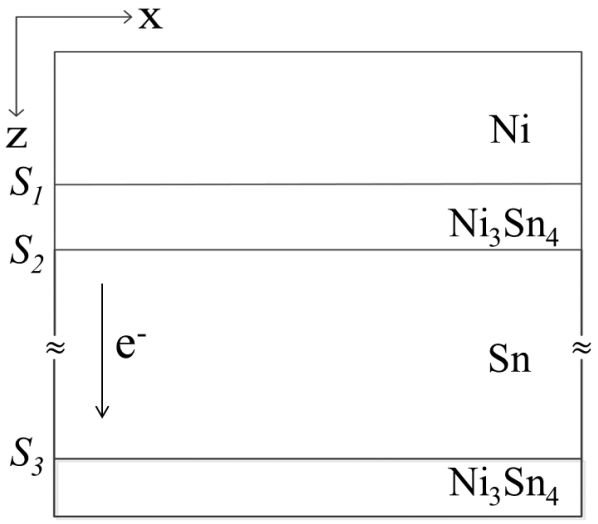

Figure 2.25: Schematic of the modeled structure with an added Ni_3Sn_4 phase at the anode side.

the total UBM consumption does not occur until $j = 5 \times 10^8 \mathrm{A/cm^2}$ when $\theta = 90^\circ$, although it happens under $j = 5 \times 10^7 \mathrm{A/cm^2}$ when $\theta = 0$. It follows, therefore, that the UBM consumption rate strongly depends on the Sn grain orientation as well as current density. Results in Fig. 2.27 are in good agreement with Figs. 2.24 and 2.26. Since IMC forms at the expense of the UBM, it takes much shorter time to fail a solder joint by UBM depletion when θ is small.

The times needed for complete UBM depletion as a function of Sn grain orientation at four current densities, denoted as t_{II} are shown in Fig. 2.28. These curves provide an estimate for the time required to fail a solder joint due to UBM depletion. It is interesting to compare t_{II} with the time required for sufficient void formation to fail a solder joint due to Sn self-diffusion,

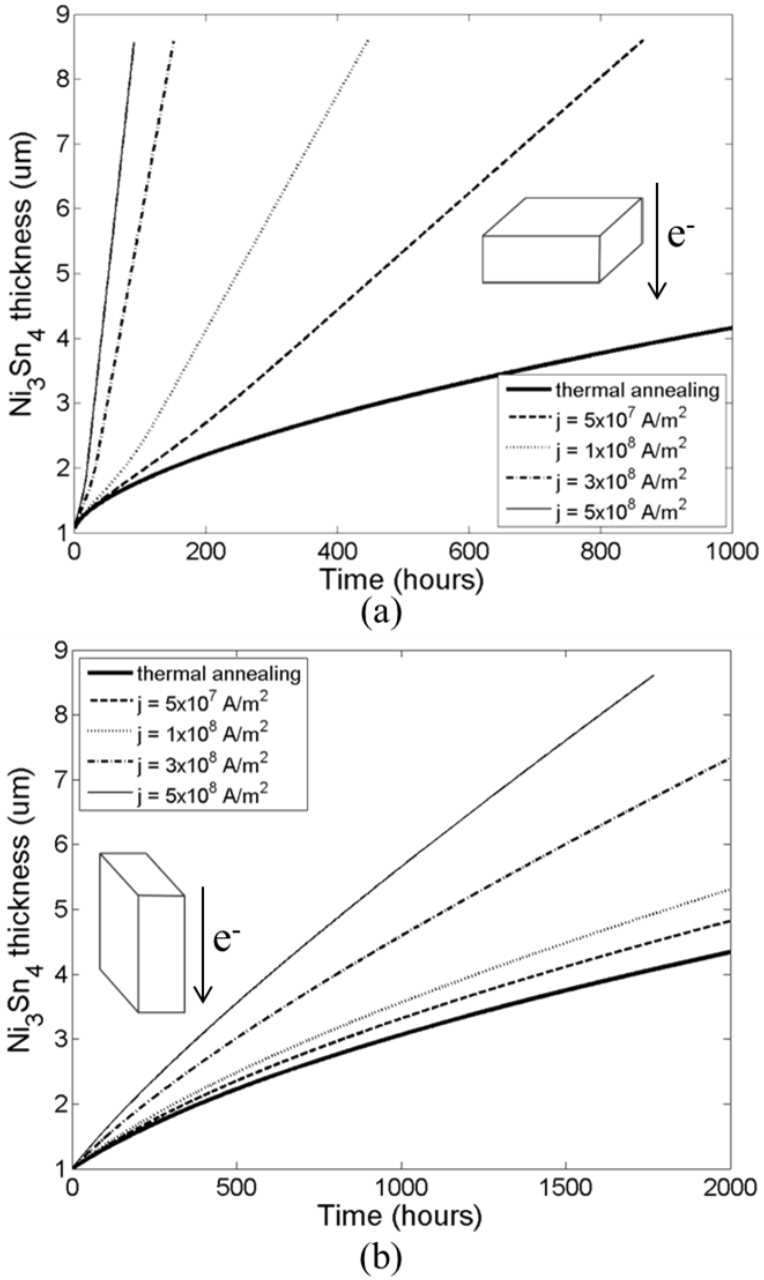

Figure 2.26: Total Ni_3Sn_4 growth as a function of stressing time at four current densities when (a) $\theta = 0$, and (b) $\theta = 90^\circ$.

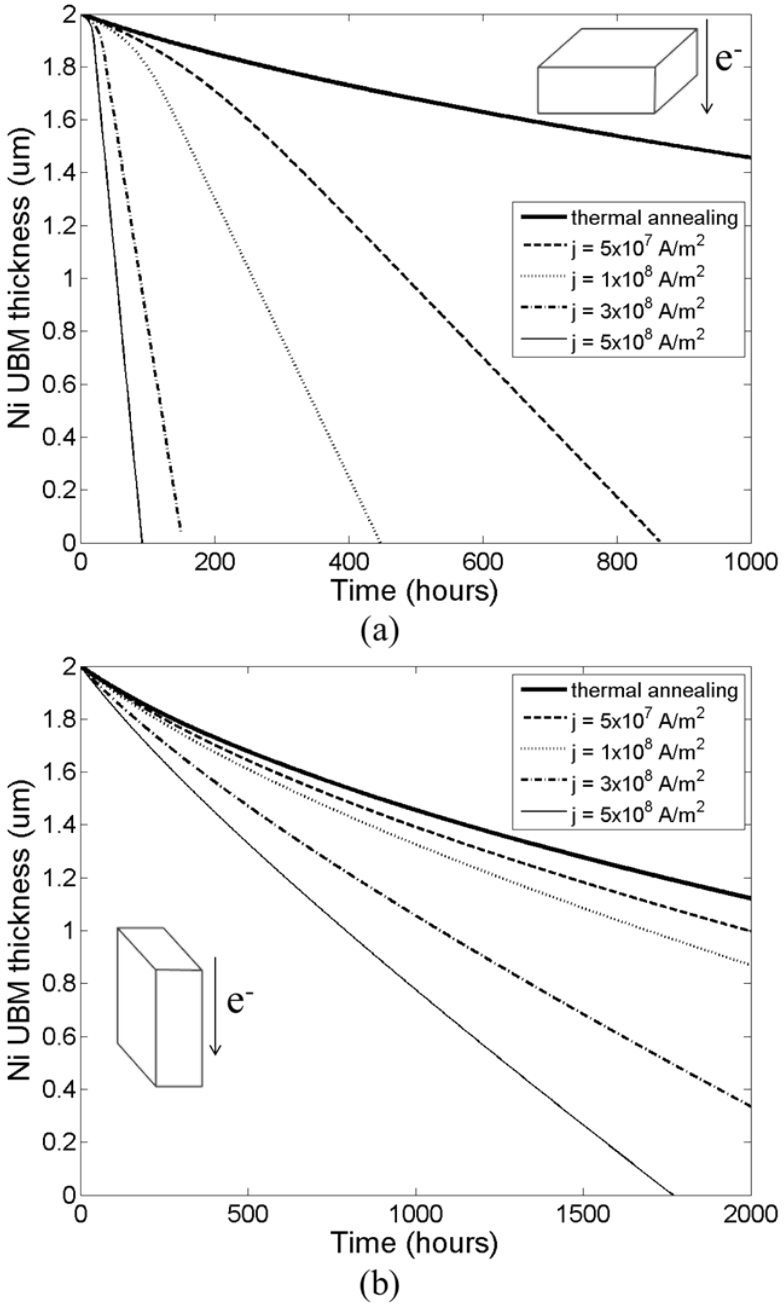

Figure 2.27: UBM consumption as a function of stressing time at four current densities when (a) $\theta = 0$, and (b) $\theta = 90^{\circ}$.

denoted as t_I. In general, t_I is less sensitive to Sn crystal orientations since the self-diffusion coefficient of Sn is not strongly anisotropic [39]. In fact, t_I is mainly determined by temperature and current density, and can best be described by the Black's equation [10]:

$$\text{MTTF} = Aj^{-n} \exp\left(\frac{Q}{kT}\right) \tag{2.13}$$

where MTTF is the mean time to failure, A is a constant, j is the current density, n is the current exponent, Q is the activation energy, k is the Boltzmann constant, and T is the absolute temperature. Figure 2.29 is an example showing the two competing failure mechanisms of solder EM in which the testing condition is $T = 170°\text{C}$, $j = 3 \times 10^8 \text{A/cm}^2$. In this example, t_I was estimated by values reported in Ref. [15], where $n = 2.1$, and $Q = 0.94$ eV. When $t_I < t_{II}$ under a specific temperature and current density, the solder joint is more likely to fail by Sn self-diffusion, or by the so-called Mode I failure mechanism. In the contrary, when $t_I > t_{II}$, the solder joint is more likely to fail by UBM depletion, or by the so-called Mode II failure mechanism. In this case, the effects of Sn grain orientation and EM on IMC formation need to be considered. Consequently, the Black's equation may not be accurate enough to predict the time to failure, because the parameter A in Eq. 2.13 is no longer a constant, but becomes a function of θ. In addition, the activation energy Q would be related to the mechanism of UBM depletion instead of Sn self-diffusion. In addition, it should be pointed out that the grain orientation at which the two curves intersect depends on temperature and current density. For example, results in Fig. 2.29 shows that the two

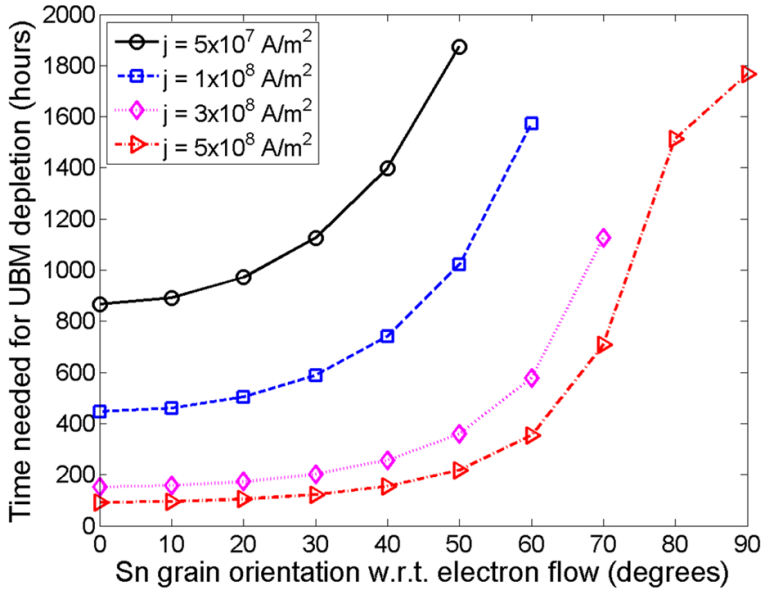

Figure 2.28: Time needed for UBM depletion as a function of Sn crystal orientation at four current densities.

curves representing different failure mechanisms intersect when the relative *c*-axis alignment with respect to the electron flow direction is about 50°. The value was associated with a specific test condition, and therefore was not a universal conclusion. Several approaches have been proposed in order to prevent Mode II early failures, including Zn doping [77], Cu additives to the Ni UBM [77], and multiple solder reflows [107], most of which are based on optimization of grain structure to retard the Ni consumption rate.

2.5 Summary

In this chapter, the effect of Sn grain structure on electromigration reliability of Pb-free flip chip solder joints were investigated.

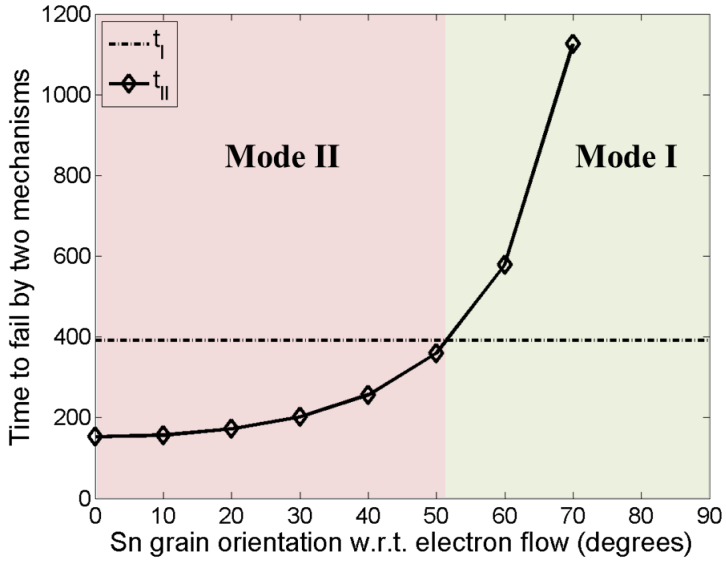

Figure 2.29: Time-to-fail prediction by two failure mechanisms. Test condition: $T = 170°C$, $j = 3 \times 10^8 A/cm^2$.

Sn grain structures were characterized using the EBSD technique to investigate the effect of number of solder reflows as well as thermal annealing. Material characterization showed that a single solder reflow during the assembly process produced solder joints with the majority of Sn grains with a large grain size and a random spread of grain orientations. Thermal annealing caused further grain coarsening. Four additional post-assembly reflows, on the other hand, yielded solder joints with a finer grain structure. More interlaced twin boundaries were observed. Thermal annealing in this case led to some grain growth, while the multi-grain feature remained. In addition, the grain orientation and grain size statistics were correlated with the EM failure results. It was found that the EM failure mode was closely re-

lated to the alignment between the *c*-axis of the Sn crystal and the electron flow direction. Single grain with its *c*-axis closely aligned to the electron flow is at the largest risk of early EM failure. Sn grain structural optimization was also explored. It was suggested that multi-grain structures with high-angle twin boundaries would be an effective approach to improve the EM reliability. The process of multiple solder reflows was thus proposed as one of such approaches.

In addition to the experimental work, a kinetic analysis was formulated to specifically study the early EM failure mechanism in Sn-based solder joints with Ni UBM. A numerical model was built to incorporate the anisotropic diffusion properties of the UBM materials in solder. Simulation results showed that when the *c*-axis of Sn has a close alignment to the current direction, IMC growth was enhanced by both electromigration and the extremely fast interstitial diffusion of Ni in Sn. The combined process resulted in IMC dissolution from the cathode side of the solder joint, which led to EM failure by UBM depletion. Numerical predictions were found to be consistent with the experimental observations, which provides a theoretical explanation for the EM degradation mechanisms.

Chapter 3

Estimation of Diffusion Coefficients Using Simulated Annealing

We avoid the gravest difficulties when, giving up the attempt to frame hypotheses concerning the constitution of matter, we pursue statistical inquiries as a branch of rational mechanics.

Josiah Willard Gibbs

3.1 Introduction

As was mentioned in Chaper 1, intermetallic formation is critical in controlling the reliability of Sn-based interconnects. This study will focus on solid-state intermetallic compound (IMC) growth. Many reports have indicated [102, 74, 105] that the solid-state IMC formation is induced by interdiffusion and phase transformation near the interface. When subject to current stressing, IMC growth can be enhanced by the electromigration driving force. In order to investigate the problem, a kinetic analysis was formulated as discussed in Chapter 2. The material parameters in the analysis include individual diffusion coefficients in the IMCs. These parameters, however, are not available in the literatures. This is not surprising since the

system under investigation involves multiple phases and more than one diffusion species, and so far there is no analytical solution to it. Due to the multi-component nature, the experimental measurements to determine the kinetics of IMC formation are equally complicated.

In this chapter, an efficient Monte Carlo simulation technique known as simulated annealing is applied to estimate the diffusion parameters by fitting the model with experimental data of IMC growth under thermal annealing. We report diffusion coefficients in Ni_3Sn_4 between 150 and 200°C, and those in Cu_6Sn_5 and Cu_3Sn between 120 and 200°C. The activation energies are determined. Together the results reported in this chapter will provide the diffusivity data to predict IMC growth and UBM consumption at any given temperature within the range.

This chapter will start with a literature survey on the measurement of diffusion coefficient in IMCs. Section 3.3 defines the problem and introduces the simulated annealing technique used to estimate the diffusion coefficients. Results and discussions will be presented in Section 3.4.

3.2 Diffusion Coefficients

The material parameters that control the mass transport and the IMC growth rate are the intrinsic diffusion coefficients. The temperature dependence of diffusivities follows the Arrhenius relationship

$$D = D_0 \exp\left(\frac{-Q}{RT}\right) \tag{3.1}$$

where D is the diffusion coefficient, D_0 is the frequency factor, Q is the activation energy, R is the gas constant, and T is the temperature in Kelvin.

In dilute solid solutions, the diffusion coefficient is determined by depositing a thin layer of radioactive tracer atoms B^* on the A surface and measuring the concentration evolution of B^* diffusing in pure A. Diffusion coefficients in dilute solid solutions are widely available in the literature. In concentrated solid solutions such as IMCs, the tracer method is difficult to apply, and usually, other methods and analysis are needed. Both Mei *et al.* [82] and Onishi and Fujibuchi [86] studied interdiffusion in Cu_6Sn_5 and Cu_3Sn phases with Cu/Sn diffusion couples, and reported the interdiffusion coefficients D in Cu_6Sn_5 and Cu_3Sn although the individual coefficients were not reported in their studies. Paul and his colleagues [87] conducted annealing experiments with Cu/Sn, Cu/Cu_6Sn_5 and Cu_3Sn/Sn diffusion couples and determined the tracer diffusion coefficients of the elements D^* between 150 and 350°C. Kumar and his coworkers [67] studied the Kirkendall effect in the Cu-Sn system by using inert markers, and determined intrinsic diffusion coefficients of Cu and Sn in Cu_6Sn_5 and Cu_3Sn at 200°C. Discrepancies were found in results reported by different groups due to errors coming from the non-planar morphologies of the interface and the non-planar distribution of the markers [67].

Table 3.1 shows the diffusion parameters of interest as reported in the literature. As can be seen from the table, the only available values in the IMC are the interdiffusion coefficients, while the individual diffusion

coefficients necessary for the kinetics analysis are not yet reported.

3.3 Determination of Diffusion Coefficients Using Simulated Annealing

3.3.1 Experimental Measurement

The experimental work described here was performed by an IBM research group. Thermal annealing experiments are performed on Pb-free solder bump structures. Two UBM materials were investigated: 10 µm Ni on 75 µm SnAg solder and 40 µm Cu on 40 µm SnAg solder. Figure 3.1 shows the SEM images of the as-received solder bumps. Figure 3.2 and 3.3 shows the experimental measurements of IMC growth in the Ni-Sn and Cu-Sn systems, respectively. The trend lines were empirically fit and were not generated by simulation. Several discrete points were randomly chosen at different locations on the samples for thickness measurement, and each data point was an average of five locations. The error bars resulted from uneven morphology of the IMC, but overall, the measurement gives a good average of the amount of IMC formation.

3.3.2 Kinetic Analysis

The derivation of the governing equations for IMC growth under thermal annealing is similar as given in Section 2.4.1. Figure 3.4 illustrates diffusion couples used to study Ni-Sn and Cu-Sn systems, respectively. In these systems, one intermetallic phase, Ni_3Sn_4, forms between pure Ni and

Table 3.1: Diffusion coefficients in the literature.

Type of diffusion	$D_0(\mathrm{m}^2/\mathrm{s})$	Q (kJ/mol)	Remark/ Reference
$D_{\text{Cu in (Cu)}}$	7.80×10^{-5}	210.9	[39]
	3.50×10^{-5}	203.6	
$D_{\text{Cu in (Sn)}}$	1.00×10^{-7}	16.7	$\parallel c$ [34]
	2.40×10^{-7}	33.1	$\perp c$ [34]
$D_{\text{Sn in (Sn)}}$	7.70×10^{-4}	107.1	$\parallel c$ [39]
	1.07×10^{-3}	105.0	$\perp c$ [39]
$D_{\text{Sn in (Cu)}}$	2.95×10^{-5}	177.0	[49]
$\widetilde{D}_{Cu_3Sn}$	1.43×10^{-8}	70.7	[86]
	5.48×10^{-9}	61.9	[82]
	3.20×10^{-6}	83.9	[32]
$\widetilde{D}_{Cu_6Sn_5}$	1.55×10^{-8}	64.8	[49]
	1.84×10^{-9}	53.9	[86]
$D_{\text{Ni in (Ni)}}$	1.27×10^{-4}	281.2	[39]
	9.20×10^{-5}	277.8	
$D_{\text{Ni in (Sn)}}$	1.99×10^{-6}	18.1	$\parallel c$ [109]
	1.87×10^{-4}	54.1	$\perp c$ [109]

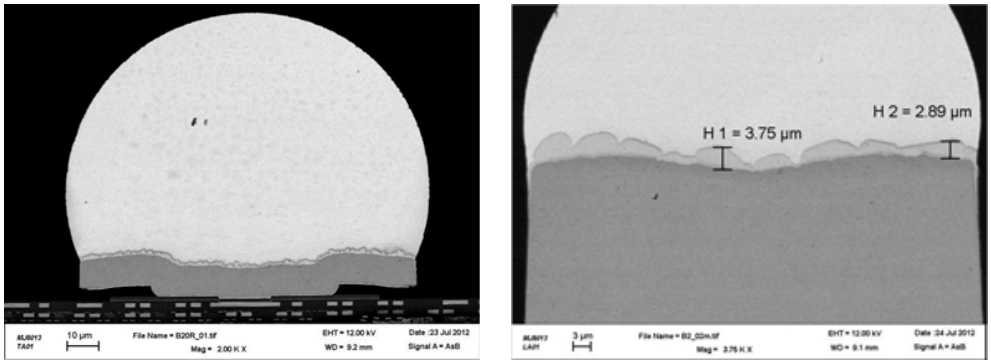

(a) (b)

Figure 3.1: SEM images of the as-received solder bumps: (a) Ni-Sn, and (b) Cu-Sn.

pure Sn phases, while two intermetallic phases, Cu_3Sn and Cu_6Sn_5, form between pure Cu and pure Sn phases.

Fick's second law gives the concentration evolution in the IMCs

$$\frac{\partial C}{\partial t} = \frac{\partial}{\partial z}\left(\widetilde{D}\frac{\partial C}{\partial z}\right) \tag{3.2}$$

$$\widetilde{D} = (1 - X_A)D_A + X_A D_B \tag{3.3}$$

where C is number of atoms per unit volume, t is time, z is thickness, $\widetilde{D}$ is the interdiffusion coefficient, X is the number of fraction of atoms, and D is the individual diffusion coefficient. In addition to interdiffusion, phase transformation takes place near the interface. The mass transport near the phase boundaries are described in Appendix B. Given the initial condition and boundary conditions, the concentration evolution can be solved. For the Ni-Sn system, the unknown parameters are the individual diffusion coefficients of Ni and Sn in the Ni_3Sn_4, while for the Cu-Sn system, there are

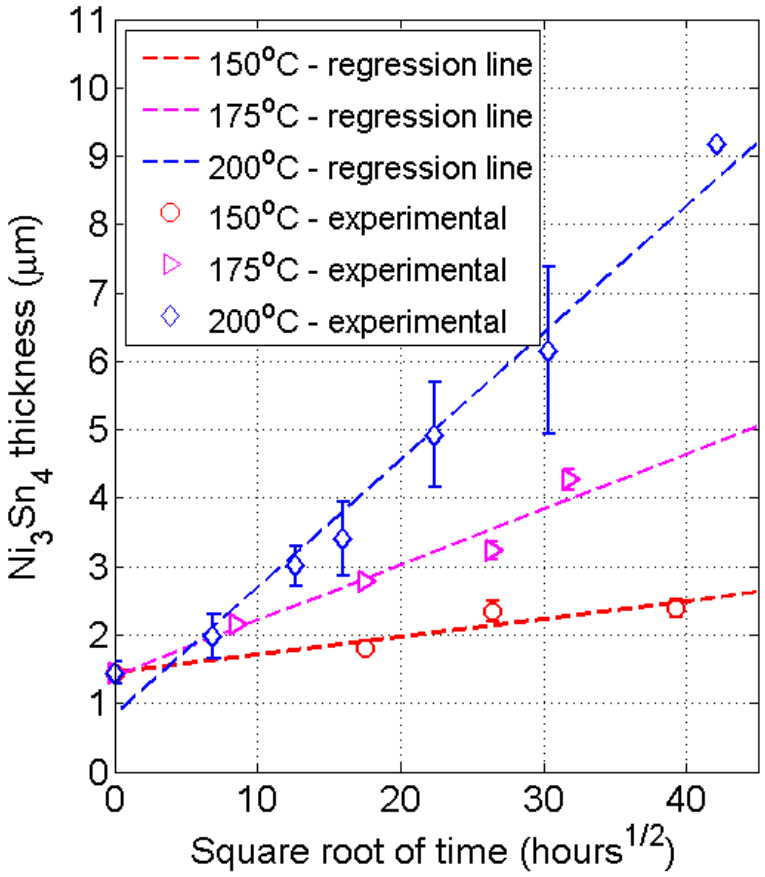

Figure 3.2: Experimental measurement of Ni_3Sn_4 growth during thermal annealing at three different temperatures.

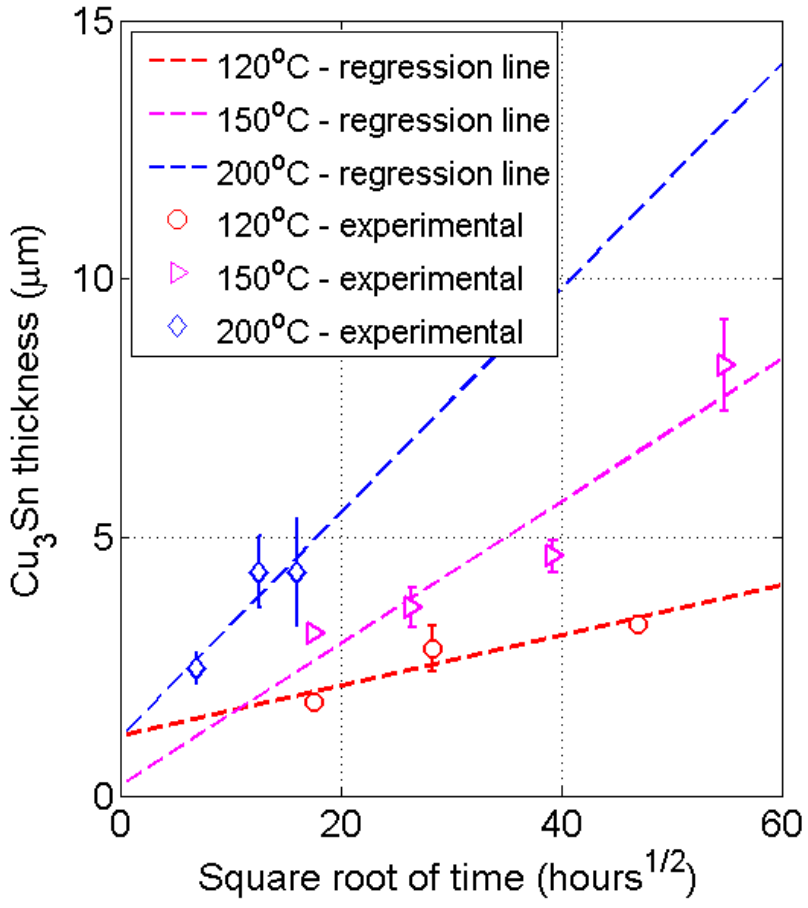

(a)

Figure 3.3: Experimental measurements of (a) Cu_3Sn growth during thermal annealing at three different temperatures.

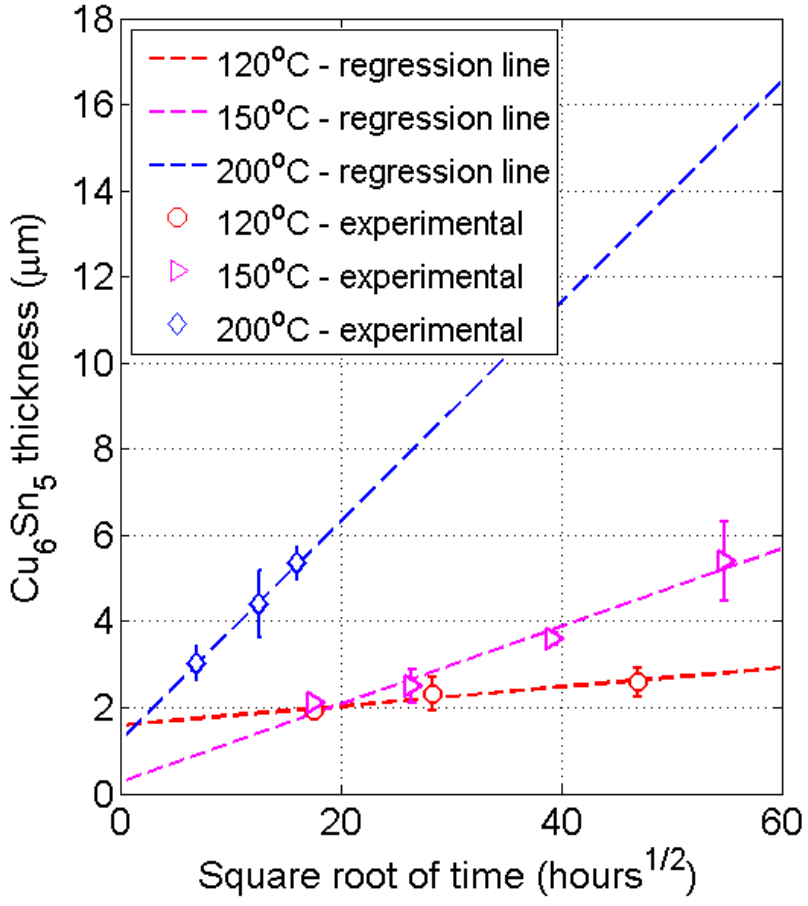

(b)

Figure 3.3: (Continued) Experimental measurements of (b) Cu_6Sn_5 growth during thermal annealing at three different temperatures.

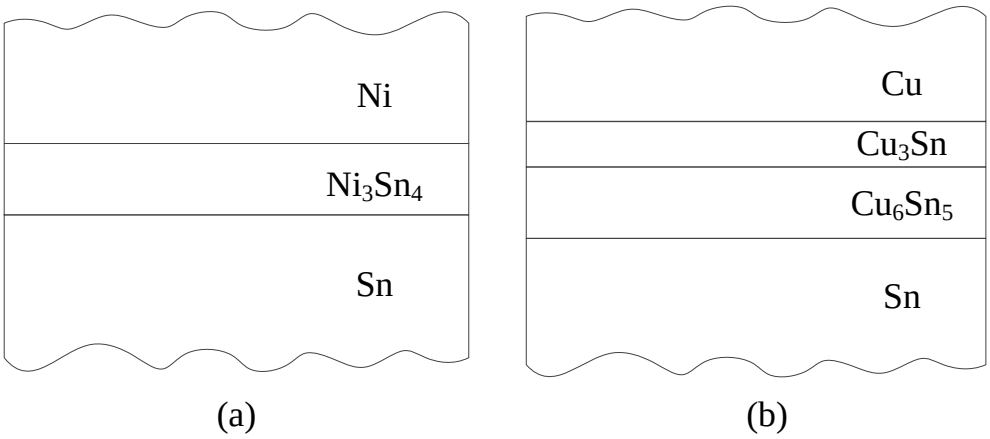

Figure 3.4: Schematics of diffusion couples for (a) Ni-Sn, and (b) Cu-Sn systems under thermal annealing.

four unknown parameters, i.e., the individual diffusion coefficients of Cu and Sn in Cu_3Sn and Cu_6Sn_5, respectively.

3.3.3 Problem Definition

Given the experimental measurement and an appropriate model to describe the physical process, the remaining question is whether there is a mathematical method whereby the unknown parameters can be obtained. This is an inverse problem [101] where the model parameters are to be inferred from observed measurements. A heuristic method is needed to find the optimal solution when the model prediction fits best with the experimental measurement.

Recently Chao *et al.* [17] proposed to apply the simulated annealing

technique to estimate material parameters for IMCs in Pb-free flip chip solder joints with Cu UBM at 150°C. They have shown that the simulated annealing technique is efficient in analyzing the IMC formation in the Cu-Sn system. In their report, however, the diffusion coefficients were characterized for a single temperature and thus the activation energy was not able to be extracted. Moreover, the kinetics analysis for the Ni-Sn system was not included in their study, although Ni has been demonstrated as an effective UBM material in addition to Cu.

The present study follows the simulated annealing method developed by Chao to estimate the diffusion coefficients for the pertinent IMCs, as well as to determine the activation energies of the temperature dependent parameters.

3.3.4 Generic Simulated Annealing Algorithm

Simulated annealing, first proposed by Kirkpatrick *et al.* [63], is an optimization approach capable of finding the global minimum of a function. Since its first introduction, simulated annealing has been applied to many complex optimization problems such as image processing [13], floor planning in very large-scale integration (VLSI) design [46], and molecular physics and chemistry [42]. In this chapter, simulated annealing is applied to estimate the diffusion coefficients of IMCs from experimentally measured IMC growth under thermal annealing. The generic algorithm of the approach is given below, and detailed procedures and results are presented in

the following sections.

A simple schematic in Fig. 3.5 shows the simulated annealing process, where the objective function is optimized by finding its global minimum. Given an initial solution ω, it tries to search for an optimal solution with the smallest objective function. Compared with the standard "greedy" algorithm, the simulated annealing technique allows perturbation to move uphill in a controlled manner to escape from local minima, L. For a "greedy" approach, it interactively searches for a neighboring solution with an objective function smaller than the current configuration until such a neighboring solution cannot be found. However, it is likely that the result we get would be a local minimum, L, instead of the true global minimum, G, as illustrated in Fig. 3.5. A practical way in applying the "greedy" algorithm is therefore to repeat the process multiple times starting with different initial solutions in the search space, and a final solution is manually picked with the smallest objective function.

Different from the "greedy" approach, simulated annealing provides a non-zero probability to move from a current solution to a neighboring solution with a higher objective function. This characteristic is analogous to thermally activated atoms during the physical annealing process, where it is possible for atoms to jump to a higher energy state, and the probability depends on the height of the energy barrier and the temperature. At high temperature, the atoms are more thermally activated and thus have more freedom to move around. As the annealing temperature gradually reduces,

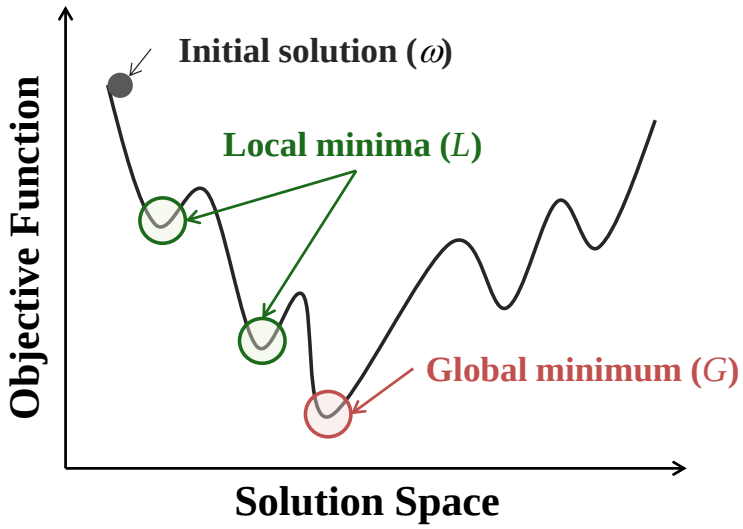

Figure 3.5: Illustration of simulated annealing.

the atoms will eventually reach an equilibrium state. Analogously, in the simulated annealing algorithm, a nominal temperature, T, gradually decreases from the "melting temperature", T_m, to the "freezing temperature", T_f, according to the annealing schedule. After defining the search space, the simulation starts with a random parameter set, ω. In each iterative step, a neighboring solution is selected. The new parameter set is denoted ω'. The objective functions, F, are calculated for the current state, ω, and the attempted new state, ω'. The probability to accept a new state is determined based on the Metropolis criterion [84]

$$\text{Prob}(\omega \to \omega') = \begin{cases} 1 & : \Delta F \leqslant 0 \quad \text{(down-hill move)} \\ \exp(-\Delta F/T) & : \Delta F > 0 \quad \text{(up-hill move)} \end{cases} \tag{3.4}$$

where $\Delta F = F(\omega') - F(\omega)$, and T is the current temperature. Eq. 3.4 indi-

cates that the probability is one when the new state has a smaller objective function than the current one, which means that a down-hill move is always accepted. When $F(\omega') > F(\omega)$, on the other hand, the attempted state will be accepted with the probability $e^{(-\Delta F/T)}$. The smaller the ΔF and the higher the temperature, the larger the acceptance probability is. The implementation of the Metropolis criterion allows the system to escape from local minima. This up-hill moving capability makes the simulated annealing approach more advantageous over the greedy method. Algorithm 1 summarizes the generic algorithm of simulated annealing.

Algorithm 1 Generic Simulated Annealing Algorithm

Define the search space, Ω.
Get an initial parameter set, $\omega \in \Omega$. $\omega_{\text{best}} \leftarrow \omega$
Calculate the objective function, $F(\omega)$
Define the initial temperature, T_m. $T \leftarrow T_m$
while $i \leqslant$ numbers of iteration **and** $F(\omega) > F_{\text{threshold}}$ **do**
  Perturb the configuration to obtain a neighboring ω' from ω
  Calculate the objective function, $F(\omega')$
  $\Delta F = F(\omega') - F(\omega)$
  if $\Delta F \leqslant 0$ **then**
    $\omega \leftarrow \omega'$
  else
    $\omega \leftarrow \omega'$ with the probability $e^{(-\Delta F/T)}$
  end if
  $\omega_{\text{best}} \leftarrow \omega$
  Update temperature
  $i + 1$
end while
return ω_{best}

There are four basic ingredients in the algorithm: (1) search space,

(2) neighboring structure, (3) objective function, and (4) annealing schedule. These are discussed in the following sections specifically aimed at the problem of diffusivity estimation in Cu-Sn and Ni-Sn IMC systems.

3.3.5 Search Space

The search space in the simulation is dentoed Ω. For each parameter set $\omega \in \Omega$,

$$\omega = \{p_1, p_2, ..., p_n\} \tag{3.5}$$

where ps are individual parameters. The parameters to be estimated are the individual diffusion coefficients of Cu and Sn atoms in the Cu_6Sn_5, and Cu_3Sn IMCs in the Cu-Sn system, and those of Ni and Sn atoms in the Ni_3Sn_4 in the Ni-Sn system. Therefore, the parameter set for the two systems can be expressed as

$$\omega_{\mathrm{Ni}} = \{D^{(1)}_{\mathrm{Ni}}, D^{(1)}_{\mathrm{Sn}}\} \tag{3.6}$$

$$\omega_{\mathrm{Cu}} = \{D^{(2)}_{\mathrm{Cu}}, D^{(2)}_{\mathrm{Sn}}, D^{(3)}_{\mathrm{Cu}}, D^{(3)}_{\mathrm{Sn}}\} \tag{3.7}$$

where the numbers in the superscript represent different phases. The search space used in the simulation is from 1×10^{-20} to 1×10^{-10} $\mathrm{m}^2/\mathrm{sec}$.

3.3.6 Neighborhood Structure

During the search process, the simulation repeatedly attempts to find a better solution by moving to a neighbor with a lower objective function. The way in which the metaheuristic moves from one solution to its neighbor

is a critical component in simulated annealing. In each iterative step, one parameter, p_i, is randomly picked. The neighborhood size is defined as

$$N = \{p_i | p_i(1 - r_i) \leq p_i \leq p_i(1 + r_i)\} \tag{3.8}$$

where r_i is the neighborhood radius, which is chosen to be 0.05 in this study. A new parameter, p_i', is obtained based on the neighborhood function

$$p_i' = \text{rand}(N \cap \Omega) \tag{3.9}$$

This generates a new parameter set, $\omega' \in \Omega$.

3.3.7 Objective Function

The objective function, $F(\omega)$, calculates the residual sum of squares (RSS), i.e., the discrepancy between the experiment measurement and the numerical prediction of IMC thicknesses with a given set of model parameters, ω. Therefore the objective function can be expressed as

$$F(\omega) = \frac{1}{N} \sqrt{\sum_{i=1}^{N} \left(\frac{d_i(\omega) - d_{i,\text{exp}}}{d_{i,\text{exp}}} \right)^2} \tag{3.10}$$

where $d(\omega)$ is the IMC thickness numerically derived from the kinetic model, d_{exp} is the IMC thickness measured from the annealing experiment, and i is the running index for each observation time. d_{exp} was obtained from the experimental results presented in Section 3.3.1. $d(\omega)$ was calculated based on the kinetic analysis described in Section 3.3.2.

3.3.8 Annealing Schedule

An annealing schedule is defined to simulate the physical process of annealing. The nominal temperature, T, starts with an initial "melting temperature", T_m. The value of T_m in this study is one, which is comparable to the value of objective function when model prediction is significantly deviated from truth. Therefore, $T_m = 1$ is sufficient for the system to escape from local minima. At each iterative step, the temperature is decreased by

$$T_i = mT_{i-1} \tag{3.11}$$

where $0 < m < 1$. m is usually larger than 0.8 to ensure enough time for the system to find the equilibrium state. The annealing process stops at a "freezing temperature" $T_f = 10^{-6}$. The value 10^{-6} is chosen so that uphill move is greatly improbable towards the end of the simulation. Given the number of iteration, m can be calculated.

Figure 3.6 shows the annealing schedule employed in this study. Figure 3.7 shows an example plot of the objective function versus numbers of iteration. As is seen in Fig. 3.7, a significant amount of uphill move is observed at the beginning of the annealing process, while only downhill moves are accepted towards the end.

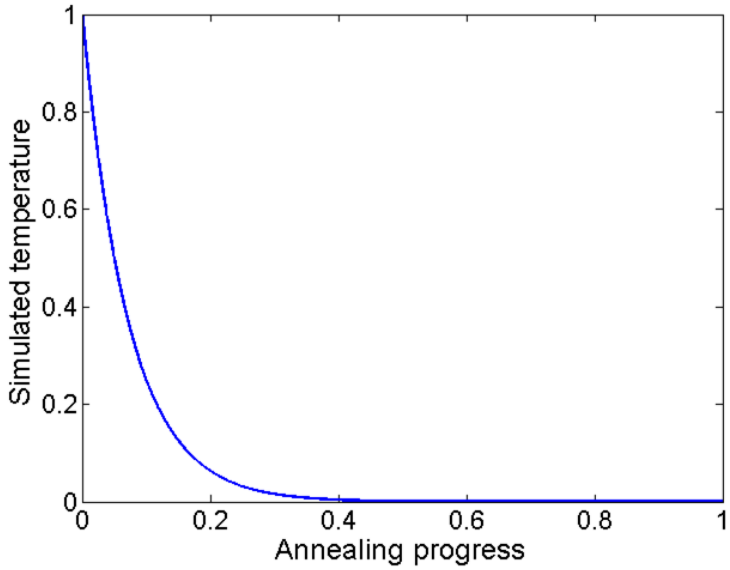

Figure 3.6: Annealing schedule.

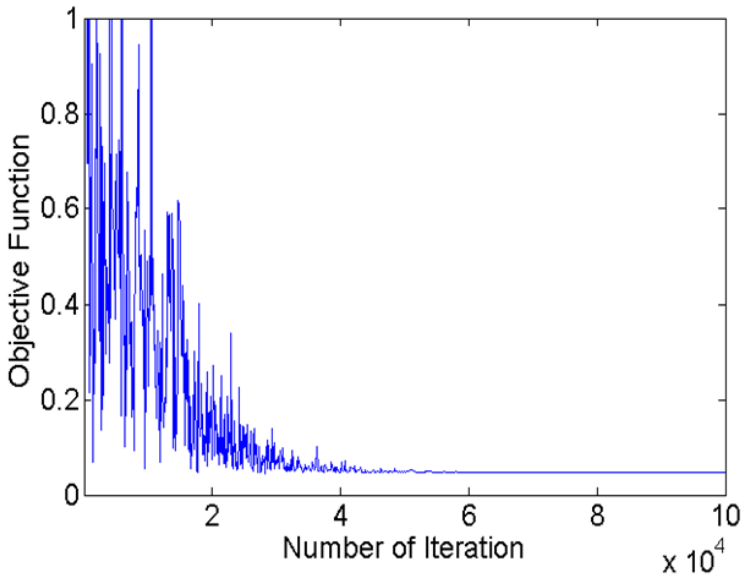

Figure 3.7: An example plot of the objective function versus numbers of iteration

Table 3.2: Deduced intrinsic diffusion coefficients and calculated interdiffusion coefficients in Ni_3Sn_4 IMC.

T (°C)	Species	$D(m^2/s)$	$D_{int}(m^2/s)$
150	Ni	1.04×10^{-17}	8.64×10^{-18}
	Sn	6.29×10^{-18}	
175	Ni	6.29×10^{-17}	4.54×10^{-17}
	Sn	2.20×10^{-17}	
200	Ni	1.52×10^{-16}	1.29×10^{-16}
	Sn	9.90×10^{-17}	

3.4 Results and Discussions

3.4.1 Ni-Sn System

Table 3.2 shows the diffusion coefficients estimated from simulated annealing for Ni and Sn atoms in Ni_3Sn_4. In addition, the table lists interdiffusion coefficients calculated based on Eq. (3.3). Figure 3.8 shows the simulation results of Ni_3Sn_4 growth under thermal annealing in comparison with the experimental data. The overall agreement between the experimental data and the predicted IMC thickness is reasonably good.

The temperature dependence of the diffusion coefficients can be determined from Eq. (3.1) by knowing the activation energies, which can be estimated from the slope of the Arrhenius plots. Figure 3.9 plots $\ln(D_{Ni})$ and $\ln(D_{Sn})$ vs. $1/T$, respectively, and Fig. 3.10 plots $\ln(D_{int})$ vs. $1/T$. The activation energies were calculated to be 0.93 ± 0.15 eV and 0.95 ± 0.08 eV

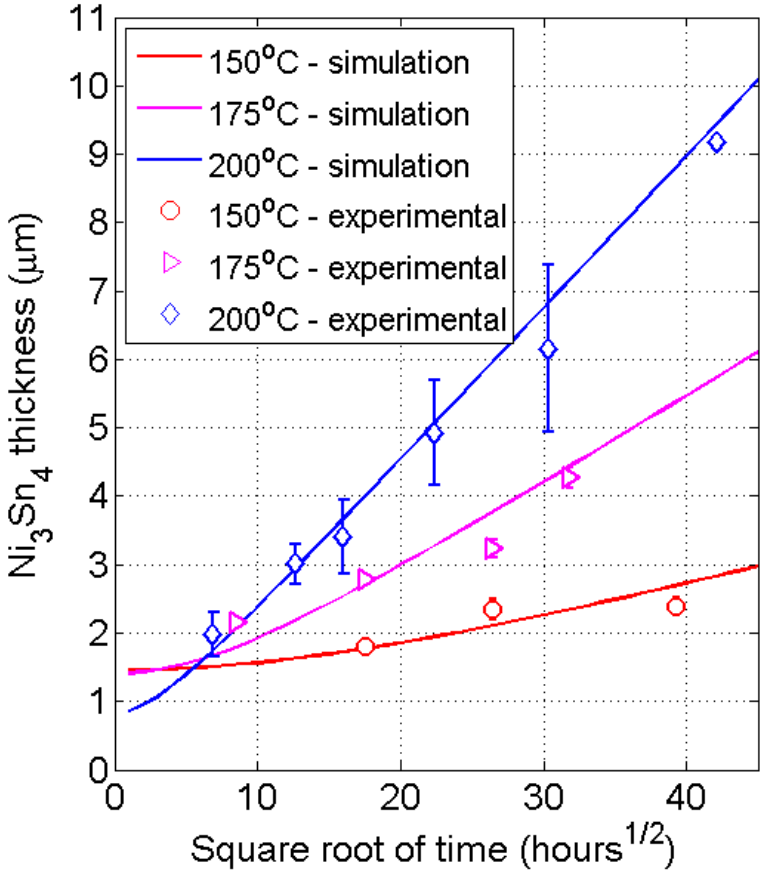

Figure 3.8: Experimental and simulated Ni_3Sn_4 growth during thermal annealing.

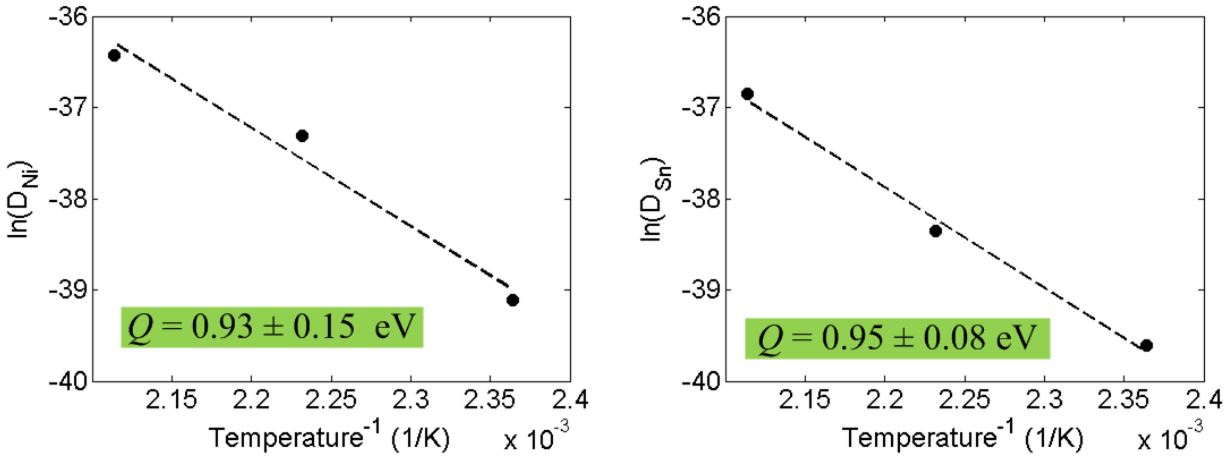

Figure 3.9: Arrhenius plots of intrinsic diffusion coefficient of (a) Ni in Ni_3Sn_4; (b) Sn in Ni_3Sn_4.

for Ni and Sn in Ni_3Sn_4, respectively, and 0.94 ± 0.09 eV for the interdiffusion coefficient. Here the upper and lower bounds in the activation energies were expressed using the standard deviation.

IMC growth can also be characterized by

$$y = y_0 + kt^n \tag{3.12}$$

where y is the IMC thickness, y_0 is the initial thickness at $t = 0$, k is the growth rate constant, and n is the time exponent. It has been widely accepted that $n = 0.5$ if diffusion is the rate controlling mechanism. The growth rate constant k can be estimated from Fig. 3.2, and the results are summarized in Table 3.3.

Since k^2 has the same unit as diffusivity, it follows the Arrhenius

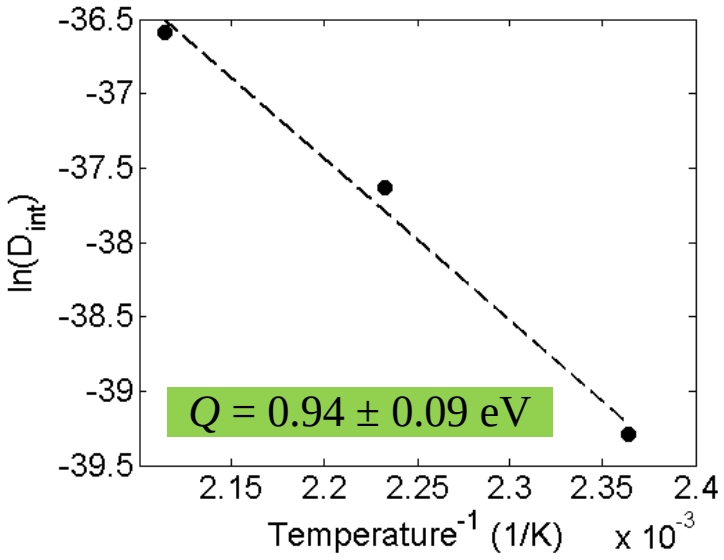

Figure 3.10: Arrhenius plot of the interdiffusion coefficient in Ni_3Sn_4 IMC.

Table 3.3: Growth rate constant, k (in $\mu m/s^2$), for Ni_3Sn_4 under thermal annealing.

Temperature (°C)	Growth rate constant
150	0.0004
175	0.0014
200	0.0027

equation:

$$k^2 = k_0^2 \exp(-\frac{Q}{RT}) \tag{3.13}$$

where k^2 is the square of the growth rate constant, k_0^2 is the pre-exponential factor, Q is the apparent activation energy, R is the gas constant, and T is the temperature. The Arrhenius plot for Ni_3Sn_4 growth is shown in Fig. 3.11. The apparent activation energy was determined to be 1.32 ± 0.19 eV. The value of the apparent activation energy for Ni_3Sn_4 growth is higher than that of the diffusion coefficients. The difference in the two activation energies could be due to the fact that the model used in this study only accounts for the kinetic mechanisms to produce phase transformation. For example, the interface migration rate is determined based on mass transport of the atoms near the interface. However, phase transformation is a combined cause of both kinetic mechanisms and thermodynamic driving forces. The necessary condition for a spontaneous intermetallic formation relates directly to the energy difference of the system upon transformation. Therefore, Eq. (3.13) can be re-written by combining the two factors,

$$k^2 = k_0^2 \exp(-\frac{Q + |\Delta H|}{RT}) \tag{3.14}$$

where Q is the activation energy for diffusion, and ΔH is the enthalpy of forming Ni_3Sn_4. The hypothesis can be confirmed by knowing the enthalpy of formation for the intermetallic. Literature values for Ni_3Sn_4 are in the range of -33.7 to -25.3 kJ/mol [38], corresponding to -0.35 to -0.26 eV. The negative value means that the IMC formation reduces the enthalpy of the

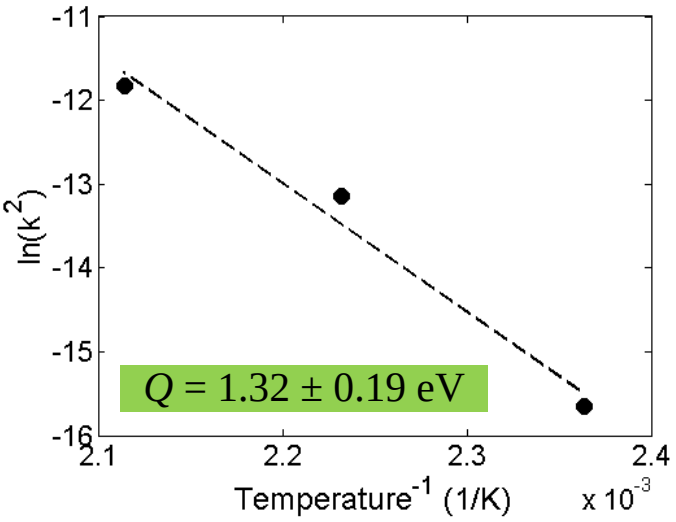

Figure 3.11: Arrhenius plot of $\ln(k^2)$ vs. $1/T$ for Ni_3Sn_4 growth.

system. This makes the sum of the absolute values of Q and ΔH around 1.3 eV.

3.4.2 Cu-Sn System

Table 3.4 and 3.5 summarize the estimated intrinsic diffusion coefficients in Cu_3Sn, and Cu_6Sn_5, respectively. These parameters are not available in the literature. However, several groups have reported the interdiffusion coefficients in the Cu-Sn alloying system, and thus the calculated interdiffusion coefficients as well as the literature reports are listed in the tables for comparison. It is clear that the simulation results are in good agreement with the literature values, serving as an indirect validation for the study.

Figure 3.12 shows the simulated Cu_3Sn and Cu_6Sn_5 growth along with the experimental data, suggesting that the numerical predictions were consistent with the experiments.

Table 3.4: Estimated intrinsic diffusion coefficients in Cu_3Sn IMC and calculated interdiffusion coefficients in comparison with literature values.

T (°C)	Species	$D(m^2/s)$	$D_{int}(m^2/s)$	D_{int}[literature](m^2/s) [86, 32, 82]
120	Cu	1.40×10^{-17}	3.32×10^{-17}	$5.47 \times 10^{-18} \sim 3.29 \times 10^{-17}$
	Sn	3.96×10^{-17}		
150	Cu	1.58×10^{-16}	1.29×10^{-16}	$2.66 \times 10^{-17} \sim 1.39 \times 10^{-16}$
	Sn	1.19×10^{-16}		
200	Cu	7.43×10^{-16}	7.03×10^{-16}	$2.23 \times 10^{-16} \sim 1.73 \times 10^{-15}$
	Sn	6.89×10^{-16}		

Table 3.5: Estimated intrinsic diffusion coefficients in Cu_6Sn_5 IMC and calculated interdiffusion coefficients in comparison with literature values.

T (°C)	Species	$D(m^2/s)$	$D_{int}(m^2/s)$	D_{int}[literature](m^2/s) [86, 82]
120	Cu	3.80×10^{-17}	3.15×10^{-17}	$3.78 \times 10^{-17} \sim 1.25 \times 10^{-16}$
	Sn	2.60×10^{-17}		
150	Cu	1.05×10^{-16}	1.33×10^{-16}	$1.54 \times 10^{-16} \sim 4.04 \times 10^{-16}$
	Sn	1.57×10^{-16}		
200	Cu	1.12×10^{-15}	9.94×10^{-16}	$1.08 \times 10^{-15} \sim 2.04 \times 10^{-15}$
	Sn	8.88×10^{-16}		

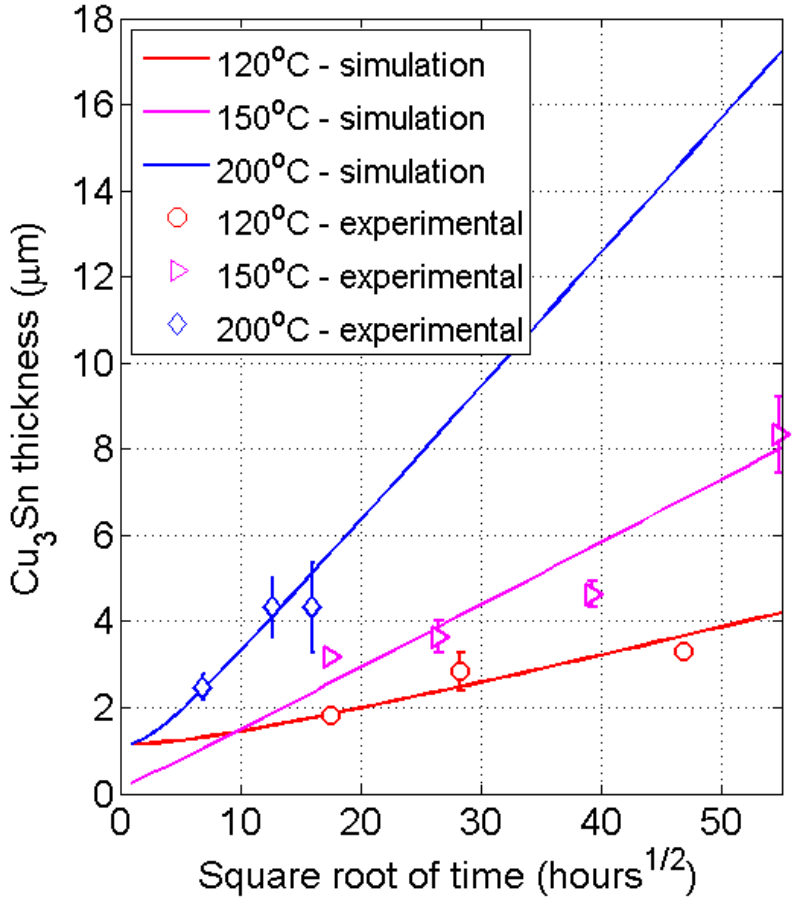

(a)

Figure 3.12: Experimental and simulated results of (a) Cu_3Sn growth during thermal annealing.

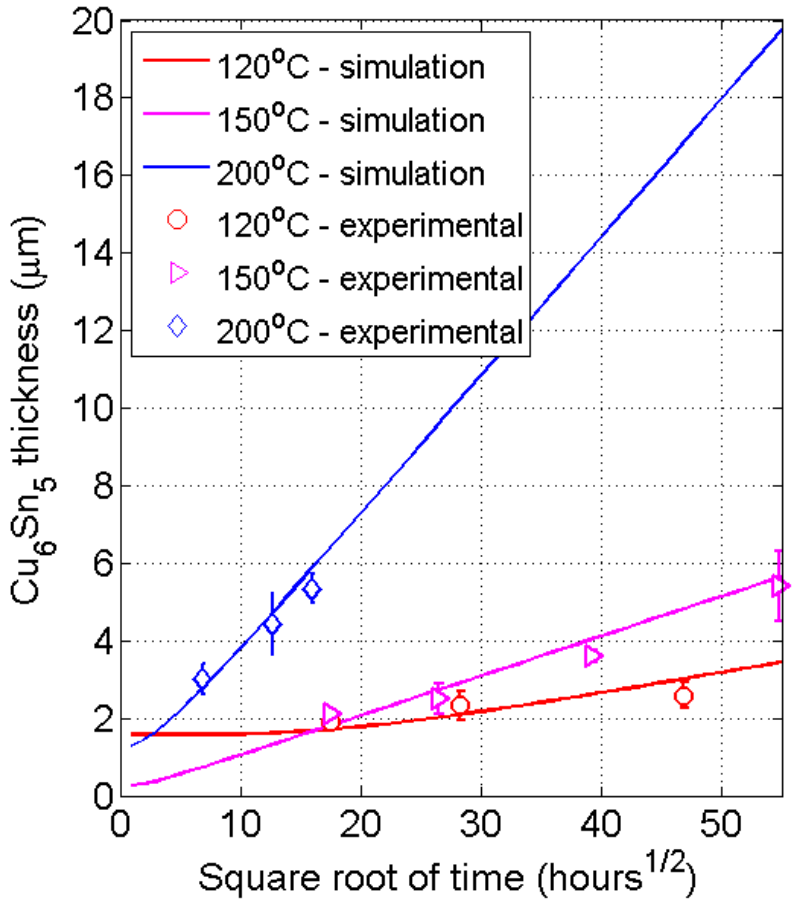

(b)

Figure 3.12: (Continued) Experimental and simulated results of (b) Cu_6Sn_5 growth during thermal annealing.

Table 3.6: Activation energies (in eV), for interdiffusion coefficients in Cu_3Sn and Cu_6Sn_5 obtained from this study as well as other references.

	Cu_3Sn	Cu_6Sn_5	Temperature range (°C)
Onishi [86]	0.73	0.67	190∼220
Mei [82]	0.64	0.56	190∼220
This study	0.61 ± 0.02	0.69 ± 0.001	120∼200

Following a similar analysis for the Ni-Sn system, the activation energies were obtained by Arrhenius plots as shown in Fig. 3.13 for intrinsic diffusion coefficients. Figure 3.13 shows that in Cu_3Sn, Sn has a smaller activation energy than Cu, suggesting that Sn diffusion dominates at lower temperatures, while Cu diffusion dominates at higher temperatures. On the other hand, Cu and Sn diffusion has comparable activation energies in Cu_6Sn_5.

Figure 3.14 shows the Arrhenius plot for the interdiffusion coefficients. The activation energies for the interdiffusion coefficients were determined to be 0.61 ± 0.02 and 0.69 ± 0.001 eV in Cu_3Sn, and Cu_6Sn_5, respectively. These values are in reasonably good agreement with those reported by Onishi [86] and Mei [82], as listed in Table 3.6. The difference in activation energies in different studies could be due to the fact that IMC growth were measured under a different temperature range. Results reported in [86] and [82] were based on IMC growth from 190 to 220°C, while results in this study were based on IMC growth from 120 to 200°C.

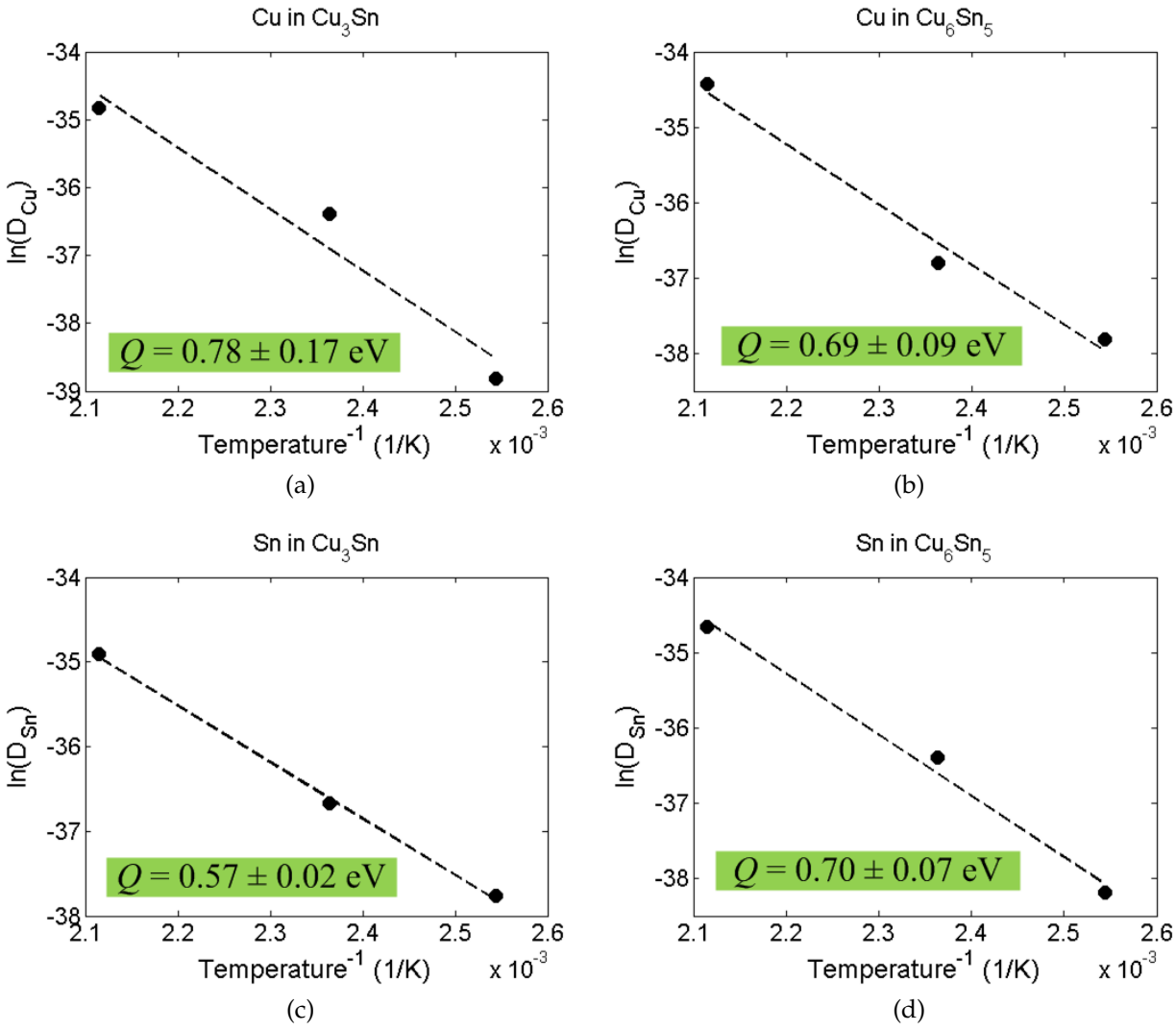

Figure 3.13: Arrhenius plots of intrinsic diffusion coefficient of (a) Cu in Cu_3Sn; (b) Cu in Cu_6Sn_5; (c) Sn in Cu_3Sn; (d) Sn in Cu_6Sn_5.

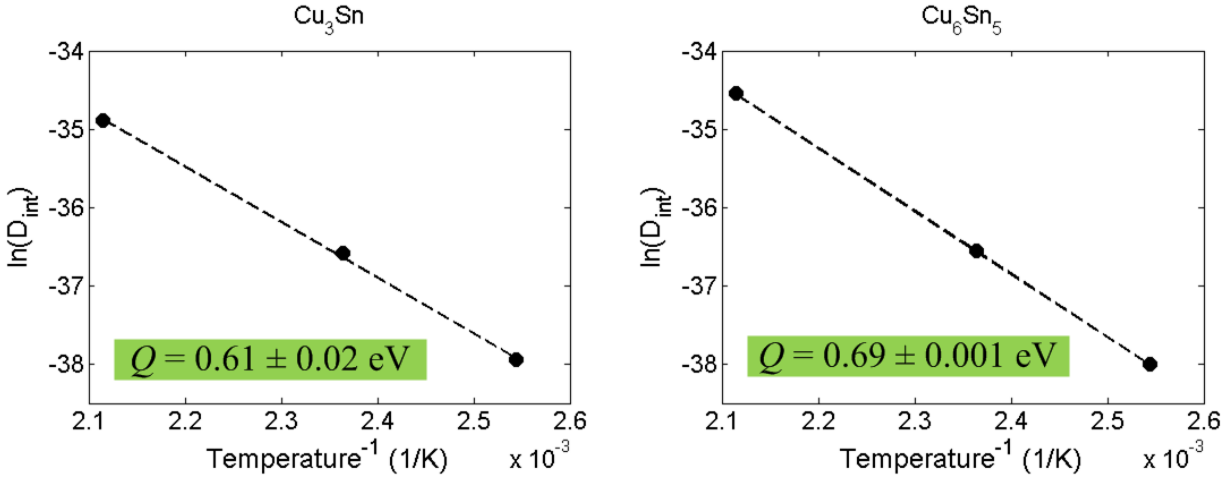

Figure 3.14: Arrhenius plots of interdiffusion coefficient of (a) Cu_3Sn; (b) Cu_6Sn_5.

Table 3.7: Growth rate constant, k (in $\mu m/s^2$), for Cu_3Sn and Cu_6Sn_5 under thermal annealing.

Temperature (°C)	Cu_3Sn	Cu_6Sn_5
120	0.0008	0.0004
150	0.0023	0.0015
200	0.0036	0.0042

The growth rate constants according to Eq (3.12) for Cu-Sn IMC were determined based on the experimental data, and results are shown in Table 3.7. Figure 3.15 shows the Arrhenius plot for $\ln(k^2)$ vs. $1/T$.

By comparing the activation energies for interdiffusion and IMC growth, it is found that the two activation energies are comparable for Cu_3Sn (0.61 ± 0.02 eV vs. 0.58 ± 0.19 eV), while in the case of Cu_6Sn_5, the activation energy

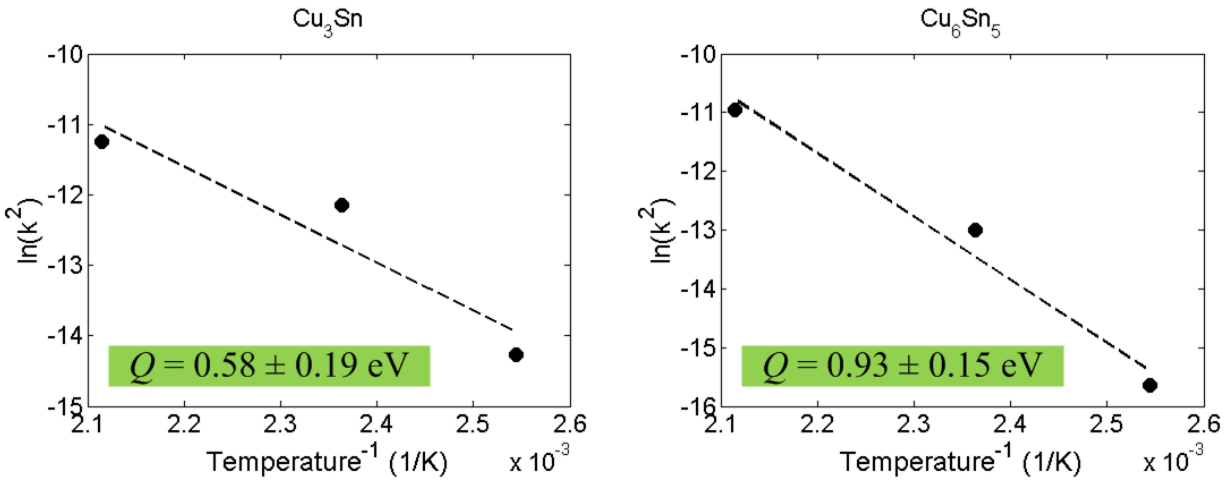

Figure 3.15: Arrhenius plots of $\ln(k^2)$ vs. $1/T$ for (a) Cu_3Sn; and (b) Cu_6Sn_5 growth.

for IMC growth (0.93 ± 0.15 eV) is larger than that for diffusion (0.69 ± 0.001 eV). The enthalpy of formation for Cu_3Sn and Cu_6Sn_5 are summarized in Table 3.8, which suggests that ΔH in Cu-Sn IMCs are relatively small. These combined results can explain the Cu_3Sn case fairly well, indicating that Cu_3Sn growth is dominated by the kinetic process. However, results from the kinetic analysis cannot explain the Cu_6Sn_5 case. One possibility for the discrepancy may be due to sidewall wetting during Cu-Sn IMC growth as shown in Fig. 3.16. The model was formulated based on one-dimensional diffusion. When it is applied to the two-dimensional diffusion case, errors can be added to the results. In addition, other factors may affect the results, such as errors in experimental measurements, or other thermally activated processes can be involved in Cu_6Sn_5 formation. More study is required to

Table 3.8: Literature reports on enthalpy of formation (in eV) for Cu_3Sn and Cu_6Sn_5.

Cu_3Sn	Reference	Cu_6Sn_5	Reference
-0.08 ± 0.01	[38]	-0.06 ± 0.01	[38]
-0.08 ± 0.002	[64]	-0.07 ± 0.005	[41]
-0.08 ± 0.002	[51]		
-0.08 ± 0.002	[54]		

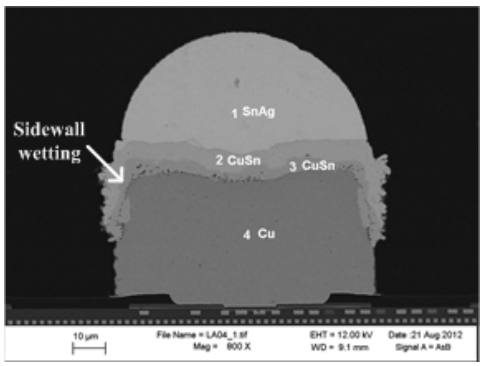

Figure 3.16: Cross-sectional SEM image of an annealed Cu-Sn solder bump at 170°C for 256 hours.

better understand the problem.

3.5 Summary

In this chapter, a kinetic analysis was developed to investigate IMC formation in Pb-free solder joints with Ni and Cu metallization. Thermal annealing experiments were performed by IBM on Pb-free solder joints with two different UBM structures, i.e., Ni and Cu. The samples were annealed under three different temperatures, and IMC thicknesses were measured

as a function of time. The results showed that Ni_3Sn_4 was formed in the Ni-Sn diffusion couple, while the Cu-Sn diffusion couple consisted of two intermetallics, i.e., Cu_3Sn and Cu_6Sn_5. All the IMCs followed a parabolic growth law during thermal annealing.

A numerical model was built to describe the interdiffusion and phase transformation, where the intrinsic diffusion coefficients in the model were not readily available from literature. An effective Monte Carlo method known as simulated annealing was thus applied to estimate the unknown parameters. The intrinsic diffusion coefficients were estimated by fitting the experimental results to find the best match between simulation and experiments.

The parameters estimated from the simulated annealing method were then used as an input to the numerical model in order to analyze IMC growth. The simulation results were found to be consistent with the experimental data, which served as a validation for the method used in this study. The activation energies of the diffusion coefficients were obtained by using the Arrhenius relationship for the temperature dependent parameters. These results provide a useful database to predict IMC growth at any temperature within the temperature range. A comparison between Ni and Cu metallization also provides useful information for material selection of UBM metallization in Pb-free solder joints.

Chapter 4

Electromigration Reliability of Sn-based TSV Microbump Joints in 3D Integration

New technology will not necessarily replace old technology, but it will date it. Eventually, it will replace it. But it's like people who had black-and-white TVs when color came out. They eventually decided whether or not the new technology was worth the investment.

Steve Jobs

4.1 Introduction

Microbumping is one of the key technologies in 3D integration [111]. This technology, together with through-silicon-vias (TSVs), forms electrical connections between stacked dies in a 3D integrated circuits. As the I/O counts increase and the pitch size decreases, material selection for the bonding metallurgy and reliability of the fine-pitch interconnect joining have become critical issues in 3D chip stacking. Fine-pitch silicon-to-silicon stacking approaches include transient liquid phase (TLP) bonding resulting in intermetallic compound (IMC) after joining [108], metal to metal (Cu-Cu)

bonding by thermal compression [20], and micro-controlled collapse chip connection (μ-C4) or microbumps through mass reflow or thermal compression [114, 78].

Sn-based microbumps are currently used by the microelectronic industry due to its process compatibility with the current assembly technologies. With the joint size significantly smaller than the C4 solder joints and the need to increase the current density, electromigration (EM) has emerged as a critical reliability concern and has drawn considerable interests [50, 73, 99, 113, 68]. In Sn-based C4 solder joints, IMC formation resulting from material reactions between Sn and the under-bump metallurgy (UBM) was found to be enhanced under EM and played an important role in controlling the solder reliability [75, 107]. For 3D chip stacking interconnection, the solder volume is substantially reduced because of package miniaturization and fine-pitch requirements. The limited supply of Sn induces more extensive IMC formation and can convert the entire bump into IMC upon thermal annealing or under current stressing. The extensive IMC growth in Sn-based microbumps gives rise to EM characteristics distinctly different from that of C4 solder joints. In this chapter, the EM reliability of TSV microbump joints in 3D interconnects will be studied. Emphasis will be placed on the effect of metallurgical selection and intermetallic formation on microbump EM reliability.

4.2 Experimental Details

4.2.1 Test Vehicles

EM tests were performed on four-point Kelvin structures of TSV microbump joints in chip-on-chip test vehicles (TVs) that were provided by Texas Instruments. The microbumps were composed of Sn-2.5Ag (wt%) solders that were fabricated with three different schemes of metallization as illustrated in Fig. 4.1. The first type had a Cu-Sn-Cu structure with copper forming both the UBM and the TSV tip. The Cu UBM was 30 µm in diameter and 6 µm thick, while the TSV was 25 µm in diameter. The second had an asymmetric Cu-Sn-Ni structure, where the UBM structure was the same as type I, and an ENIG (electroless nickel immersion gold) layer with 1.5 µm thick Ni was formed on the TSV tip. The third featured an electroplated Cu (4 µm) and Ni (2 µm) layer on the UBM side and an ENIG layer on the TSV tip, and hence was denoted Ni-Sn-Ni here. The joints were assembled using thermal compression bonding (TCB).

4.2.2 EM Test and Joule Heating

The TSV microbump joints were tested under nitrogen ambient at 180°C and 0.5A, corresponding to $7.07 \times 10^4 \mathrm{A/cm^2}$ based on the UBM opening area. The temperature of the test structures was calibrated using a built-in temperature sensor. As a result, the oven temperature was set at 152°C with an average Joule heating of 28°C. The resistance of the test structures was monitored by a four-point measurement to track the resistance change,

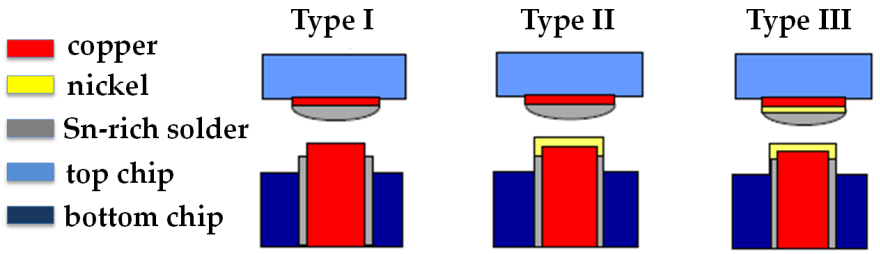

	Cu-Sn-Cu	Cu-Sn-Ni	Ni-Sn-Ni
Top die UBM	Cu	Cu	Cu + Ni
TSV tip finish	Cu	Ni + Au (ENIG)	Ni + Au (ENIG)

Figure 4.1: Schematics of bump metallization for three test vehicles.

and hence the damage evolution inside the TSV microbump joints. Figure 4.2 shows the EM test setup. The samples were mounted and wire-bonded on ceramic dual in-line packages (DIP), which were inserted into zero-insertion force (ZIF) sockets. Eight wires were connected to each sample, four for voltage and current sensing for the temperature sensor, and the other four for the device under test (DUT).

4.2.3 Microstructure Analysis

After the EM tests, current-stressed microbumps were cross-sectioned and examined using scanning electron microscope (SEM), energy dispersed x-ray (EDX), and focused ion beam (FIB), for materials characterization. The neighboring bumps subject only to thermal annealing, along with as-received bumps, were also cross-sectioned to investigate intermetallic growth, interfacial reaction, and void formation. In this way, the IMC growth kinet-

Figure 4.2: EM test setup. The inset illustrates the connection between the sample and the DIP using wiring bonding.

ics for three types of metallization under EM were obtained, and compared with those subject to thermal aging only. Results from these analyses were used to evaluate the EM reliability of the microbump joints.

4.3 Experimental Results

4.3.1 Estimation of the Annealing Temperature

The oven temperature was 152°C, whereas the DUT temperature was 180°C because of Joule heating. Due to the thermal gradient between the DUT and the ambient environment, the temperature of the neighboring bumps subject to annealing only cannot be readily obtained. A coupled electro-thermal finite element analysis (FEA) was used to estimate the temperature in the neighboring bumps. Table 4.1 lists the material properties used in the FEA. The temperature contours of an 8×8 array of TSV microbump joints are shown in Figure 4.3. While the current-stressed microbumps were tested at 180°C, the surrounding bumps were estimated to be annealed at 170°C. The difference in temperature was taken into account when we considered the kinetics of the IMC growth in microbumps with and without current.

4.3.2 Interfacial Reactions under Thermal Annealing

Interfacial reaction is important in controlling the joint reliability. The morphology and evolution of the IMC in microbump joints were first investigated at different stages of annealing. The backscattered scanning

Table 4.1: Material properties used in the FEA simulation.

Material	Electrical resistivity (Ohm·m)	Thermal conductivity (W/m/k)	Density (g/cm^3)	Specific heat (J/kg/K)
Chip (Si)	-	148	2.33	705
TSV (Cu)	2.18×10^{-8}	401	8.96	385
Microbump (Cu_6Sn_5)	17.5×10^{-8}	34.1	8.28	286
Trace (Al)	2.62×10^{-8}	237	2.7	902
Package	-	13.6	3.9	850
Die attach	-	7.92	2.5	1100
Passivation (polyimide)	-	0.12	1.39	1006
Underfill	-	0.4	1.2	1050

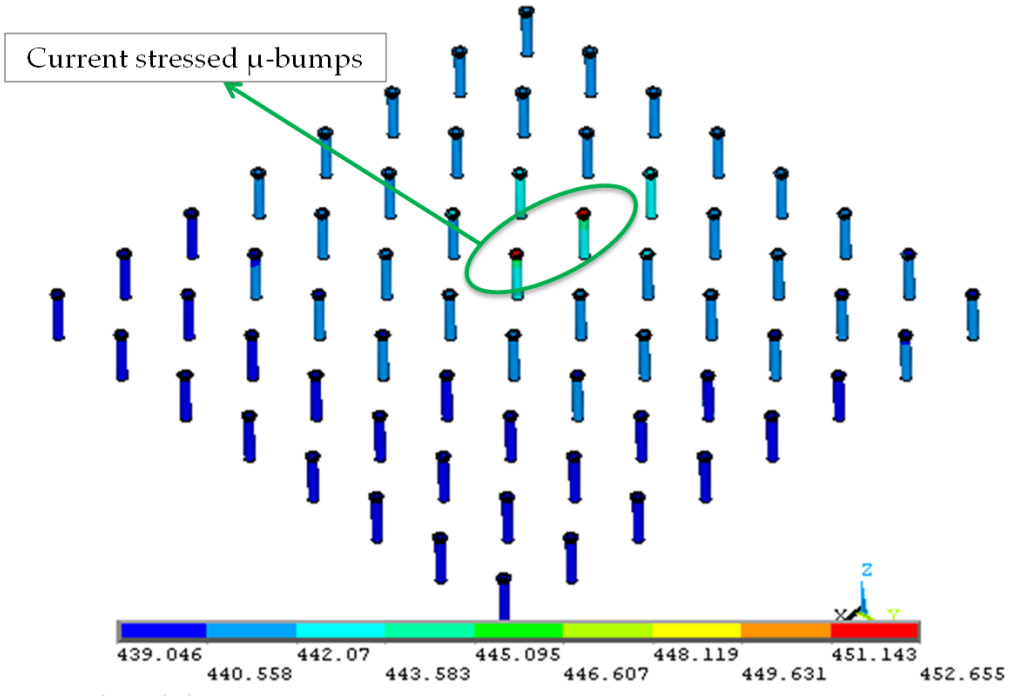

Figure 4.3: Temperature contour of an 8×8 array of TSV microbump joints calculated from finite element simulation.

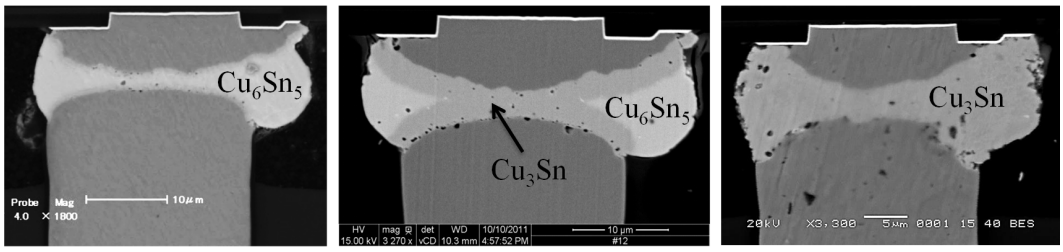

Figure 4.4: BS-SEM images of cross-sections of the Cu-Sn-Cu (type I) TSV microbump joints at different stages of thermal aging at 170°C, (a) as-received, (b) at time 83 a.u., and (c) at time 1000 a.u.

electron microscopy (BS-SEM) was used and results for the Cu-Sn-Cu (type I) structure are shown in Fig. 4.4. In the as-received microbump, the IMC conversion was already completed in the form of Cu_6Sn_5 after assembly as shown in Fig. 4.4(a). Very thin layers of Cu_3Sn existed on both sides between Cu and the Cu_6Sn_5, which were not readily observed in the back-scattering (BS) SEM image. Upon annealing, the microbumps underwent a phase transformation from Sn-rich Cu_6Sn_5 intermetallic to Cu-rich Cu_3Sn intermetallic as shown in Fig. 4.4(b). Eventually, the interfacial reaction resulted in a fully converted Cu_3Sn bump as shown in Fig. 4.4(c).

For the Cu-Sn-Cu (type I) structure, voids were observed in both annealed and current-stressed microbumps. Typical void locations were found to be in the Cu_3Sn IMC layers near the Cu/Cu_3Sn interface. While voids nucleated initially at the top UBM and the bottom TSV interfaces which can be attributed to Kirkendall voids induced by formation of Cu_3Sn, the subsequent void growth at the bottom interface might be attributed to

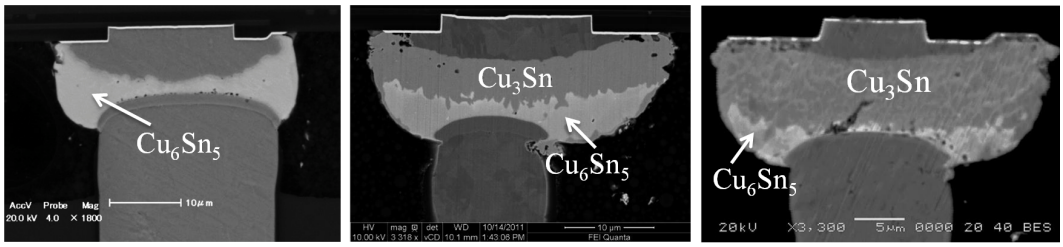

(a) (b) (c)

Figure 4.5: BS-SEM images of cross-sections of the Cu-Sn-Ni (type II) TSV microbump joints at different stages of thermal aging at 170°C, (a) as-received, (b) at time 267 a.u., and (c) at time 1000 a.u.

the difference between plating processes of the microbumps and the TSVs. Borgeson *et al.* [110] have recently observed similar voiding, and they attributed the cause for voiding to organic impurities incorporated in the Cu during electroplating.

BS-SEM results of the thermal annealed Cu-Sn-Ni (type II) structure are shown in Fig. 4.5. Fig. 4.5(a) shows a TSV microbump joint after the assembly. EDX analysis indicated that the initial reflow and thermal compression bonding has consumed all the Sn material, so that the bump was composed of IMC in the form of Cu_6Sn_5. On the UBM side, a very thin layer of Cu_3Sn was first formed, which grew thicker with aging time at the expense of Cu stud consumption. The phase transformation is shown in Figs. 4.5(b) and (c). The reaction at the TSV side was substantially reduced due to the presence of Ni that served as a barrier layer and prevented Cu in TSV from reacting with the IMC. This asymmetric IMC formation in type II bumps led to more Cu UBM consumption than type I structures.

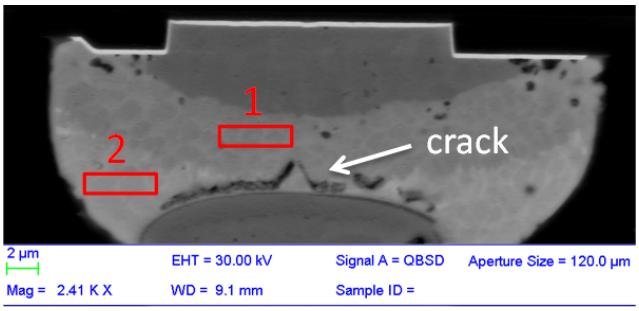

Figure 4.6: BS-SEM image of a Cu-Sn-Ni microbump, showing areas for EDX analysis summarized in Table 4.2.

Figure 4.6 and Table 4.2 shows EDX results for the two IMC phases in the Cu-Sn-Ni microbumps. As shown, only a limited amount of Ni (< 1 at. %) was dissolved to form $(Cu, Ni)_6Sn_5$ and $(Cu, Ni)_3Sn$. The amount of Ni was so small that the IMC can be regarded simply as Cu_6Sn_5 and Cu_3Sn. No $(Ni, Cu)_3Sn_4$ IMC was found. Kao *et al.* [48] studied the reaction between Ni and SnAgCu solders with varying Cu concentrations. Their results showed that at high Cu concentrations ($0.6 \sim 3.0$ at.%), $(Ni, Cu)_3Sn_4$ was not detected, but a continuous $(Cu, Ni)_6Sn_5$ layer formed. Only when the Cu concentration in the solder was low (< 0.2 at.%) that $(Ni, Cu)_3Sn_4$ was formed at the interface. In this case, however, there was ample supply of Cu from the Cu stud. Hence $(Cu, Ni)_6Sn_5$ would preferentially form with only little Ni dissolution.

A crack was found in some type II structures, as shown in Fig 4.6. The crack was suspected to be related to thermo-mechanical stress resulting from IMC formation. Since most Sn was consumed by reacting with Cu, there is an unbalanced Sn flux across the microbump. This could lead to

Table 4.2: EDX results for a Cu-Sn-Ni microbump (in at.%).

Element	Area 1	Area 2
Cu	71.61	45.69
Ni	0.74	0.72
Sn	27.65	53.59
IMC	$(Cu, Ni)_3Sn$	$(Cu, Ni)_6Sn_5$

microvoids generating near the Ni barrier layer. Table 4.3 lists key mechanical properties of Sn-3.5Ag solder and three intermetallics [70]. The IMCs have a much higher value of Youngs modulus and hardness than the solder material, indicating a potential for brittle behavior. The volume shrinkage during IMC formation can induce tensile stress within the microbump [14]. Once a crack is initiated at a locally stressed area, it can propagate fast due to the lack of plasticity. The crack might also be caused by the mismatch in coefficient of thermal expansion (CTE). Further study is required to understand this phenomenon.

Figure 4.7 shows the IMC evolution scheme of the Ni-Sn-Ni (type III) structure. After assembly, Ni_3Sn_4 growing from the opposite interfaces bridged the gap in the center, while the remaining solder material was squeezed to the side of the microbump. This is shown in Fig. 4.7(a). Sn was gradually transformed during thermal annealing, and the top and bottom Ni_3Sn_4 layers further impinged on each other, until eventually the joint was fully converted into a Ni_3Sn_4 IMC bump as shown in Fig. 4.7(c). The mor-

Table 4.3: Mechanical properties of Sn-3.5Ag solder and three intermetallics investigated in this study [70].

Properties	Sn-3.5Ag	Cu_6Sn_5	Cu_3Sn	Ni_3Sn_4
Young's modulus (GPa)	52.73	85.56	108.3	133.3
Poisson's ratio	0.36	0.309	0.299	0.330
Hardness (Vickers)	14.8 (Brinell)	378	343	365
Coefficient of thermal expansion (ppm/°C)	22.2	16.3	19.0	13.7

phology of Ni_3Sn_4 was not as planar as Cu_3Sn, but the surface gradually flattened out under thermal aging (Fig. 4.7(b)). Microvoids were observed in the type III structure. Figure 4.8 shows an example of such voiding phenomena. Since microvoids were found in some as-received bumps and after initial stage of thermal annealing, it is believed that the voids were nucleated at the Sn/Ni_3Sn_4 interface during assembly. Further impingement of the IMC layers from top and bottom interfaces may also be a reason for voiding because voids were commonly observed in the center.

4.3.3 Kinetics of Intermetallic Growth under Electromigration

So far the results on IMC formation and growth in each bumping metallization are observed under thermal annealing. In this section, the effect of EM on IMC formation is studied. Neighboring bumps subject to thermal annealing only in the same EM-tested packages were cross-sectioned

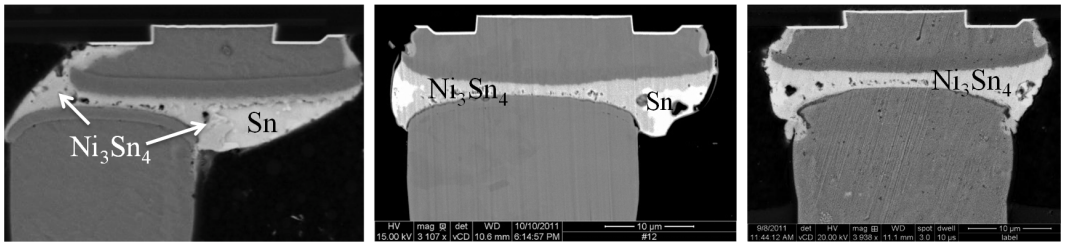

Figure 4.7: BS-SEM images of cross-sections of the Ni-Sn-Ni (type III) TSV microbump joints at different stages of thermal aging at 170°C, (a) as-received, (b) at time 83 a.u., and (c) at time 1000 a.u.

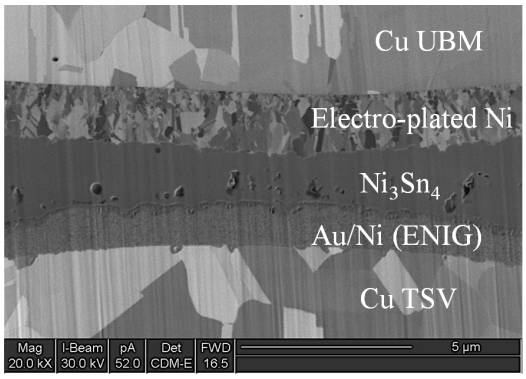

Figure 4.8: Ion beam image showing the cross-sections of a Ni-Sn-Ni microbump joint with microvoids inside Ni_3Sn_4 IMC

and examined together with the current-stressed microbumps. Figure 4.9 compares SEM results for type I (Cu-Sn-Cu) microbumps with and without current stressing. Electron flow direction is shown in the figure. The results indicated two stages of IMC formation for type I microbumps under EM testing. In the early stage, the microbumps experienced a phase transformation by consuming both the Cu UBM and the TSV. Upon complete transformation, the bump configuration would remain unchanged, either under further annealing or EM, since there was no more solder available for IMC formation. The fully converted IMC bump was stable against electric current in that no EM-induced damage was observed in the EM-tested microbumps.

Figure 4.10 presents SEM images for type II (Cu-Sn-Ni) microbumps with and without current stressing. As discussed in the previous session, cracks were observed in EM as well as under thermal aging, confirming that the stress-related cracks had already developed without EM stressing.

Figure 4.11 shows SEM results for the type III (Ni-Sn-Ni) structure subject to current stressing and thermal annealing only. As can be seen in Fig. 4.11, Sn diffused from the sidewalls and reacted with the Cu UBM as well as the TSV, which is not desirable. This could be prevented by promoting the barrier layer formation during TSV fabrication and bumping process.

Based on these results, IMC thickness for each test structure under EM and thermal annealing was determined from the SEM images, and ki-

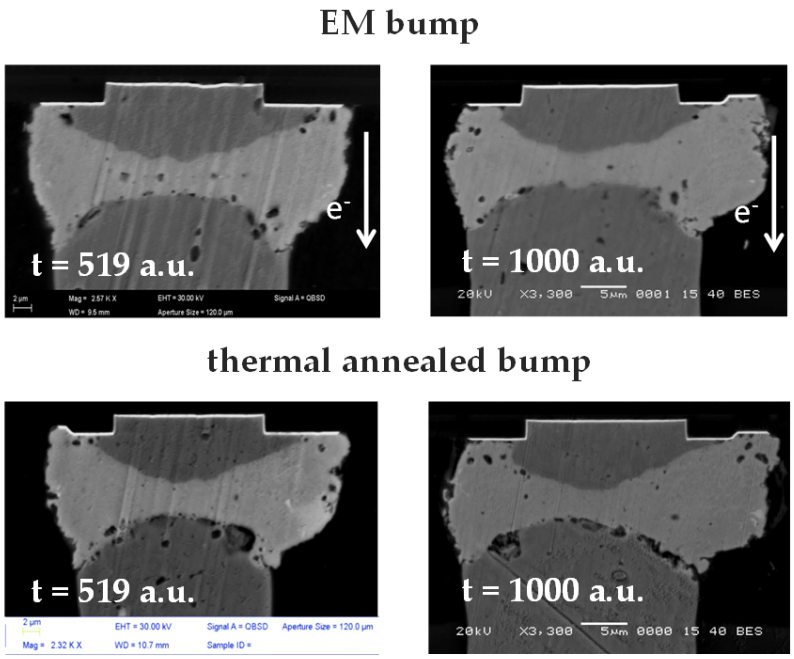

Figure 4.9: EM (180°C) vs. thermal annealing (170°C) for type I structure.

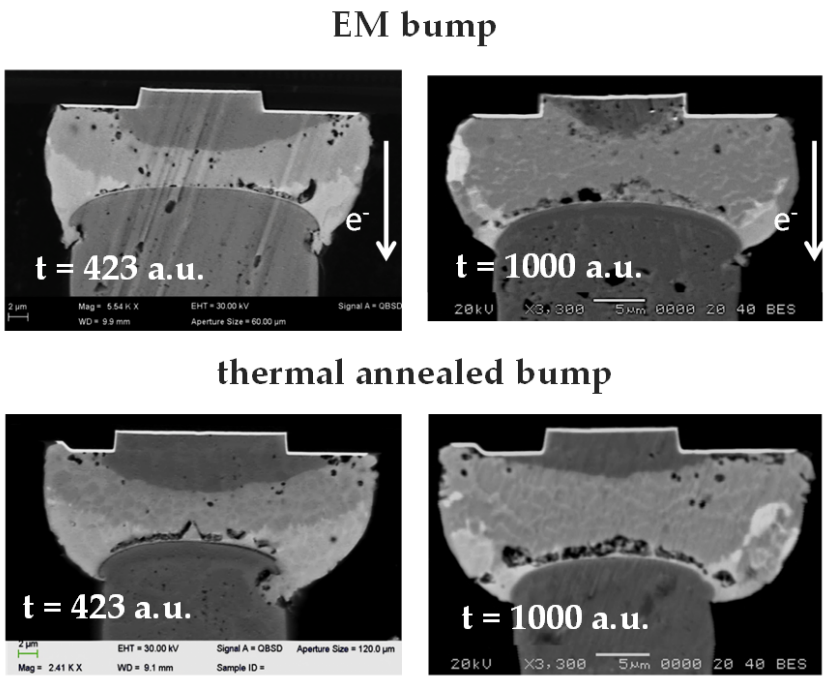

Figure 4.10: EM (180°C) vs. thermal annealing (170°C) for type II structure.

netic growth rates were obtained as shown in Fig. 4.12 and Table 4.4. The IMC thickness was found to increase with the square root of time for all test structures. Thus the IMC growth followed a parabolic time dependence, indicating a diffusion-controlled process. The amount of Cu_3Sn would no longer grow after the Cu concentration reached saturation in Sn. This is reflected in the flat step as shown in Fig. 4.12(a). By comparing the growth rates in type I and II structures, it can be found that the growth rate of Cu-Sn-Cu structures was less than two times that of Cu-Sn-Ni structure, although interfacial reaction was double-sided in type I and single-sided in type II. This can be attributed to the interaction between the two interfaces across the microbump. Since the physical spacing between the upper and lower metallization is small, it takes only a shorter time for the two interfaces to touch each other. The interaction between the two interfaces should be taken into account when estimating the IMC growth in the microbumps with limited supply of Sn. The type III microbump had the largest EM-enhanced effect in comparison with the annealed bumps (Fig. 4.12(c)). However, the overall IMC growth characteristics were not significantly affected by EM. This observation in microbumps is different from that in flip chip solder joints, where IMC growth can be greatly enhanced under EM. Chao *et al.* [18] reported that IMC growth under EM followed a linear relationship with time, in contrast to a parabolic growth commonly observed under solid-state annealing. It has been shown in Chapter 2 that the EM-enhanced IMC growth is closely related to the fast diffusion rates of Cu and Ni in sol-

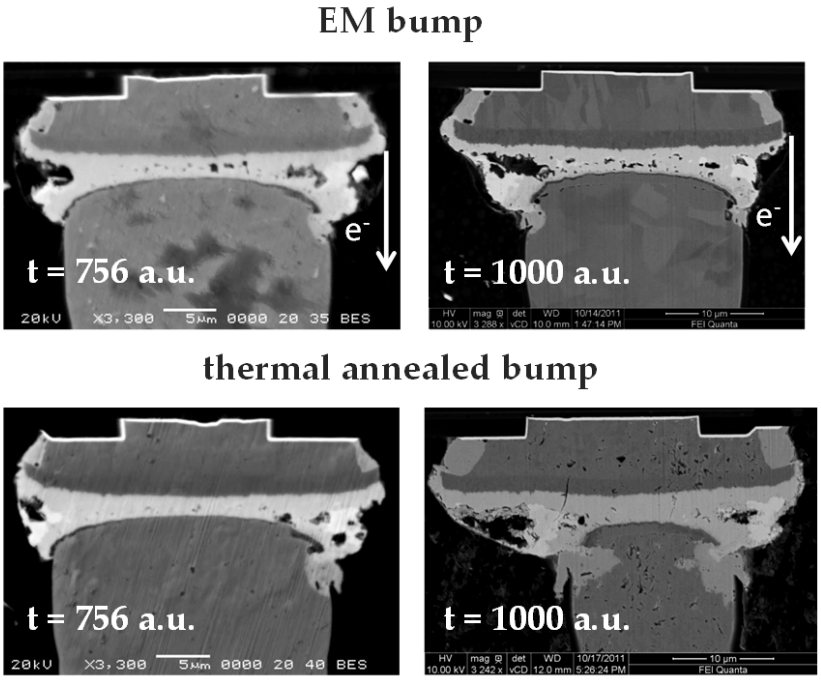

Figure 4.11: EM (180°C) vs. thermal annealing (170°C) for type III structure.

der. For the case of microbumps, especially type I and II, solder was fully reacted upon bonding, making the joints consisting of IMC bumps. Since the diffusion rate in the IMCs are several orders of magnitude slower than in solder, the EM driving force is expected to be small, and thus the EM enhancement effect on IMC growth kinetics is not significant once the IMC conversion is completed. In addition, it is clearly shown from Table 4.4 that Ni is an effective barrier layer in slowing down the IMC growth.

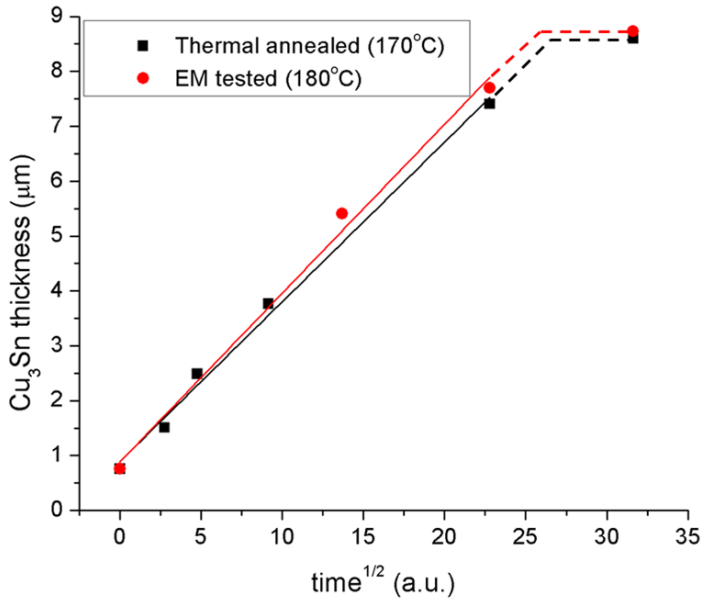

(a)

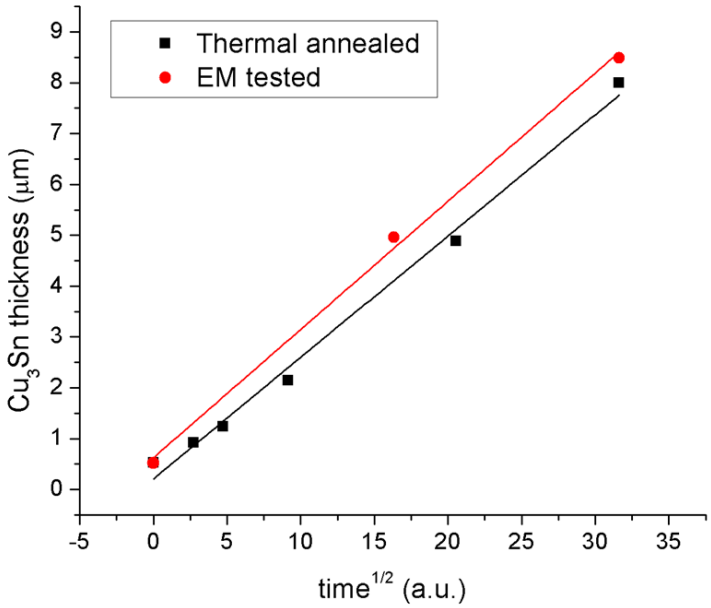

(b)

Figure 4.12: IMC thickness as a function of square root of time for three types of structures under EM and thermal annealing, (a) type I (Cu-Sn-Cu); (b) type II (Cu-Sn-Ni).

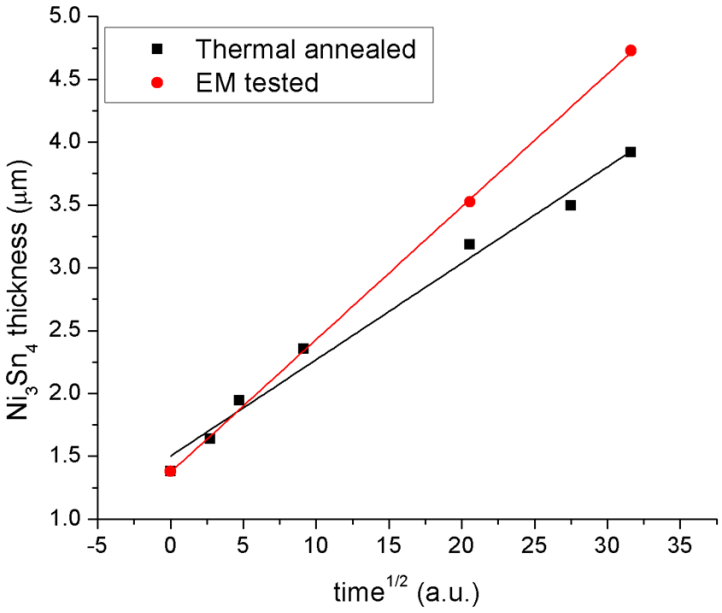

(c)

Figure 4.12: (Continued) IMC thickness as a function of square root of time for three types of structures under EM and thermal annealing, (c) type III (Ni-Sn-Ni).

Table 4.4: Calculated IMC growth rate constant (k) and linear correlation coefficients (R^2) for TSV microbump joints under EM and thermal annealing, assuming a parabolic growth law $y = k\sqrt{t} + y_0$, where y is the IMC thickness, t is time, and y_0 is the initial IMC thickness.

	$k(\mu m/h^{1/2})$		R^2	
Structure	EM tested $180^\circ C$	Annealed $170^\circ C$	EM tested $180^\circ C$	Annealed $170^\circ C$
Cu-Sn-Cu	0.28	0.27	0.9880	0.9925
Cu-Sn-Ni	0.23	0.22	0.9978	0.9933
Ni-Sn-Ni	0.096	0.070	0.9999	0.9872

4.3.4 EM Test Results

EM test results are summarized in Fig. 4.13, where the resistance traces monitored during EM testing are plotted. For the survived units, their resistance traces remained flat until test was terminated. For the failed units, two failure modes were observed as shown by the resistance traces. For most of the failed samples, the resistance had an abrupt jump at the time of failure. No significant resistance increases were observed before the sudden jump, indicating no cumulative damage induced by EM within the microbump. Such failures were confirmed to be false failures, not related to electromigration in the TSV microbump joints. This is consistent with the cross-sectional results showing no additional damage due to EM. Even though non-EM induced voids developed in the microbumps, they may not be sufficient to cause the microbumps to fail and result in the sudden resistance increase. On the other hand, two samples in the Cu-Sn-Ni structure exhibited a gradual resistance increase up to $\Delta R \sim 100\%$, as highlighted in Fig. 4.13(b). One of the failed units was cross-sectioned and the BS-SEM image was inserted in Fig. 4.13(b), which shows crack formation by interconnecting series of voids in the EM-stressed microbump at the bottom interface. This failure mode was believed to be related to crack propagation discussed in the previous section and not related to electromigration. It is therefore concluded that no EM-related failures were detected during the EM testing period.

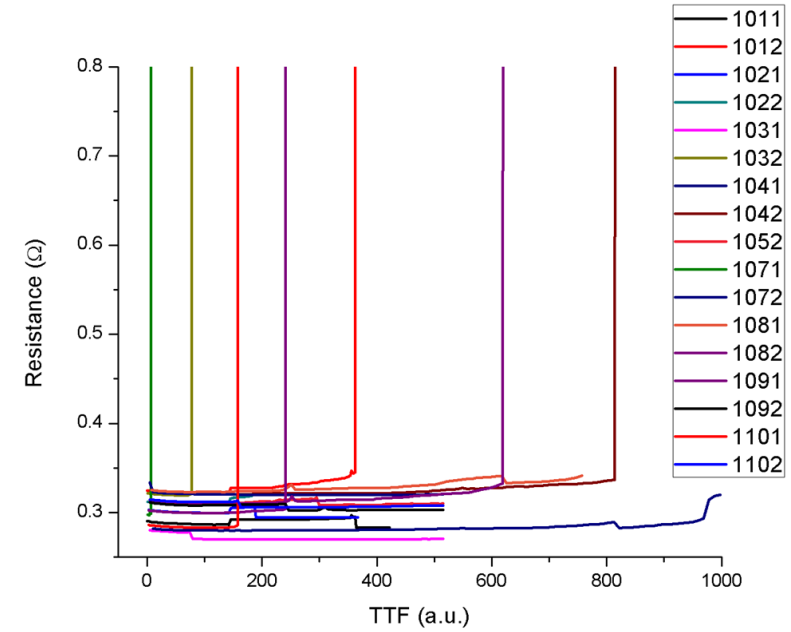

(a)

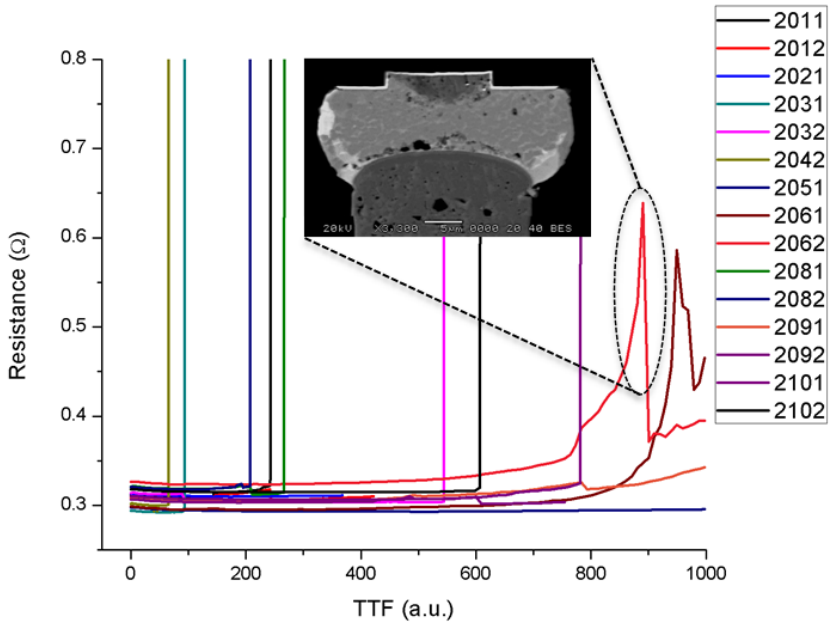

(b)

Figure 4.13: Resistance change monitored by four-point measurement during EM testing for (a) type I (Cu-Sn-Cn), (b) type II (Cu-Sn-Ni).

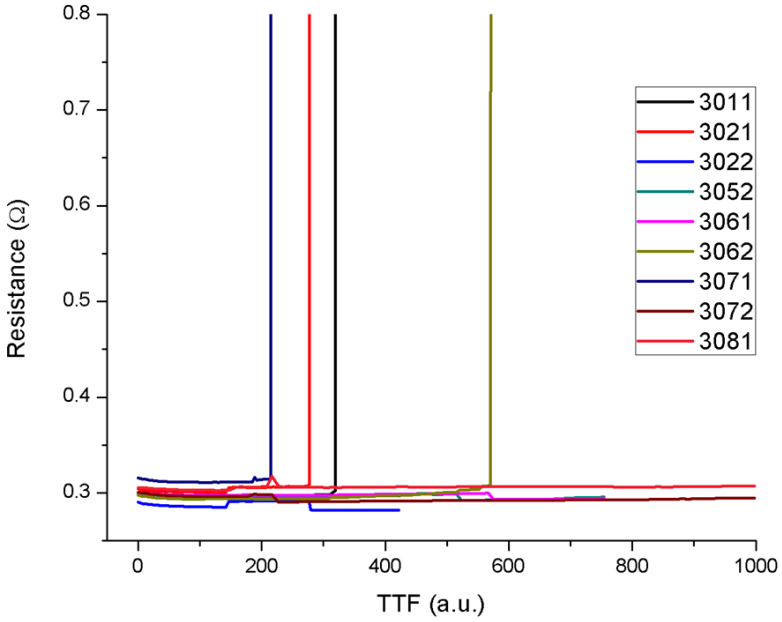

(c)

Figure 4.13: (Continued) Resistance change monitored by four-point measurement during EM testing for (c) type III (Ni-Sn-Ni).

4.4 Discussion

4.4.1 Other Reliability Concerns for 3D IC Microbumps

In the present study, the EM reliability of the TSV microbump joints was investigated and found to be much better than flip chip C4 solder joints. This is because of the limited amount of solder that can be fully converted into IMC after bonding or shortly thereafter due to the high testing temperature. Other reliability concerns, however, have been reported in microbumps involving low-volume solders. Dunne *et al.* [33] studied the thermal cycling reliability of the microbumps using the same test structures as those in this work. No failure was observed in the type III, i.e., Ni-Sn-Ni system. But a few failures occurred in type I and II systems as shown in Fig. 4.14. This is likely because the unconsumed Sn in the type III system makes the joint more ductile and more favorable for thermal cycling fatigue. Sakuma *et al.* [91] also investigated the thermal cycling reliability of stacking die structures with Cu/Sn and Cu/Ni/In microbumps. Their results showed that the stacked systems with Cu/Ni/In joints had fewer failures than Cu/Sn joints for the reason that some In remained in the Cu/Ni/In joints, which served as a stress relieve layer. For the Cu/Sn microbumps, cracking in Si was observed indicating that stresses were transferred to the weaker location inside the chip. Cheng *et al.* [21] reported early failure in Cu/Ni/Sn-2.5Ag microbumps under thermal cycling. The authors attributed the failure to defects induced during phase transformation. Son *et al.* [96] reported failure at the metal pad of the microbumps after ther-

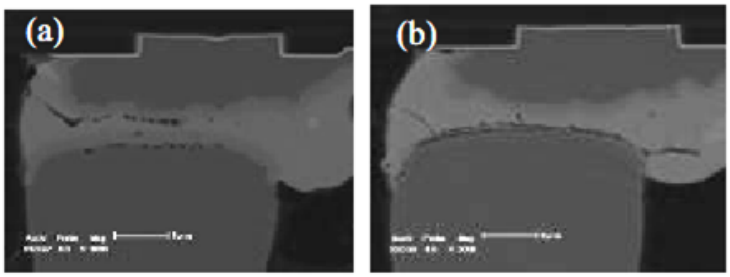

Figure 4.14: Joint cracks after thermal cycling in (a) Cu-Sn-Cu, and (b) Cu-Sn-Ni [33].

mal cycling test. These results indicate that microbumps with low-volume solder may decrease the thermal fatigue effects because there is less solder left for plastic deformation. Instead, the stress in the intermetallics due to phase transformation or thermal cycling can be large enough to cause failure. In this case, depending on the structure of the package as well as the microbumps, failure may occur at the weakest location other than in the IMC.

4.4.2 Processing and Design Optimization for 3D IC Microbumps

Bump design requires a careful optimization. The amount of Sn should be optimized so that a certain amount would remain after the initial reflow. This is because unconsumed Sn is beneficial to the temperature cycling reliability [33, 91] while consumed Sn into IMC can improve EM reliability. The thickness of UBM is also critical because excessive consumption would lead to joint opens. An optimal UBM thickness depends on the specific UBM/solder system. Among the three bump configurations investi-

gated in this study, asymmetric joint design Cu-Sn-Ni requires a thick UBM due to excess material consumption on the Cu UBM side. The problem is alleviated in the Cu-Sn-Cu structure. But non-uniform UBM consumption rate has been observed because the solder would easily wet on sidewalls of the UBM. Using Ni as metallization on both interfaces gives the bump a better protection against sidewall wetting. However, in order to prevent Cu TSV from reacting with the solder, the ENIG plating on the TSV tip needs to seal perfectly all the way to the sides of TSV.

4.5 Summary

EM reliability of TSV microbump joints in 3D interconnects has been investigated. No EM-related damage was identified in the three types of TSV microbump joints investigated after 1200 hours of EM testing. This was mainly because the microbumps had been fully converted into IMC bumps after assembly or under thermal annealing. The EM performance of IMC bumps was better than Sn-based C4 solder joints [107]. Furthermore, EM did not significantly enhance IMC growth in three types of structures studied here.

It is suggested that the UBM and bump configuration be carefully designed in order to improve the overall reliability of the microbumps. Symmetric joint design like Cu-Sn-Cu and Ni-Sn-Ni are preferred because of symmetric IMC formation and metallization consumption.

Although the microbumps are superior in EM reliability, other reliability issues remain, such as process-induced defects, excessive UBM consumption, and void/crack formation. While the first two can be improved by process or design optimization, the last problem indicates that stresses exist in the microbumps, and either void or crack forms to partially relieve the stress. Origins of stress could be thermal stress induced during thermal cycling, or related to interfacial reactions when there is unbalanced diffusion rates and phase transformation-induced volume shrinkage [14]. More research is therefore required to improve the mechanical integrity of the microbumps. This will be addressed in the next chapter.

Chapter 5

Concurrent Interdiffusion, Phase Transformation and Deformation

A theory is the more impressive the greater the simplicity of its premises, the more different kinds of things it relates, and the more extended its area of applicability.

Albert Einstein

5.1 Introduction

Stress generation in alloys due to interdiffusion is a long-standing problem in materials science. Kirkendall voiding is one of the examples. Other stress relaxation mechanisms include [8] creep, disloction slide, bending, and brittle fracture. The effect of the diffusion-induced stress also depends on their time scale as compared to the annealing time.

It would be useful to make a distinction between three different types of diffusion-induced stresses: (i) from concentration (due to inequality of the atomic volumes); (ii) from diffusion (due to unbalanced intrinsic diffusion rates of two different diffusing species); and (iii) from stresses related to the formation of a new phase if the density of the product phase is different

from that of the parent phase.

In the last chapter, it has been pointed out that stress management would be important in improving the reliability of 3D IC microbumps. In order to study the diffusion-induced stress evolution, stress analysis needs to be coupled into the kinetic model of interdiffusion. The subject of coupling mechanics and material reaction systems has been explored in many areas of research. Suo *et al.* [98] formulated a theory to model oxidation, diffusion and creep to study stress generation and voiding in alloys upon selective oxidation. Pharr *et al.* [88] developed a model that couples EM and creep to investigate EM in Pb-free solder joints. Zhao *et al.* [117] formulated an analysis of concurrent reaction and plasticity to study initial lithiation of crystalline silicon in lithium-ion batteries. The main idea behind these analyses can also be applied to the IMC materials where concomitant interdiffusion, phase transformation, and deformation occur. This chapter presents a modeling study that couples stress to the kinetic analysis of IMC formation in the solder-UBM alloying systems.

5.2 Model Description

A one dimensional coupled analysis was formulated as illustrated in Fig. 5.1. Consider a diffusion couple comprising of two semi-infinite metals annealed at an elevated temperature, where an IMC layer forms in between. The two phase boundaries, S_1 and S_2 move as the IMC grows thicker, and therefore it's a moving boundary problem. Here the concentration-induced

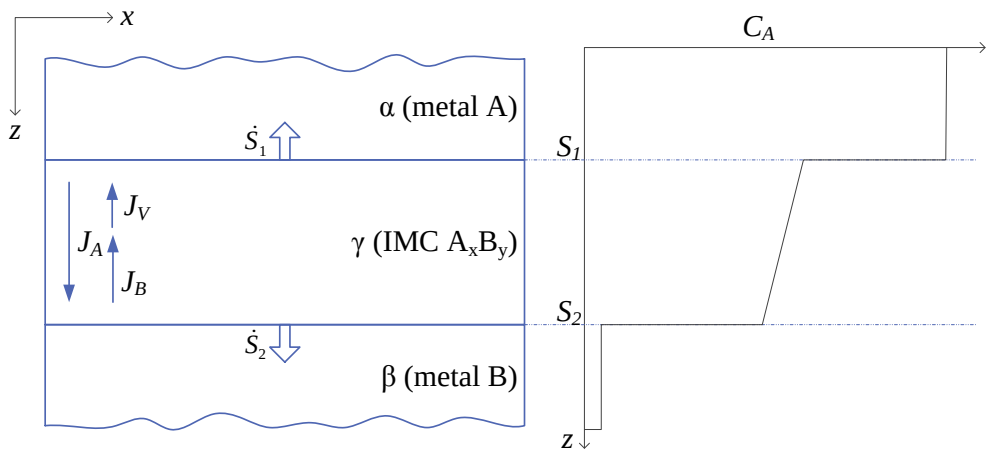

Figure 5.1: Schematic of the model.

stress is ignored in the analysis because intermetallics have a very narrow concentration range. The stresses generated from interdiffusion and phase transformation are both considered. Within the IMC phase, the two elements, A and B, diffuse in opposite directions at different rates. This inequality can generate contraction on one side while expansion on the other. Meanwhile, phase transformation induces stress as well, the amount of which depends on the volumetric difference between the two phases. The stress accommodation is assumed to be mostly elastic, but plasticity is allowed near the phase boundary, which will be discussed later.

5.2.1 Concentration Evolution

The atomic fluxes due to concentration gradient and diffusion-induced stress are expressed as,

$$J_A = -D_A \frac{\partial C_A}{\partial z} + \frac{\Omega C_A D_A}{kT} \frac{\partial \sigma^m}{\partial z} \tag{5.1}$$

$$J_B = -D_B \frac{\partial C_B}{\partial z} + \frac{\Omega C_B D_B}{kT} \frac{\partial \sigma^m}{\partial z} \tag{5.2}$$

where J is the diffusion flux, D is the intrinsic diffusion coefficient, C is the number of atoms per unit volume, Ω is the atomic volume, k is the Boltzmann constant, T is the absolute temperature in Kelvin, σ^m is the mean stress defined as one third of the sum of the principal stresses, z is the thickness, and A and B are the two diffusing species.

It is assumed that the vacancy concentration is low so that the atomic concentrations satisfy

$$(C_A + C_B)\Omega = 1 \tag{5.3}$$

Therefore Eq. (5.2) can be rewritten as,

$$J_B = D_B \frac{\partial C_A}{\partial z} + \frac{\Omega C_B D_B}{kT} \frac{\partial \sigma^m}{\partial z} \tag{5.4}$$

J_A and J_B are the atomic fluxes with respect to the lattice plane. Non-reciprocal diffusion of the two species gives rise to the inequality of these two fluxes,

$$J_A \neq J_B \tag{5.5}$$

In substitutional alloys, atoms diffuse by jumping into an adjacent vacant site in the lattice. In other words, the vacancy can be viewed as a

third diffusion species that can jump into a site occupied by an atom. The diffusion fluxes are balanced by introducing an additional vacancy flux, denoted by J_V.

$$J_A + J_B + J_V = 0 \tag{5.6}$$

The vacancy flux is obtained by substituting Eq. (5.1) and (5.4) into Eq. (5.6):

$$\begin{aligned} J_V &= -(J_A + J_B) \\ &= D_A \frac{\partial C_A}{\partial z} - D_B \frac{\partial C_A}{\partial z} - \frac{\Omega C_A D_A}{kT} \frac{\partial \sigma^m}{\partial z} - \frac{\Omega C_B D_B}{kT} \frac{\partial \sigma^m}{\partial z} \\ &= (D_A - D_B) \frac{\partial C_A}{\partial z} - \frac{\Omega}{kT} (C_A D_A + C_B D_B) \frac{\partial \sigma^m}{\partial z} \end{aligned} \tag{5.7}$$

For substitutional binary materials where atoms migrate based on a vacancy diffusion mechanism, the vacancies are created or removed by removing or adding an atomic plane. This causes the atomic plane to move with respect to the laboratory reference. The velocity, v, at which the atomic planes move is controlled by the vacancy flux,

$$v = \Omega J_V = \Omega (D_A - D_B) \frac{\partial C_A}{\partial z} - \frac{\Omega^2}{kT} (C_A D_A + C_B D_B) \frac{\partial \sigma^m}{\partial z} \tag{5.8}$$

The net flux of A, N_A, consists of a diffusion flux as described by Eq. (5.1), and a vacancy flux due to the moving lattice plane, vC_A. Then

$$\begin{aligned} N_A &= J_A + vC_A \\ &= -D_A \frac{\partial C_A}{\partial z} + \frac{\Omega C_A D_A}{kT} \frac{\partial \sigma^m}{\partial z} \\ &\quad + \Omega C_A (D_A - D_B) \frac{\partial C_A}{\partial z} - \frac{\Omega^2 C_A}{kT} (C_A D_A + C_B D_B) \frac{\partial \sigma^m}{\partial z} \\ &= -\widetilde{D} \frac{\partial C_A}{\partial z} + \frac{D_A - D_B}{kT} \Omega C_A (1 - \Omega C_A) \frac{\partial \sigma^m}{\partial z} \end{aligned} \tag{5.9}$$

$$\widetilde{D} = (1 - X_A)D_A + X_A D_B \tag{5.10}$$

where $\widetilde{D}$ is the interdiffusion coefficient, and X_A is the atomic fraction of element A. From Eq. (5.9), it can be seen that the stress-induced diffusion depends on the stress gradient as well as the difference between the two diffusion coefficients.

The net flux of B can be derived similar to Eq. (5.9):

$$\begin{aligned} N_B &= J_B + vC_B \\ &= \widetilde{D}\frac{\partial C_A}{\partial z} - \frac{D_A - D_B}{kT}\Omega C_A(1 - \Omega C_A)\frac{\partial \sigma^m}{\partial z} \\ &= -N_A \end{aligned} \tag{5.11}$$

Eq. (5.11) implies that the sum of the two net fluxes vanishes:

$$N_A + N_B = 0 \tag{5.12}$$

Now the concentration evolution of A can be obtained by applying the Fick's second law of diffusion:

$$\begin{aligned} \frac{\partial C_A}{\partial t} &= -\frac{\partial N_A}{\partial z} \\ &= \frac{\partial}{\partial z}\left[\widetilde{D}\frac{\partial C_A}{\partial z} - \frac{D_A - D_B}{kT}\Omega C_A(1 - \Omega C_A)\frac{\partial \sigma^m}{\partial z}\right] \end{aligned} \tag{5.13}$$

The derivation above is similar to Darken's analysis, except that a stress-induced term is added to the diffusion flux. The key is to recognize that non-reciprocal diffusion of the two elements resulted in unequal diffusion fluxes, and they are compensated by a vacancy diffusion flux.

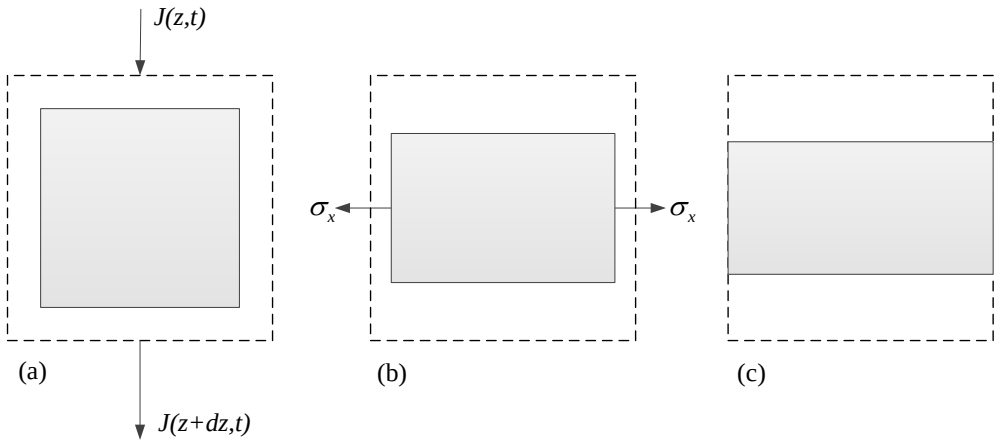

Figure 5.2: (a) Unequal diffusion rates of two components result in a net mass gain or loss. (b) The biaxial stress field causes deformation. (c) Diffusion and deformation combined to meet the constraint in the transverse directions.

5.2.2 Stress Evolution

The stress generated due to unbalanced diffusion rates of two diffusion species can be illustrated as shown in Fig. 5.2. A non-reciprocal diffusion results in a net mass gain or loss, which generates a strain field (Fig. 5.2(a)). The material is constrained in the lateral directions, so the film is stress free in the z direction, but subjected to a biaxial stress field which induces deformation (Fig. 5.2(b)). The diffusion and deformation combine to satisfy the constraint in the lateral direction (Fig. 5.2(c)). In the present study, only elastic deformation is considered.

The total strain, ϵ_{ij}, is the sum of that due to diffusion, ϵ_{ij}^{D}, and that

due to elastic deformation, ϵ_{ij}^E. So is the total strain rate.

$$\epsilon_{ij} = \epsilon_{ij}^D + \epsilon_{ij}^E \tag{5.14}$$

$$\frac{\partial \epsilon_{ij}}{\partial t} = \frac{\partial \epsilon_{ij}^D}{\partial t} + \frac{\partial \epsilon_{ij}^E}{\partial t} \tag{5.15}$$

The divergence of the diffusion flux induces isotropic strain rates [98],

$$\frac{\partial \epsilon_{ij}^D}{\partial t} = \frac{\Omega}{3} \frac{\partial J_V}{\partial z} \delta_{ij} \tag{5.16}$$

The elastic deformation can be described by Hooke's law. Under a biaxial stress state,

$$\sigma_x = \sigma_y = \sigma \tag{5.17}$$

$$\sigma_z = 0 \tag{5.18}$$

$$\epsilon_x^E = \epsilon_y^E = \frac{1-\nu}{E} \sigma \tag{5.19}$$

where E is the Young's modulus, and ν is the Poisson's ratio. In the biaxial stress field, the mean stress is

$$\sigma^m = \frac{2}{3} \sigma \tag{5.20}$$

Since the sandwiched structure is assumed to be confined by the surrounding rigid materials, the total strain as well as the total strain rate in the two transverse directions, x and y, are zero:

$$\epsilon_x = \epsilon_y = 0 \tag{5.21}$$

$$\frac{\partial \epsilon_x}{\partial t} = \frac{\partial \epsilon_y}{\partial t} = 0 \tag{5.22}$$

Combining Eq. (5.15) and (5.22) gives rise to

$$\frac{\partial \epsilon_x^E}{\partial t} = -\frac{\partial \epsilon_x^D}{\partial t} \tag{5.23}$$

Applying Eq. (5.19) and (5.16) into (5.23), the stress evolution is deduced

$$\frac{\partial \sigma}{\partial t} = -\frac{E\Omega}{3(1-\nu)}\frac{\partial J_V}{\partial z} \tag{5.24}$$

J_V was derived in Section 5.2.1. Applying Eq. (5.7) into Eq. (5.24) and substitute σ^m by σ, the stress evolution becomes:

$$\frac{\partial \sigma}{\partial t} = \frac{E\Omega}{3(1-\nu)}\frac{\partial}{\partial z}\left[-\Delta D\frac{\partial C_A}{\partial z} + \frac{2}{3}\frac{\overline{D}}{kT}\frac{\partial \sigma}{\partial z}\right] \tag{5.25}$$

where

$$\begin{aligned}\overline{D} &= \Omega C_A D_A + (1-\Omega C_A) D_B \\ &= X_A D_A + X_B D_B\end{aligned} \tag{5.26}$$

$$\Delta D = D_A - D_B \tag{5.27}$$

Similarly, substitute σ^m by σ and rewrite Eq. (5.13):

$$\frac{\partial C_A}{\partial t} = \frac{\partial}{\partial z}\left[\widetilde{D}\frac{\partial C_A}{\partial z} - \frac{2}{3}\frac{\Delta D}{kT}\Omega C_A(1-\Omega C_A)\frac{\partial \sigma}{\partial z}\right] \tag{5.28}$$

In summary, Eq. (5.25) is the governing equation for stress evolution. Together with Eq. (5.28), they formulate the kinetic model taking into account simultaneous concentration and stress evolution.

Phase transformation takes place near the interfaces in addition to interdiffusion. In order to derive the rate at which each phase grows or

shrinks, one must consider mass transport across the interface. Stress at the phase boundary also needs special treatment due to an additiontal source of stress. This will be discussed in the following section.

5.2.3 Boundary Conditions and Interface Migration

The phase boundary conditions require careful consideration because the problem involves moving interfaces together with change in density due to phase transformation.

Figure 5.3 shows the binary Ni-Sn phase diagram [92]. The solubility range in a certain phase as a function of temperature can be determined based on the phase diagram, and the upper and lower bound of the solubility are set as the atomic fraction of the component at the phase boundaries, denoted as X_A^{upper}, and X_A^{lower}, respectively.

Referring to Fig. 5.1, there are two moving interfaces, one between the α and γ phases, S_1, and the other between the γ and β phases, S_2. Using the general solution to the interface movement in Eqs. (B.4) and (B.5) in Appendix B, the interface migration equations for these two phase boundaries can be obtained. For S_1, $X_A^{\alpha\gamma} = 1$, $N_{A,\alpha} = 0$. Eq. (B.4) becomes,

$$dz^{\gamma}\Big|_{S_1} = -\frac{\Omega dt}{\left(1 - X_A^{\text{upper}}\right)} N_{A,\gamma}\Big|_{S_1} \tag{5.29}$$

For S_2, $X_A^{\beta\gamma} = 0$, $N_{A,\beta} = 0$. Eq. (B.5) becomes,

$$dz^{\gamma}\Big|_{S_2} = \frac{\Omega dt}{X_A^{\text{lower}}} N_{A,\gamma}\Big|_{S_2} \tag{5.30}$$

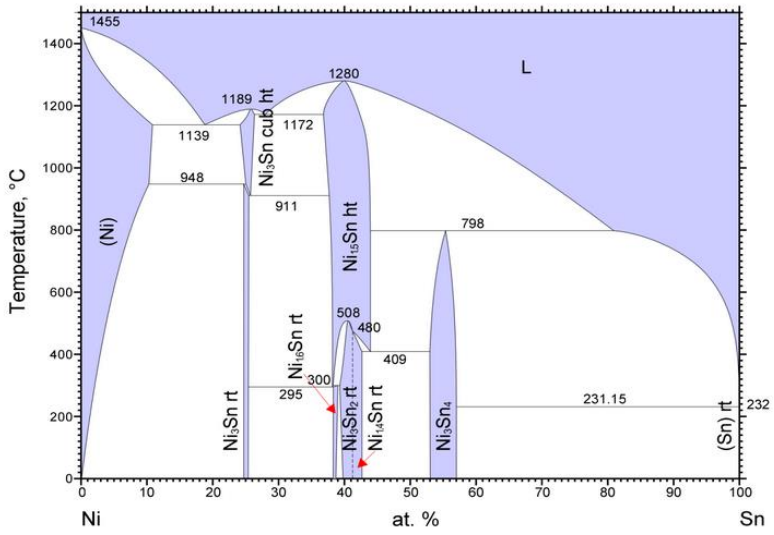

Figure 5.3: Binary Ni-Sn phase diagram

The volumetric change during phase transformation induces a dilatational strain field. The analysis is similar to the derivation for the diffusion induced stress, and the schematic diagram is illustrated in Fig. 5.4. Phase transformation-induced volumetric strain, ϵ_V, can be expressed as,

$$\epsilon_V = \frac{\Omega_{\text{IMC}} - \Omega_{\text{Metal}}}{\Omega_{\text{Metal}}} \tag{5.31}$$

The transformation-induced strain in each direction is one third of the volumetric strain,

$$\epsilon_i^T = \frac{1}{3}\epsilon_V = \frac{1}{3}\frac{\Omega_{\text{IMC}} - \Omega_{\text{Metal}}}{\Omega_{\text{Metal}}} \quad (i = x, y, z) \tag{5.32}$$

Due to the constraint of the material in the lateral directions, the phase transformation-induced strain is accommodated by deformation. For

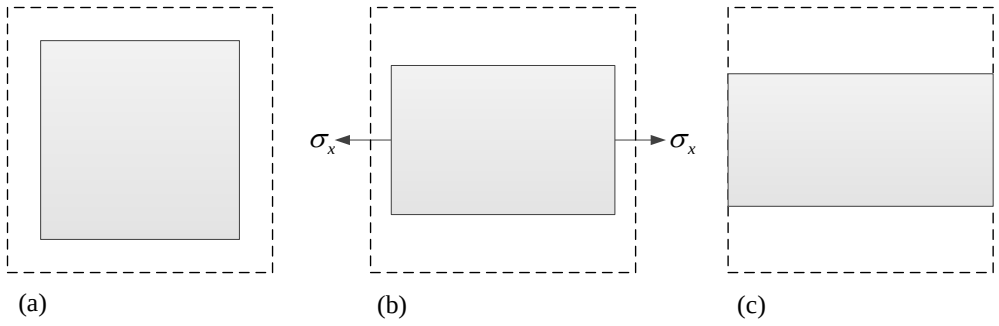

Figure 5.4: (a) Phase transformation induces volumetric change due to density mismatch between the product phase and the parent phase. (b) The biaxial stress field causes deformation. (c) Phase transformation and deformation combined to meet the confinement in the transverse directions.

the Ni-Sn alloy system under investigation, the volumetric strain exceeds the elastic regime of the material. Plasticity is therefore considered at the phase boundaries. The total strain is the sum of the phase transformation-induced strain and the plastic strain,

$$\epsilon_i = \epsilon_i^T + \epsilon_i^P \tag{5.33}$$

The net strain in the x and y directions vanish,

$$\epsilon_i^P = -\frac{1}{3}\frac{\Omega_{\text{IMC}} - \Omega_{\text{Metal}}}{\Omega_{\text{Metal}}} \quad (i = x, y, z) \tag{5.34}$$

Assuming a power law stress-strain relationship,

$$\sigma = K\epsilon^n \tag{5.35}$$

where K is the strength coefficient, and n is the work hardening exponent.

Under a uniaxial stress state,

$$\epsilon_z^P = -sign(\sigma)\left(\frac{|\sigma|}{K}\right)^{1/n} \tag{5.36}$$

Plastic deformation perserves volume, which means the sum of the strains at three directions is zero, thus,

$$\epsilon_x^P = \epsilon_y^P = \frac{sign(\sigma)}{2}\left(\frac{|\sigma|}{K}\right)^{1/n} \tag{5.37}$$

Eq. (5.35) and (5.37) give rise to the biaxial stress at the phase boundaries,

$$\sigma\Big|_{S_1} = -K\left[\frac{2(\Omega_\gamma - \Omega_\alpha)}{3\Omega_\alpha}\right]^n \mathrm{sgn}(\Omega_\gamma - \Omega_\alpha) \tag{5.38}$$

$$\sigma\Big|_{S_2} = -K\left[\frac{2(\Omega_\gamma - \Omega_\beta)}{3\Omega_\beta}\right]^n \mathrm{sgn}(\Omega_\gamma - \Omega_\beta) \tag{5.39}$$

5.2.4 Dimensionless Analysis

First set the dimensionless parameter, η, as the ratio of diffusivity of component B to that of component A:

$$\eta = \frac{D_B}{D_A} \tag{5.40}$$

Then set another dimensionless parameter, χ, as the raio of the biaxial modulus to the thermal energy per unit volume:

$$\chi = \frac{2E\Omega}{3kT(1-\nu)} \tag{5.41}$$

The concentration of component A scales with density $1/\Omega$. The biaxial stress scales with its biaxial modulus:

$$\Sigma = \frac{E}{1-\nu} \tag{5.42}$$

The coordinate z and the interface position S scale with the IMC length at a certain time, H. Then the time scales with τ set by Eq. (5.28):

$$\tau = \frac{H^2}{D_A} \tag{5.43}$$

Consequently, the diffusion Eq. (5.28) becomes:

$$\frac{\partial c}{\partial t} = \frac{\partial}{\partial z}\left[(1-c+\eta c)\frac{\partial c}{\partial z} - \chi(1-\eta)c(1-c)\frac{\partial \sigma}{\partial z}\right] \tag{5.44}$$

and the stress Eq. (5.25) becomes:

$$\frac{\partial \sigma}{\partial t} = \frac{1}{3}\frac{\partial}{\partial z}\left[-(1-\eta)\frac{\partial c}{\partial z} + \chi\left(c+(1-c)\eta\right)\frac{\partial \sigma}{\partial z}\right] \tag{5.45}$$

The scaled concentration at the boundaries are:

$$c\big|_{S_1} = X_A^{\text{upper}} \tag{5.46}$$

$$c\big|_{S_2} = X_A^{\text{lower}} \tag{5.47}$$

The boundary conditions in Eq. (5.38) and (5.39) become:

$$\sigma\Big|_{S_1} = -\frac{K}{\Sigma}\left[\frac{2(\Omega_\gamma - \Omega_\alpha)}{3\Omega_\alpha}\right]^n \operatorname{sgn}(\Omega_\gamma - \Omega_\alpha) \tag{5.48}$$

$$\sigma\Big|_{S_2} = -\frac{K}{\Sigma}\left[\frac{2(\Omega_\gamma - \Omega_\beta)}{3\Omega_\beta}\right]^n \operatorname{sgn}(\Omega_\gamma - \Omega_\beta) \tag{5.49}$$

Table 5.1: Material properties of Ni_3Sn_4 used in the simulation.

Ω (cm^3/mol)	X_{Ni}^{upper}	X_{Ni}^{lower}	E (GPa)	ν
10.72	0.44	0.427	133 [70]	0.33 [70]

The rates at which the interfaces move at the phase boundaries expressed by Eq. (5.29) and (5.30) now become:

$$dz\Big|_{S_1} = -\frac{dt}{1-c}\left[-(1-c+c\eta)\frac{\partial c}{\partial z} + c(1-c)(1-\eta)\frac{\partial \sigma}{\partial z}\right] \tag{5.50}$$

$$dz\Big|_{S_2} = \frac{dt}{c}\left[-(1-c+c\eta)\frac{\partial c}{\partial z} + c(1-c)(1-\eta)\frac{\partial \sigma}{\partial z}\right] \tag{5.51}$$

where the partial derivatives and the concentrations are evaluated at their boundaries.

Table 5.1 lists some physical properties of the Ni_3Sn_4 IMC under investigation. These include atomic volume, upper and lower bounds of Ni concentration in atomic fraction, Young's modulus, and Poisson's ratio. For Ni and Sn, the atomic volumes are 6.58 and 16.29 cm^3/mol, respectively.

A finite difference method was applied to numerically solve the coupled equations. The calculation begins with a linear concentration and stress profile in the IMC. During a small time step dt, the concentration evolves based on Eq. (5.44), and the stress evolves based on Eq. (5.45). The moving interfaces are updated according to Eqs. (5.50) and (5.51). The concentrations at the phase boundaries are kept constant as governed by Eqs. (5.46)

and (5.47), while the stresses at the phase boundaries are determined by Eqs. (5.48) and (5.49).

5.3 Results and Discussions

5.3.1 A Case Study

Although there has been substantial evidence in the literature that solder failure sometimes occurs in the intermetallic layers or at the IMC interfaces, there are only a few studies on the measurement of mechanical properties of these Sn-based alloys and little quantitative data on their often prescribed brittleness. It has been argued by Lee *et al.* [70] that there is no sufficient scientific evidence to support the statement that IMCs in solder alloys are brittle. Chromik [26] found that the intermetallics typically recovered 30% of the maximum penetration upon unloading during nanoindentation measurements, indicating that the deformation of the intermetallics behaves both elastic and plastic. The stress-strain curve of Ni_3Sn_4 is not readily available, and thus the tensile strength data of IMCs such as Ni_3Sn_4 is largely unknown. However, the yield strength may be estimated from the hardness measurement. Some empirical and approximate theoretical rules-of-thumb have been developed to estimate the yield strength from the hardness. One rule-of-thumb states that [95] the yield strength (or tensile strength in materials that strain harden) is approximately one-third the measured hardness. Fields *et al.* [37] reported the Vicker's hardness of 365 ± 7 kg/mm^2 for Ni_3Sn_4 under room temperature, while the hardness was

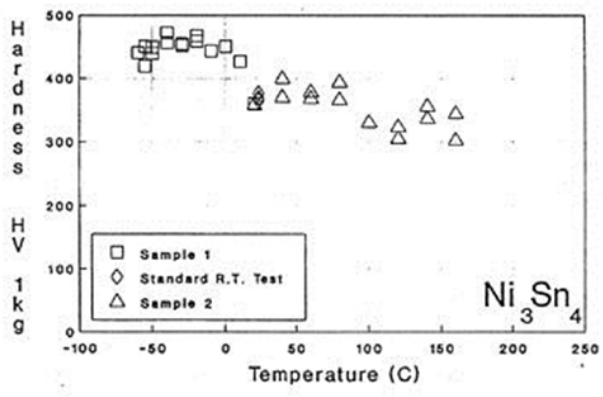

Figure 5.5: Temperature dependence of hardness of Ni_3Sn_4 [37].

found to decrease slightly with increasing temperature as shown in Fig. 5.5. Ghosh [43] reported the Vicker's hardness of Ni_3Sn_4 at room temperature to be 374 ± 22.5 kg/mm^2, which agreed fairly well with that reported by Fields *et al.* Jang *et al.* [55] investigated the nanoindentation characteristics of intermetallics in Pb-free solder alloys and reported that the hardness of Ni_3Sn_4 was 8.12 ± 0.62 GPa, which was much higher than the other two reports. This can be due to the different nanoindentation techniques employed in these studies. In this work, Fields' measurement will be adopted to estimate the yield strength of Ni_3Sn_4 from hardness.

As a case study, an annealing temperature of 200°C was chosen. The hardness value at 200°C was determined by extrapolating the curve from Fig. 5.5, so that the yield strength was estimated to be,

$$\sigma_Y \approx \frac{1}{3}\mathrm{Hv} \approx 100\,\mathrm{kg/mm^2} \approx 1\,\mathrm{GPa} \tag{5.52}$$

In this section, the intermetallic will be assumed for simplicity to be perfectly plastic without work hardening, which leads to $K = 1$ GPa, and $n = 0$. The diffusion coefficients are determined by the simulated annealing method as described in Chapter 3, using the same IMC kinetics data under 200°C. Figure 5.6 shows the simulation results, where each curve represents the concentration or stress distribution along the thickness direction of the IMC. The moving boundaries, S_1 and S_2, are illustrated in the figures. It was found that both concentration and stress follow a linear distribution inside IMC. The concentration profile is straightforward to interpret in that the Ni concentration changes linearly from the upper-bound solubility at Ni-rich side to the lower-bound solubility at Sn-rich side. For stress evolution, it can be seen from Fig 5.6 (b) that the biaxial stress state at the Ni/IMC boundary (near S_1) is compressive, while tensile at the IMC/Sn boundary (near S_2). This is because $\Omega_{\mathrm{Ni}} < \Omega_{\mathrm{IMC}} < \Omega_{\mathrm{Sn}}$, and thus the formation of IMC induces stress states with opposite signs at the two boundaries according to Eq. (5.32). This indicates that the stress gradient built up in the IMC depends on the volumetric change due to IMC formation. In this case, the interface between IMC and solder is of more interest because it is in tension and more prone to void formation. The result is consistent with experimental observations that voids are largely found near the solder-rich side as indicated in Fig 5.7. In the mean time, phase transformation induced stresses are elastically unloaded inside IMC as it grows thicker.

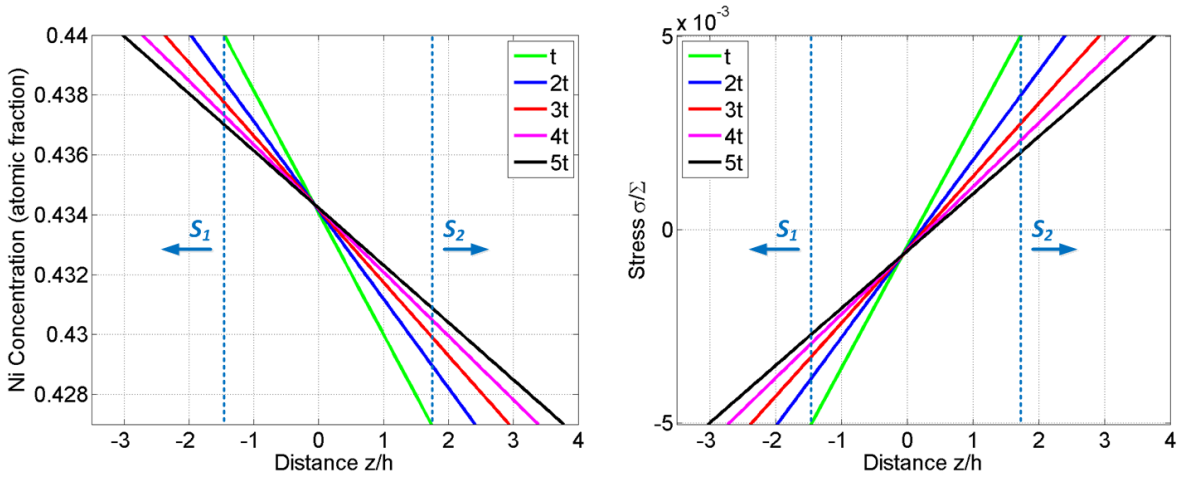

Figure 5.6: Simulation results of (a) concentration evolution, and (b) stress evolution in the IMC.

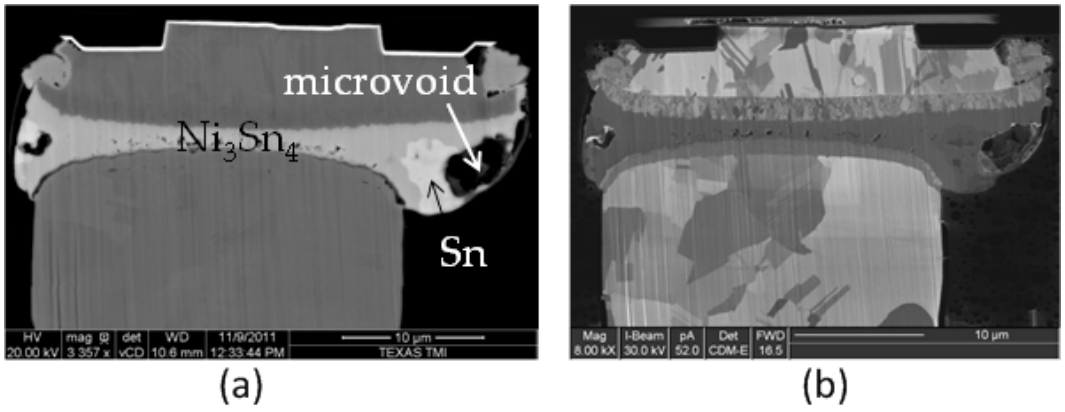

Figure 5.7: (a) SEM and (b) FIB images of a same microbump annealed under 170°C after 225 hours. Microvoid formation was observed as illustrated.

.

5.3.2 Diffusion Induced Stress and its Effect on IMC Growth

For a binary alloy, the diffusivity difference between two elements A and B can result in a stress gradient that drives the atoms to diffuse in opposite directions. This counteracting flux is analogous to the stress-induced EM back flow effect [12] except that the stress gradient generated in the EM back flow effect always acts against the mass transport. Here simulation is performed to study the effect of relative diffusivity on IMC growth. The ratio of diffusivity of component B to A, η, is varied from 0.1 to 1 while keeping the interdiffusivity as constant. The following conditions are used in the simulation: $\widetilde{D} = 1.00 \times 10^{-17}$ m^2/s, $K = 1$ GPa, $n = 0$, and $T = 200°$C. Figure 5.8 plots the IMC thickness as a function of the relative diffusion coefficient. Results show that the IMC growth rate increases as the relative diffusion coefficient decreases. This can be explained from Eq. (5.28). Since the interdiffusion coefficient is kept constant, the value of the first term of the chemical flux depends on the concentration gradient alone. However, in the second term of Eq. (5.28), decreasing the relative diffusivity increases ΔD, and thus increases the stress-induced diffusion. When $D_A = D_B$, $\Delta D = 0$, Eq. (5.28) is back to Darken's analysis.

The magnitude of the relative diffusivity or the the relative mobile component in Ni_3Sn_4 is not clear at this time. Marker experiments are usually performed in order to determine the relative mobilities of the two elements in the intermetallics. Beek *et al.* [106] studied the relative mobilities of Ni and Sn in different Ni-Sn phases using the marker experiment. How-

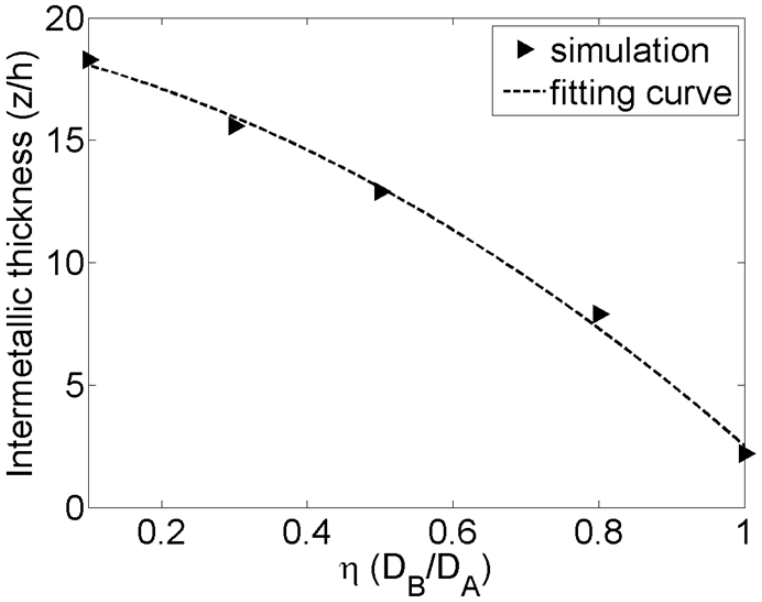

Figure 5.8: Simulated IMC growth as a function of relative diffusivity.

.

Table 5.2: Lattic parameter of Ni_3Sn_4.

Person symbol	a (nm)	b (nm)	c (nm)	β	Reference
Monoclinic	1.2222	0.4064	0.5225	$105°3'$	[45]

ever, they failed to come to a conclusion for the Ni_3Sn_4 phase because the growing layer of Ni_3Sn_4 was not clearly distinguishable in the diffusion couple. Simulation results presented in Chapter 3 (Table 3.2) shows that Ni is a slightly faster diffusing component than Sn in Ni_3Sn_4.

Results in Table 3.2 also indicated that the diffusion coefficients of Ni and Sn in the Ni_3Sn_4 have been found to be within one order of magnitude of each other. It has been argued that diffusion in highly ordered intermetallic compounds occurs through more complex mechanisms because the simple nearest-neighbor jump of a vacancy inevitably leads to disordering of the structure. Nowotny [45] first studied the crystal structure of Ni_3Sn_4 and found it to be monoclinic with 14 atoms per unit cell, with a structure type similar to CoSn (B35). Table 5.2 shows the lattice parameter of Ni_3Sn_4, and Fig. 5.9 shows the crystal structure. The concept of correlated nearest neighbor vacancy jumping that maintains the atomic ordering was first proposed for the B2 atomic structure by Elcock and McCombie [35] and Huntington *et al.* [53] and is called the six-jump cycle (6JC) or the Huntington-McCombie-Elcock (HME) mechanism. The immediate result of the correlated jump mechanism is strong coupling between the component diffusion coefficients

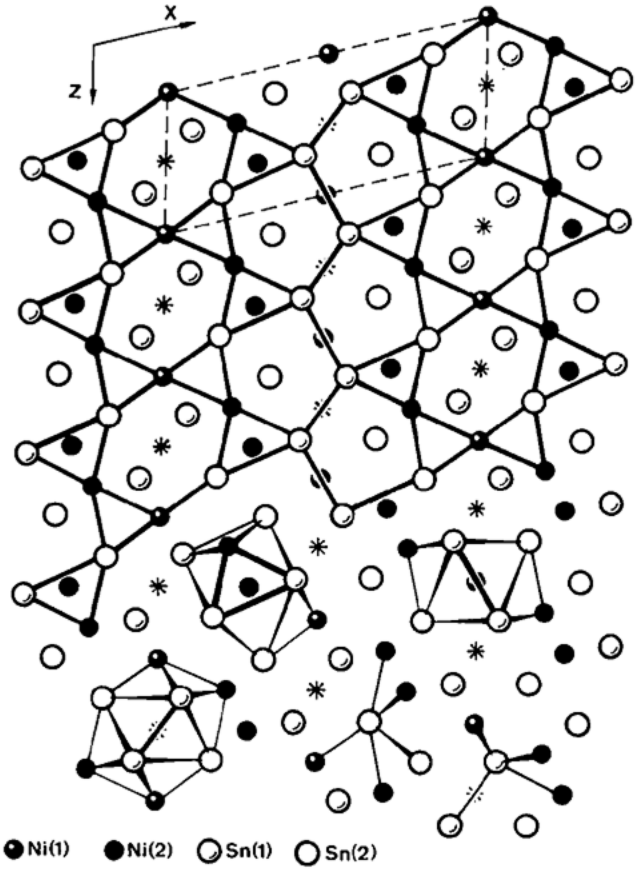

Figure 5.9: Crystal structure of Ni_3Sn_4 [56].

of the intermetallic compounds. Bakker indicated that the 6JC mechanism imposes limits on the ratio of the components diffusivities as follows,

$$0.5 < D_A^* / B_B^* < 2 \tag{5.53}$$

where A and B are the constitutive elements of the binary alloy and D_A^* and D_B^* are the individual tracer diffusion coefficients. The diffusion coefficients that have been estimated in this study are not sufficiently definite to substantiate this relationship. However, the ratios of the two intrinsic diffusion coefficients ($D_{\mathrm{Ni}} / D_{\mathrm{Sn}}$) were in the range of 1.5 to 3.

5.3.3 Phase Transformation-induced Stress and its Effect on IMC Growth

In order to study the effect of phase transformation-induced stress on IMC kinetics, the yield strength K is varied from 0.3 to 3 GPa while keeping the other parameters the same as in the previous case study, and the results are plotted in Fig. 5.10. It is found that the IMC growth rate increases as the yield strength increases. This can be attributed to the fact that an increase in yield strength results in a larger stress gradient inside the intermetallic, and thus enhances the diffusion process.

Perfect plasticity is assumed in the above analysis, which is an ideal case. In reality, the generation of dislocations can hinder the movements of other dislocations and thus suppress the amount of plastic deformation. The extent of work hardening can be characterized by the strain hardening exponent, n, in Eq. (5.35). Therefore, four stress-strain curves are studied

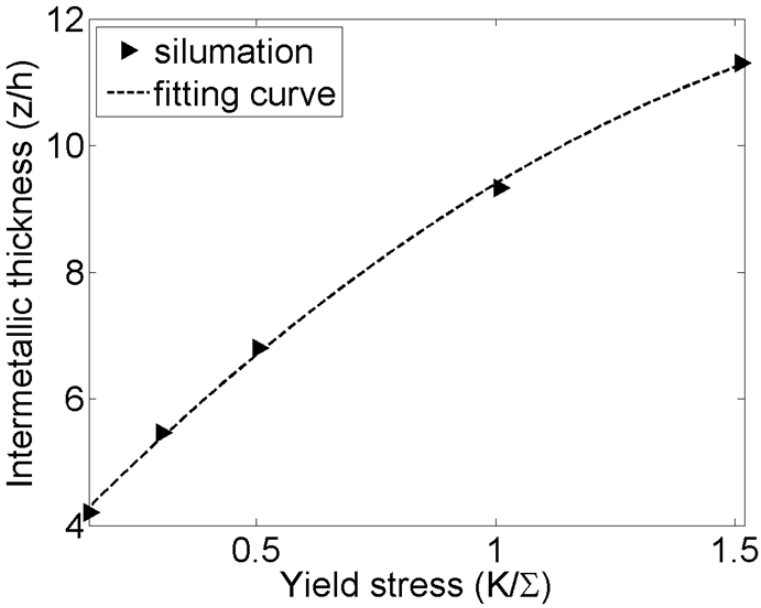

Figure 5.10: Simulated IMC growth as a function of yield stress.

in addition to the case of $n = 0$ in order to investigate the effect of strain hardening exponent on IMC kinetics. The stress-strain relationships with different n's are determined such that the yield strength is kept constant as 1 GPa, and such relationships are plotted in Fig. 5.11. In addition, simulation results of IMC thickness are shown in Fig. 5.12. It can be seen that the varying extent of work hardening plays a role in IMC kinetics as well. An increase in the strain hardening exponent increases the amount of stress at the phase boundaries due to density mismatch during phase transformation, which increases the driving force for diffusion.

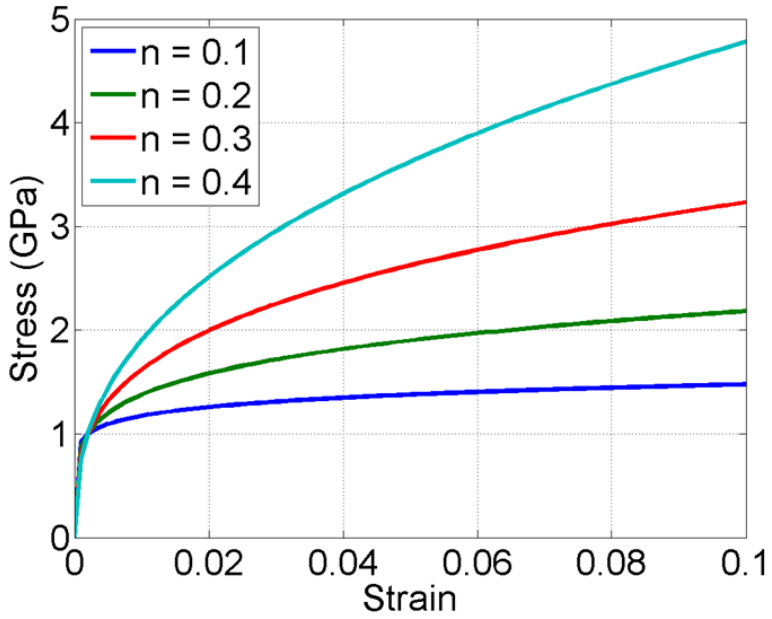

Figure 5.11: Stress-strain curves used in the simulation.

5.3.4 Effect of Stress-induced Diffusion on Estimation of Diffusion Coefficients

In Chapter 3, diffusion coefficients were estimated based on Darken's analysis where the stress effect was ignored. By considering the stress-induced diffusion as analyzed in this chapter, it is expected that diffusion coefficients estimated from the simulated annealing method can be different from those estimated in Chapter 3. Figure 5.13 plots the experimental results of Ni_3Sn_4 growth under 200°C. The results are used to study the effect of stress-induced diffusion on estimation of the diffusion parameters. Perfect plasticity is assumed with varying yield strengths of the material, i.e., $K = 1, 2, 3$ GPa and $n = 0$. Diffusion coefficients of Ni and Sn in Ni_3Sn_4

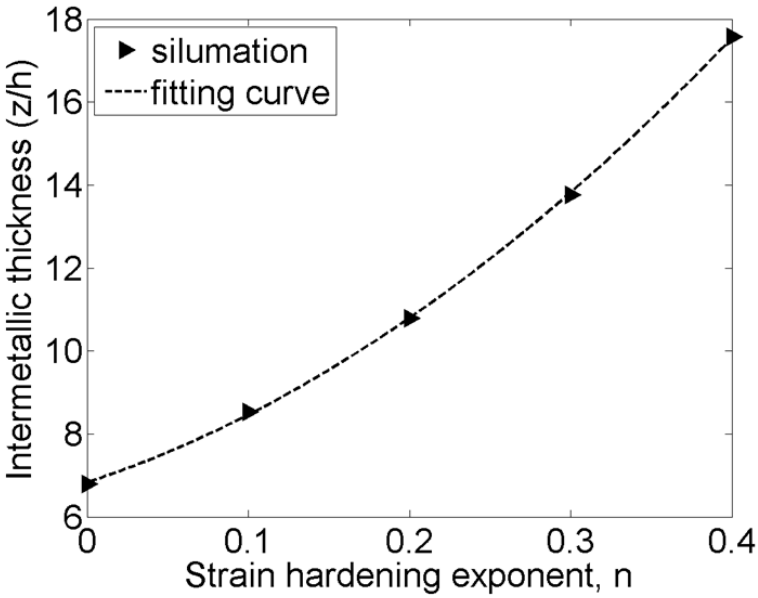

Figure 5.12: Simulated IMC growth as a function of strain hardening exponent, n.

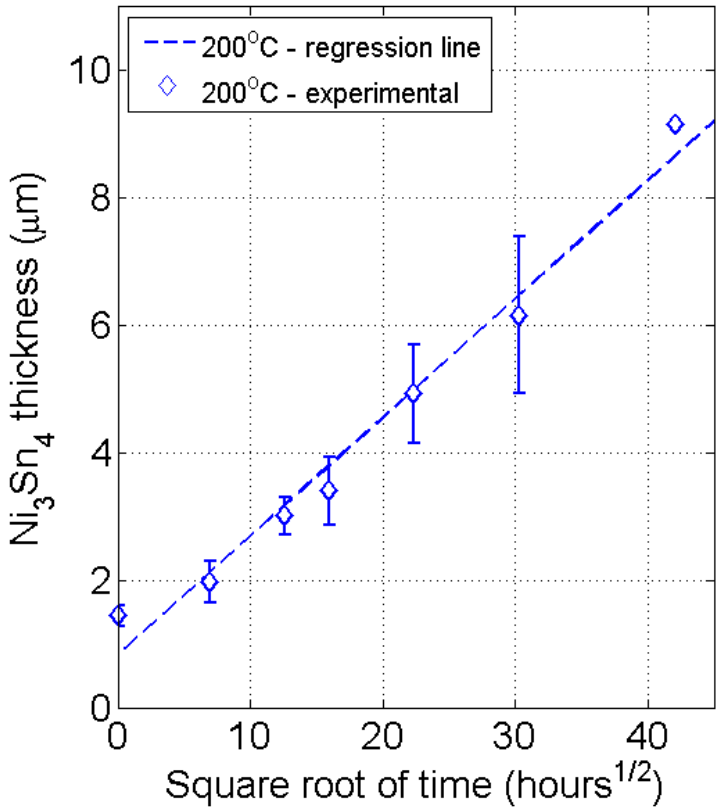

Figure 5.13: Experimental results of Ni_3Sn_4 growth under 200°C.

were estimated using the simulated annealing method and compared with the values obtained in Chapter 3.

The results are summarized in Table 5.3. It is indicated from Table 5.3 that the estimated diffusion parameters decreased as the yield strength of the material increased. Moreover, the parameters were about two orders of magnitude smaller when $K = 3$ GPa as compared to the reference case. This is primarily because the stresses induced by phase transformation at

Table 5.3: Estimated diffusion coefficients of Ni and Sn at 200°C under different IMC yield strengths compared to the reference case.

	D_{Ni} (m^2/s)	D_{Sn} (m^2/s)
Baseline	1.52×10^{-16}	9.90×10^{-17}
$K = 1$ GPa	1.21×10^{-17}	1.05×10^{-17}
$K = 2$ GPa	2.44×10^{-18}	1.57×10^{-18}
$K = 3$ GPa	1.55×10^{-18}	9.70×10^{-19}

the phase boundaries increase as the yield strength increases. This builds up a larger stress gradient inside the IMC. Figure 5.14 illustrates the atomic fluxes in the IMC. It is indicated from Fig. 5.14 that the chemical fluxes of Ni and Sn are in opposite directions resulted from the concentration gradient. The stress gradient, on the other hand, would lead to stress-induced diffusion of Ni and Sn atoms along the same direction from Ni to Sn. Consequently, as the stress gradient increases, the total flux of Ni is enhanced, while that of Sn suppressed. Since the estimated diffusion coefficient of Ni is larger than that of Sn, and hence the overall IMC growth would be enhanced under a larger stress gradient, which leads to smaller diffusion parameters. Although the estimated diffusion parameters may not represent realistic diffusion coefficients, they reflect the kinetics characteristics of IMC growth that can be affected when taking the stress analysis into consideration.

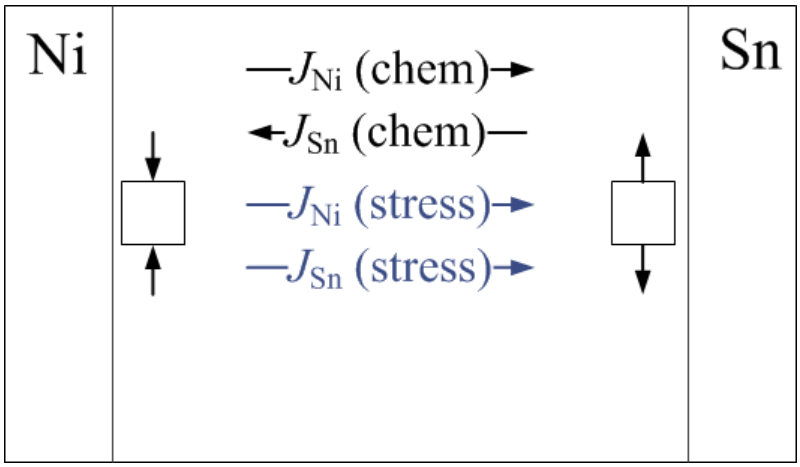

Figure 5.14: Schematic of atomic fluxes in the IMC.

5.3.5 More Examples

It was observed from the case study that both concentration and stress had a linear distribution in the IMC, which indicates that the higher order derivatives in the governing equations are not significant as compared to the first order derivative. However, this may not always be the case. Two more examples are shown here in order to study the effect of diffusion on stress evolution and vise versa. The conditions used in the simulation are the same as those in the previous case study except the plastic properties of the IMCs, and they are listed in Table 5.4.

Figure 5.15 plots the diffusion and stress evolution for case B and C, respectively. Compared to the case study shown in Section 5.3.1, case B and C increase the effective stresses at the phase boundaries by increasing the work hardening exponent or yield strength, resulting in a larger stress gradient. Results in Fig. 5.15(a) and (c) show non-linear characteristics in the

Table 5.4: Parameters of the plastic properties used in the simulation

	Case A (Section 5.3.1)	Case B	Case C
Yield strength, K (GPa)	1	1	10
Work hardening exponent, n	0	0.5	0.5

concentration profiles, especially in Fig. 5.15(c). This suggests that diffusion behavior could be affected by stresses when the stress effect is large enough. On the other hand, linear characteristics in stress profiles are observed in both cases. This could be attributed to the fact that the ratio of the diffusion coefficient of Ni to that of Sn estimated from this study is about 1.5 as indicated from Table 5.3. This value is close to 1 when the two diffusing species have the same diffusivity, which means that the stress caused by unequal diffusion rates of two elements are not significant. Therefore stresses were mainly generated from phase transformation-induced volumetric change at two phase boundaries, leading to a linear stress distribution in the IMC.

5.3.6 Stress in Equilibrium

In the previous analysis, it was assumed that the diffusion couple was semi-infinitely long, which means that the supply of the metal phases α and β are unlimited. This can be considered true for the case of flip chip and ball-grid array solder joints where the amount of the metal and solder are large enough so they would not be completely depleted during the use life-

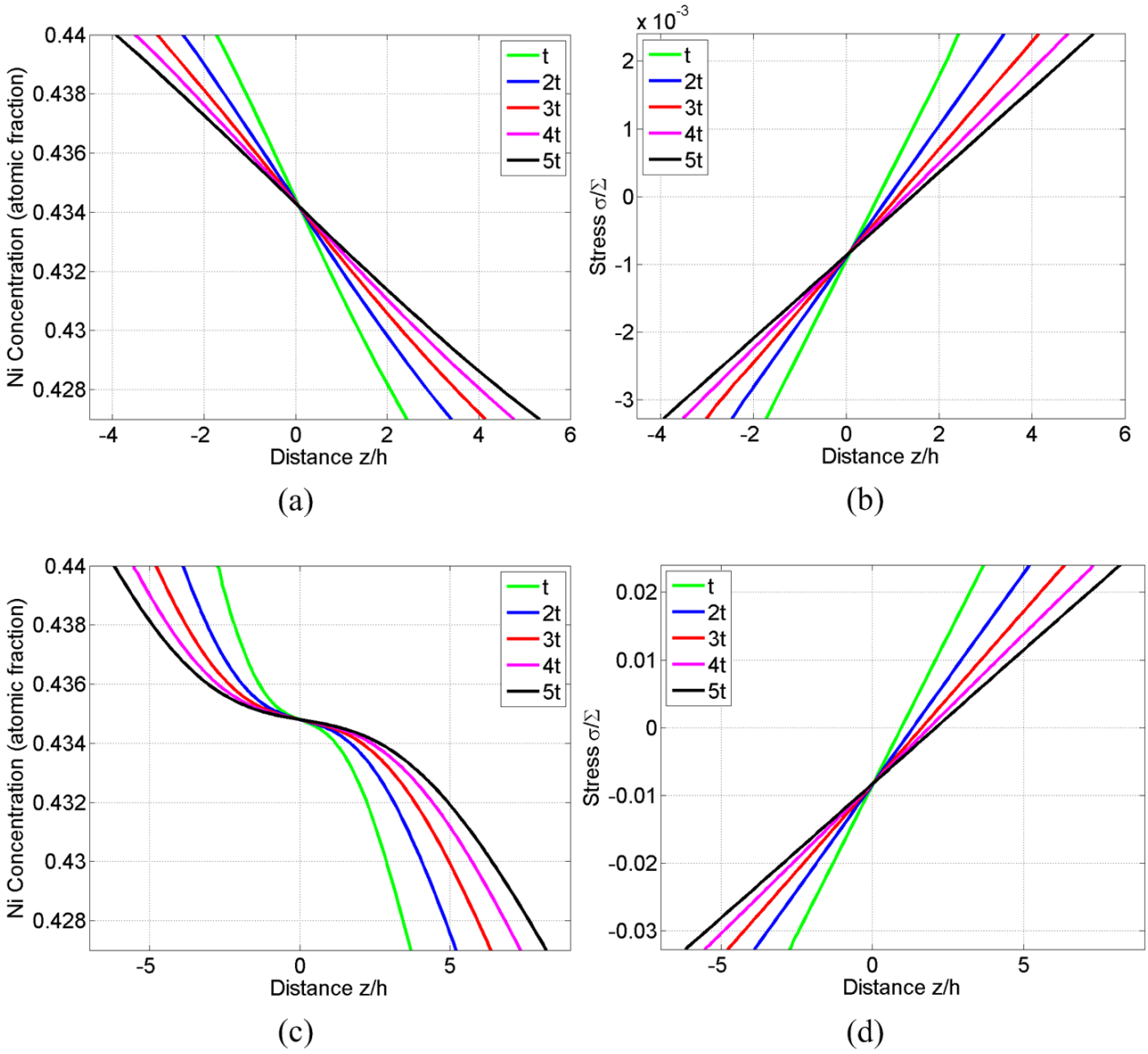

Figure 5.15: Simulation results of (a) concentration and (b) stress evolution when $K = 1$ GPa, $n = 0.5$, and (c) concentration and (d) stress evolution when $K = 10$ GPa, $n = 0.5$.

time of the electronic packages. In 3D technologies, on the other hand, the microbumps connecting between chips have substantially reduced amount of solder as a result of scaling. This can lead to complete consumption of the solder materials upon reaction. Therefore, the model has to be modified to analyze the stress in equilibrium in addition to the transient state.

For Ni_3Sn_4 IMC, the consumed thickness of solder can be estimated by mass conservation,

$$d_{\mathrm{Sn}} = \frac{4m_{\mathrm{Sn}}\,\rho_{\mathrm{IMC}}}{(4m_{\mathrm{Sn}} + 3m_{\mathrm{Ni}})\,\rho_{\mathrm{Sn}}}\,d_{\mathrm{IMC}} \tag{5.54}$$

where m is the atomic weight, ρ is the density, and d is the thickness. A finite Sn thickness is prescribed in the model, and at each iteration step, the solder consumption is checked according to Eq. (5.54). Once Sn is totally consumed, it is assumed that there is no more reaction at the solder/IMC interface, so that the net flux across the interface vanishes. This leads to the new boundary conditions,

$$\left.\frac{dc}{dz}\right|_{S_2} = 0 \tag{5.55}$$

$$\left.\frac{d\sigma}{dz}\right|_{S_2} = 0 \tag{5.56}$$

Figure 5.16 shows the stress distribution in the microbumps after total Sn consumption with varying n values. Results show that the stress becomes uniform and reaches a steady-state after the solid-state reaction stops. The stresses are tensile because the reaction between Ni and Sn follows

$$3\mathrm{Ni} + 4\mathrm{Sn} \longrightarrow \mathrm{Ni_3Sn_4} \tag{5.57}$$

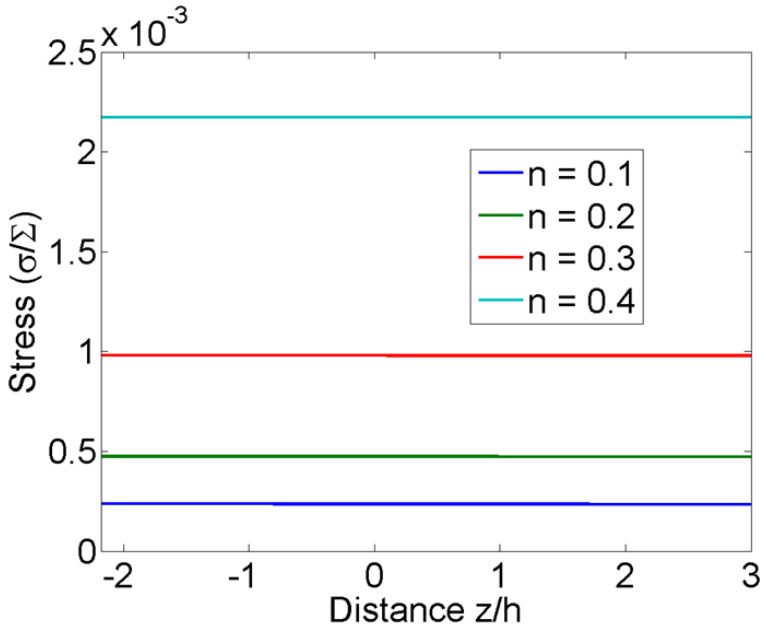

Figure 5.16: Stress distribution in microbumps after total Sn consumption.

The molar volumes of Ni, Sn, and Ni_3Sn_4 are 6.58, 16.29, and 75.04 cm^3/mol, respectively. The density mismatch causes a net volume shrinkage of 11.6%. This negative volume change makes the IMC in tension due to the confinement effect. The absolute value of the steady-state stress depends on the mechanical properties of the intermetallic. The stress is smaller within softer materials (smaller n) since stress is relaxed more via plastic deformation.

5.4 Summary

In this chapter, a numerical model has been developed to study concurrent diffusion, phase transformation, and deformation in the formation process of intermetallic compound. Two processes that can generate stress

are considered in the model. The first one is due to unequal diffusion rates of the two components A and B, which leads to a flux divergence. The second originates from a net volumetric change during phase transformation. The volumetric strain at the phase boundaries are too large to be compatible with elastic deformation alone. To rectify the conflict, plastic deformation are considered at the interfaces, setting up a biaxial stress field in the plane directions normal to the film thickness. The case of Ni_3Sn_4 formation in the Ni-Sn solder system is investigated to evaluate concentration and stress evolution in the intermetallics during solid-state reaction. Simulation results show that the Ni/IMC interface is in compression while the solder/IMC interface is in tension. The IMC growth rate depends on the relative diffusion rates as well as the mechanical properties of the itnermetallic. Finally, a finite thickness of the diffusion couple is considered to investigate the stress in equilibrium.

Chapter 6

Conclusions and Future Work

We have found it of paramount importance that in order to progress we must recognize the ignorance and leave room for doubt. Scientific knowledge is a body of statements of varying degrees of certainty - some most unsure, some nearly sure, none absolutely certain.

Richard Feynman

6.1 Conclusions

The effects of intermetallic compound (IMC) formation on reliability of Pb-free Sn-based solders for flip chip and three-dimensional (3D) interconnects have been studied. For flip chip solder joints, the IMC kinetics is important in controlling the electromigration (EM) reliability. The introduction of Pb-free Sn-based solder materials and its anisotropic characteristics give rise to new reliability challenges. In the first part of the dissertation, the effect of Sn grain orientation on EM reliability of Pb-free Sn-based solder joints was studied. The Sn grain microstructure was characterized and correlated with the EM test results. It was found that the EM failure mode

was closely related to the relative alignment of the *c*-axis of the Sn crystal with respect to the electron flow direction. The grain structural optimization was also explored. It was suggested that multiple solder reflows that produced multi-grain structure with high-angle twin boundaries would be an effective approach to improve the EM reliability. In addition to the experimental work, a kinetic analysis was formulated to study the early failure mechanism in Sn-based solder joints with Ni under-bump metallization (UBM). A numerical model was formulated to incorporate the anisotropic diffusion properties of Ni in solder. Both IMC growth rate and UBM consumption rate were calculated and found to be dependent on Sn grain orientations. Numerical predictions were found to be consistent with the experimental observations, which provided a theoretical base to account for the EM degradation mechanisms.

In the aforementioned kinetic analysis, the intrinsic diffusion coefficients in IMCs were not readily available in the literature. In this study, an effective Monte Carlo method known as simulated annealing was used to estimate the unknown parameters by fitting the model predictions with experimental measurements. The intrinsic diffusion coefficients of Ni and Sn in Ni_3Sn_4 between 150 and 200°C, and those of Cu and Sn in Cu_3Sn and Cu_6Sn_5 between 120 and 200°C were estimated. The interdiffusion coefficients calculated from the simulation results of the intrinsic coefficients were found to be in good agreement with the values reported in the literature, which did exist. The parameters estimated from simulated annealing were

applied to the numerical model to predict IMC growth, which was found to be consistent with the experimental growth data. In addition, activation energies for the diffusion coefficients were determined, which enabled the prediction of intermetallic growth at any temperature within the practical use temperature range.

Recently, 3D integration with through-silicon vias (TSVs) has emerged as an effective solution to overcome the wiring limit beyond 32 nm node technology. Sn-based microbumping, which provide connection between stacking chips, is one of the key technologies in 3D integration. Unlike the flip chip solder joints which are mostly composed of solder, microbumps consist of a large amount of IMC due to significant reduction in the amount of Sn present. This change can affect the reliability of 3D IC microbumps. In this study, the EM reliability of TSV microbump joints was investigated. Results showed no EM-induced damage in the microbumps after 1200 hours of EM testing. This was mainly because the solder in the microbumps were fully converted into IMCs after assembly or under testing. Optimization of UBM and bump configuration was also discussed for an improved overall reliability of the microbumps.

Despite of the superior EM reliability for the 3D IC microbumps, experimental observations of void and crack formation in the microbumps under thermal annealing imply that stress management becomes a new challenge for microbump reliability. In this study, a numerical analysis was formulated to study concurrent diffusion, phase transformation, and defor-

mation in the formation of IMCs. Stress generation due to unbalanced diffusion rates and phase transformation-induced volumetric change was considered in the model. The coupled analysis was applied to study the Ni_3Sn_4 formation in the Ni-Sn microbumping system. Simulation results showed that the Ni/IMC interface was in compression whereas the solder/IMC interface was in tension. It was found that the IMC growth kinetics depended on the relative diffusion rates of the two components as well as the mechanical properties of the intermetallics. Finally, the modeled diffusion couple that was infinitely long was modified to one with finite thickness in order to study the steady-state stress. Together, the results offered a better understanding of stress evolution in Sn-based microbumps with Ni metallization due to diffusion and phase transformation.

6.2 Future Work

In the EM reliability study on flip chip solder joints, the process of multiple solder reflows was proposed as one of the approaches to optimize the Sn grain structure. The study, however, only compared solder joints between single and five times of reflows. It would therefore be interesting to investigate the effect of number of solder reflows on microstructure change in flip chip solder joints. Besides, it is worth exploring other solutions to control the Sn grain structure of Pb-free solder joints, such as solder size, composition, temperature of solidification, cooling rates, etc.

Regarding the stress analysis in 3D IC microbumps, the numerical

analysis is not complete due to the lack of accurate measurement on the mechanical properties of the intermetallics under investigation. Nanoindentation test can be considered to characterize the mechanical properties of intermetallics in Sn-based microbumps. Furthermore, it would be essential to develop experimental methods for stress analysis and to correlate the experimental measurements with the simulation results. For example, synchrotron X-ray microdiffraction technique could be an effective method to measure the residual stress in the microbumps after thermal cycling. High resolution Moiré interferometry that measures the in-plane displacement and strain distributions with high resolution and high sensitivity can be another possibility. In addition, the modeling study presented in Chapter 5 focused on stress analysis in the IMC. It would be of practical interest if the model can be extended to analyze crack formation, which has been identified as one of the failure mechanisms in 3D IC microbumps. To achieve this, finite element analysis (FEA) might be applied to calculate the crack driving force at interfaces possessing tensile stresses, using the material parameters obtained from this study as an input.

Appendices

Appendix A

Diffusion Treatment in the Solder Phase

The diffusion coefficient of Ni in Sn is many orders of magnitude higher than those in the IMC phase. Here we calculated the characteristic length L as a measure of how far the Ni atoms have diffused in the z-direction at time t. Take the diffusion coefficients at 170°C and assume $t = 10$ min,

$$L_{\parallel} = \sqrt{D_{\parallel} t} = \sqrt{1.47 \times 10^{-8} \times 10 \times 60} \approx 3000\mu\text{m}$$

$$L_{\perp} = \sqrt{D_{\perp} t} = \sqrt{7.73 \times 10^{-11} \times 10 \times 60} \approx 200\mu\text{m}$$

As we can see, the characteristic length is much larger than the thickness of a flip chip solder joint (50-100 μm), which means that the fast interstitial diffusion of Ni would smooth out any concentration gradient within a short amount of time. Therefore, the solder phase can be treated as a phase saturated with Ni in the model described in Chapter 2.

Appendix B

Interface Migration Treatment with Solid-State Phase Transformation

In the case of solid state phase transformation, differences in density exist. For example, the molar volume of Ni, Ni_3Sn_4, and Sn are 6.58, 10.72, and 16.13 cm^3/mol, respectively. Therefore, the total volume of the system is not a constant. To deal with this problem, I followed the analysis in [7]. First, independent governing equations for diffusion and stress evolution is obtained in each phase, which are discussed in the preceding sections. Then identify frames for analyzing diffusion in each phase. Finally find the relationship between them via mass conservation in order to construct the Stefan condition at the interface.

Consider a phase boundary S between the moving phases α and β, as shown in Fig. B.1. Mass conservation requires that

$$N_{i,\beta}\Big|_S - \dot{S}^{\beta} C_i^{\beta\alpha} = N_{i,\alpha}\Big|_S - \dot{S}^{\alpha} C_i^{\alpha\beta} \quad (i = A, B) \tag{B.1}$$

where

$N_{i,\alpha}\Big|_S$ = flux of i into phase α at the interface measured in the α phase frame.

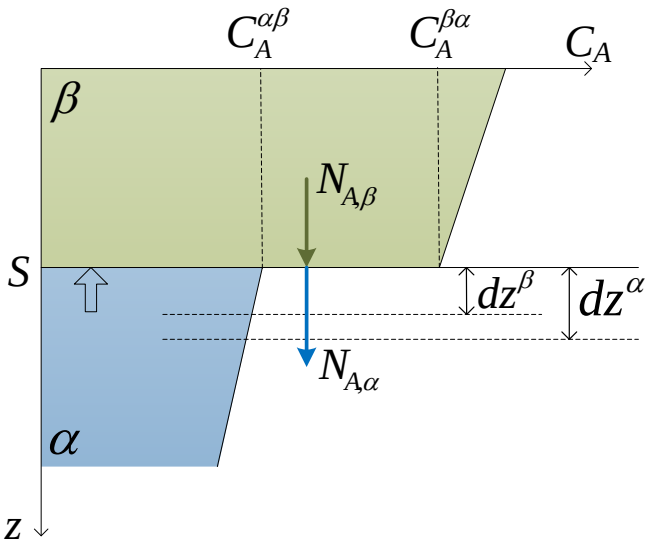

Figure B.1: Schematic of the concentration profile near the interface of α and β.

$N_{i,\beta}\Big|_S$ = flux of i into phase β at the interface measured in the β phase frame.

$\dot{S}^{\alpha}$ = velocity of the interface measured in the α phase frame.

$\dot{S}^{\beta}$ = velocity of the interface measured in the β phase frame.

$C_i^{\alpha\beta}$ = concentration of i at the interface on the α side.

$C_i^{\beta\alpha}$ = concentration of i at the interface on the β side.

The solutions to $\dot{S}^{\alpha}$ and $\dot{S}^{\beta}$ can be obtained by solving Eq. (B.1) for $i = A, B$ along with Eq. (5.3) and (5.11). The results are

$$\dot{S}^{\alpha} = \frac{\Omega_{\alpha}}{X_A^{\beta\alpha} - X_A^{\alpha\beta}} (N_{A,\beta}\Big|_S - N_{A,\alpha}\Big|_S) \tag{B.2}$$

and

$$\dot{S}^{\beta} = \frac{\Omega_{\beta}}{X_A^{\beta\alpha} - X_A^{\alpha\beta}} (N_{A,\beta}\Big|_S - N_{A,\alpha}\Big|_S) \tag{B.3}$$

As we can see, in the special case where $\Omega_{\alpha} = \Omega_{\beta}$, $\dot{S}^{\alpha} = \dot{S}^{\beta}$. There is no volume change or relative displacements of the phases.

By taking the time step infinitesimally small, we obtain the interface migration with respect to their own frames.

$$dz^{\alpha} = \frac{\Omega_{\alpha}}{X_A^{\beta\alpha} - X_A^{\alpha\beta}} (N_{A,\beta}\Big|_S - N_{A,\alpha}\Big|_S) dt \tag{B.4}$$

$$dz^{\beta} = \frac{\Omega_{\beta}}{X_A^{\beta\alpha} - X_A^{\alpha\beta}} (N_{A,\beta}\Big|_S - N_{A,\alpha}\Big|_S) dt \tag{B.5}$$

Bibliography

[1] Moore's law. http://en.wikipedia.org/wiki/Moore's_law.

[2] Rent's rule. http://en.wikipedia.org/wiki/Rent's_rule.

[3] Roadmap for 3d integration with tsvs. http://www.gslb.cleanrooms.com.

[4] I. E. Anderson. Development of Sn-Ag-Cu and Sn-Ag-Cu-X alloys for Pb-free electronic solder applications. In *Lead-Free Electronic Solders*, pages 55 – 76. 2007.

[5] B. Arfaei, N. Kim, and E. J. Cotts. Dependence of Sn grain morphology of Sn-Ag-Cu solder on solidification temperature. *Journal of Electronic Materials*, 41(2):362 – 374, 2012.

[6] S. Bader, W. Gust, and H. Hieber. Rapid formation of intermetallic compounds interdiffusion in the Cu-Sn and Ni-Sn systems. *Acta Metallurgica et Mterialia*, 43(1):329 – 337, 1995.

[7] R. W. Balluffi, S. M. Allen, and W. C. Carter. *Kinetics of Materials*. Wiley-Interscience, 1 edition, September 2005.

[8] D. L. Beke, I. A. Szabó, Z. Erdélyi, and G. Opposits. Diffusion-induced stresses and their relaxation. *Materials Science and Engineering: A*, 387:4 – 10, 2004.

[9] T. R. Bieler, H. Jiang, L. P. Lehman, T. Kirkpatrick, E. J. Cotts, and B. Nandagopal. Influence of Sn grain size and orientation on the thermomechanical response and reliability of Pb-free solder joints. *Components and Packaging Technologies*, 31(2):370–381, 2008.

[10] J. R. Black. Electromigration failure modes in aluminum metallization for semiconductor devices. *Proceedings of the IEEE*, 57(9):1587–1594, 1969.

[11] H. D Blair, T.-Y. Pan, and J. M. Nicholson. Intermetallic compound growth on Ni, Au/Ni, and Pd/Ni substrates with Sn/Pb, Sn/Ag, and Sn solders. In *IEEE Proceedings of Electronic Components and Technology Conference*, pages 259 – 267, 1998.

[12] I. A. Blech. Electromigration in thin aluminum films on titanium nitride. *Journal of Applied Physics*, 47(4):1203 – 1208, 1976.

[13] P. Carnevali, L. Coletti, and S. Patarnello. Image processing by simulated annealing. *IBM Journal of Research and Development*, 29(6):569–579, 1985.

[14] S.-H. Chae. *Electromigration and Thermomigration Reliability of Lead-Free Solder Joints for Advanced Packaging Applications*. PhD thesis, Uni-

versity of Texas at Austin, 2010.

[15] S.-H. Chae, Y. Wang, and P. S. Ho. *Electromigration Reliability of Pb-Free Solder Joints*, pages 337 – 373. John Wiley & Sons, 2012.

[16] B. Chao, S.-H. Chae, X. Zhang, K.-H. Lu, M. Ding, J. Im, and P. S. Ho. Electromigration enhanced intermetallic growth and void formation in Pb-free solder joints. *Journal of Applied Physics*, 100(8):084909, 2006.

[17] B. Chao, S.-H. Chae, X. Zhang, K.-H. Lu, J. Im, and P. S. Ho. Investigation of diffusion and electromigration parameters for Cu-Sn intermetallic compounds in Pb-free solders using simulated annealing. *Acta Materialia*, 55(8):2805 – 2814, 2007.

[18] B. Chao, X. Zhang, S.-H. Chae, and P. S. Ho. Recent advances on kinetic analysis of electromigration enhanced intermetallic growth and damage formation in Pb-free solder joints. *Microelectronics Reliability*, 49(3):253 – 263, 2009.

[19] H.-L. Chao. *Electromigration enhanced kinetics of Cu-Sn intermetallic compounds in Pb free solder joints and Cu low-k dual damascne processing using step and flash imprint lithography*. PhD thesis, University of Texas at Austin, 2009.

[20] Q. Chen, D. Zhang, Z. Wang, L. Liu, and J.-Q. Lu. Chip-to-wafer (C2W) 3D integration with well-controlled template alignment and

wafer-level bonding. In *IEEE Proceedings of Electronic Components and Technology Conference*, pages 1–6, 2011.

[21] R.-S. Cheng, H.-J. Chang, T.-C. Chang, and J.-H. Chou. Early failure induced by phase transformation in microjoints for chip-level integration. *Electrochemical and Solid-State Letters*, 15(3):H75 – H77, 2012.

[22] S. H. Chiu, T. L. Shao, C. Chen, D. J. Yao, and C. Y. Hsu. Infrared microscopy of hot spots induced by joule heating in flip-chip SnAg solder joints under accelerated electromigration. *Applied Physics Letters*, 88(2):022110–3, 2006.

[23] T.-C. Chiu, K. Zeng, R. Stierman, D. Edwards, and K. Ano. Effect of thermal aging on board level drop reliability for Pb-free BGA packages. In *IEEE Proceedings of Electronic Components and Technology Conference*, volume 2, pages 1256 – 1262, 2004.

[24] S. Cho. Technical challenges in TSV integration. In *RTI 3D Architectures for Semiconductor Integration and Packaging Conference (3D ASIP)*, 2010.

[25] W. K. Choi and H. M. Lee. Prediction of primary intermetallic compound formation during interfacial reaction between Sn-based solder and ni substrate. *Scripta Materialia*, 46(11):777 – 781, 2002.

[26] R. R. Chromik, R. P. Vinci, S. L. Allen, and M. R. Notis. Measuring the mechanical properties of Pb-free solder and Sn-based intermetallics

by nanoindentation. *JOM*, 55(6):66 – 69, 2003.

[27] P. Coudrain, D. Henry, A. Berthelot, J. Charbonnier, S. Verrun, R. Franiatte, N. Bouzaida, G. Cibrario, F. Calmon, I. O'Connor, et al. 3D integration of CMOS image sensor with coprocessor using TSV last and micro-bumps technologies. In *IEEE Proceedings of Electronic Components and Technology Conference*, pages 674 – 682. IEEE, 2013.

[28] L. S. Darken. Diffusion, mobility and their interrelation through free energy in binary metallic systems. *Trans. Aime*, 175(1):184 – 194, 1948.

[29] I. De Sousa, D. W. Henderson, L. Parry, S. K. Kang, and D.-Y. Shih. The influence of low level doping on the thermal evolution of SAC alloy solder joints with Cu pad structures. In *IEEE Proceedings of Electronic Components and Technology Conference*, page 1545, 2006.

[30] M. Ding. *Investigation of electromigration reliability of solder joints in flip chip packages*. PhD thesis, University of Texas at Austin, 2007.

[31] EU Directive. Directive 2002/95/EC of the european parliament and of the council of 27 January 2003 on the restriction of the use of certain hazardous substances in electrical and electronic equipment. *Official Journal of the European Union*, 13:L37, 2003.

[32] K. F. Dreyer, W. K. Neils, R. R. Chromik, D. Grosman, and E. J. Cotts. Calorimetric study of the energetics and kinetics of interdiffusion in

Cu/Cu_6Sn_5 thin-film diffusion couples. *Applied physics letters*, 67(19):2795 – 2797, 1995.

[33] R. Dunne, Y. Takahashi, K. Mawatari, M. Matsuura, T. Bonifield, P. Steinmann, and D. Stepniak. Development of a stacked WCSP package platform using TSV (through-silicon via) technology. In *IEEE Proceedings of Electronic Components and Technology Conference*, pages 1062 – 1067, 2012.

[34] B. F. Dyson, T. R. Anthony, and D. Turnbull. Interstitial diffusion of copper in tin. *Journal of Applied Physics*, 38(8):3408 – 3408, 1967.

[35] E. W. Elcock and C. W. McCombie. Vacancy diffusion in binary ordered alloys. *Physical Review*, 109(2):605, 1958.

[36] O. Engler and V. Randle. *Introduction to Texture Analysis: Macrotexture, Microtexture, and Orientation Mapping, Second Edition*. Taylor & Francis, 2010.

[37] R. J. Fields, S. R. Low, G. K. Lucey Jr, M. J. Cieslak, J. H. Perepezko, S. Kang, and M. E. Glicksman. The metal science of joining. *TMS*, pages 165 – 173, 1992.

[38] H. Flandorfer, U. Saeed, C. Luef, A. Sabbar, and H. Ipser. Interfaces in lead-free solder alloys: Enthalpy of formation of binary Ag-Sn, Cu-Sn and Ni-Sn intermetallic compounds. *Thermochimica Acta*, 459(1):34 – 39, 2007.

[39] W. F. Gale and T. C. Totemeier. *Smithells Metals Reference Book*. Elsevier Science, 2003.

[40] H. Gan and K. N. Tu. Polarity effect of electromigration on kinetics of intermetallic compound formation in Pb-free solder V-groove samples. *Journal of Applied Physics*, 97(6):063514–10, 2005.

[41] A Gangulee, G. C. Das, and M. B. Bever. An x-ray diffraction and calorimetric investigation of the compound Cu_6Sn_5. *Metallurgical Transactions*, 4(9):2063 – 2066, 1973.

[42] R. J. Gdanitz. Prediction of molecular crystal structures by Monte Carlo simulated annealing without reference to diffraction data. *Chemical Physics Letters*, 190(3):391 – 396, 1992.

[43] G. Ghosh. Elastic properties, hardness, and indentation fracture toughness of intermetallics relevant to electronic packaging. *Journal of Materials Research*, 19(05):1439 – 1454, 2004.

[44] P. A. Gruber, L. Bélanger, G. P. Brouillette, D. H. Danovitch, J.-L. Landreville, D. T. Naugle, V. A. Oberson, D.-Y. Shih, C. L. Tessler, and M. R. Turgeon. Low-cost wafer bumping. *IBM Journal of Research and Development*, 49(4.5):621 – 639, 2005.

[45] K. Schubert H, Nowotny. On the crystal structure of ni3sn4. *Naturwissenschaften*, 32(76), 1944.

[46] D. J. Hathaway, R. R. Habra, E. C. Schanzenbach, and S. J. Rothman. Circuit placement, chip optimization, and wire routing for IBM IC technology. *IBM Journal of Research and Development*, 40(4):453 – 460, 1996.

[47] D. Henry, F. Jacquet, M. Neyret, X. Baillin, T. Enot, V. Lapras, C. Brunet-Manquat, J. Charbonnier, B. Aventurier, and N. Sillon. Through silicon vias technology for CMOS image sensors packaging. In *IEEE Proceedings of Electronic Components and Technology Conference*, pages 556 – 562, 2008.

[48] C. E. Ho, R. Y. Tsai, Y. L. Lin, and C. R. Kao. Effect of Cu concentration on the reactions between Sn-Ag-Cu solders and Ni. *journal of Electronic Materials*, 31(6):584 – 590, 2002.

[49] K. Hoshino, Y. Iijima, and K.-I. Hirano. Interdiffusion and kirkendall effect in Cu-Sn alloys. *Trans. Jpn. Inst. Met.*, 21(10):674 – 682, 1980.

[50] Z. Huang, R. Chatterjee, P. Justison, R. Hernandez, S. Pozder, A. Jain, E. Acosta, D. A. Gajewski, V. Mathew, and R. E. Jones. Electromigration of Cu-Sn-Cu micropads in 3D interconnect. In *IEEE Proceedings of Electronic Components and Technology Conference*, pages 12 – 17, 2008.

[51] R. R. Hultgren. *Selected Values of the Thermodynamic Properties of Binary Alloys*. American Society for Metals, 1973.

[52] H. B. Huntington. Electromigration in metals. *Diffusion in Solids: Recent Developments*, page 303, 1975.

[53] H. B. Huntington, N. C. Miller, and V. Nerses. Self-diffusion in 50-50 gold-cadmium. *Acta Metallurgica*, 9(8):749 – 754, 1961.

[54] M. B. Bever J. B. Cohen, J. S Leach. *JOM*, 6:1257–1259, 1954.

[55] G.-Y. Jang, J.-W. Lee, and J.-G. Duh. The nanoindentation characteristics of Cu_6Sn_5, Cu_3Sn, and Ni_3Sn_4 intermetallic compounds in the solder bump. *Journal of Electronic Materials*, 33(10):1103 – 1110, 2004.

[56] W Jeitschko and B Jaberg. Structure refinement of Ni_3Sn_4. *Acta Crystallographica Section B: Structural Crystallography and Crystal Chemistry*, 38(2):598 – 600, 1982.

[57] S. K Kang, P. Lauro, D.-Y. Shih, D. W. Henderson, J. Bartelo, T. Gosselin, S. R. Cain, C. Goldsmith, K. Puttlitz, T. K. Hwang, et al. The microstructure, thermal fatigue, and failure analysis of near-ternary eutectic Sn-Ag-Cu solder joints. *Materials Transactions*, 45(3):695 – 702, 2004.

[58] S. K. Kang, P. Lauro, D.-Y. Shih, D. W. Henderson, and K. J. Puttlitz. Microstructure and mechanical properties of lead-free solders and solder joints used in microelectronic applications. *IBM Journal of Research and Development*, 49(4.5):607 – 620, 2005.

[59] S. K. Kang, R. S. Rai, and S. Purushothaman. Interfacial reactions during soldering with lead-tin eutectic and lead (Pb)-free, tin-rich solders. *Journal of Electronic Materials*, 25(7):1113 – 1120, 1996.

[60] S. K. Kang and A. K. Sarkhel. Lead (Pb)-free solders for electronic packaging. *Journal of Electronic Materials*, 23(8):701 – 707, 1994.

[61] S. K. Kang, D.-Y. Shih, D. Leonard, D. W. Henderson, T. Gosselin, S. Cho, J. Yu, and W. K. Choi. Controlling Ag_3Sn plate formation in near-ternary-eutectic Sn-Ag-Cu solder by minor Zn alloying. *J. Miner., Met. Mater.*, 56(6):34 – 38, 2004.

[62] U. Kang, H.-J. Chung, S. Heo, S.-H. Ahn, H. Lee, S.-H. Cha, J. Ahn, D. Kwon, J. H. Kim, J.-W. Lee, et al. 8Gb 3D DDR3 DRAM using through-silicon-via technology. In *Solid-State Circuits Conference-Digest of Technical Papers*, pages 130 – 131, 2009.

[63] S. Kirkpatrick, D. G. Jr., and M. P. Vecchi. Optimization by simmulated annealing. *Science*, 220(4598):671 – 680, 1983.

[64] O. J. Kleppa. Heat of formation of solid and liquid binary alloys of copper with cadmium, indium, tin and antimony at 450. *The Journal of Physical Chemistry*, 60(7):852 – 858, 1956.

[65] J. U. Knickerbocker, P. S. Andry, B. Dang, R. R. Horton, C. S. Patel, R. J. Polastre, K. Sakuma, E. S. Sprogis, C. K. Tsang, B. C. Webb, et al. 3D

silicon integration. In *IEEE Proceedings of Electronic Components and Technology Conference*, pages 538 – 543, 2008.

[66] N. Kumar, S. Ramaswami, J. Dukovic, J. Tseng, R. Ding, N. Rajagopalan, B. Eaton, R. Mishra, R. Yalamanchili, Z. Wang, et al. Robust TSV via-middle and via-reveal process integration accomplished through characterization and management of sources of variation. In *IEEE Proceedings of Electronic Components and Technology Conference*, pages 787 – 793, 2012.

[67] S. Kumar, C. A. Handwerker, and M. A. Dayananda. Intrinsic and interdiffusion in Cu-Sn system. *Journal of Phase Equilibria and Diffusion*, 32(4):309 – 319, 2011.

[68] R. Labie, W. Ruythooren, K. Baert, E. Beyne, and B. Swinnen. Resistance to electromigration of purely intermetallic micro-bump interconnections for 3D-device stacking. In *IEEE Proceedings of Interconnect Technology Conference*, pages 19 – 21, 2008.

[69] R. Labie, W. Ruythooren, and J. Van Humbeeck. Solid state diffusion in Cu-Sn and Ni-Sn diffusion couples with flip-chip scale dimensions. *Intermetallics*, 15(3):396 – 403, 2007.

[70] C. C. Lee, P. J. Wang, and J. S. Kim. Are intermetallics in solder joints really brittle? In *IEEE Proceedings of Electronic Components and Technology Conference*, pages 648 – 652, 2007.

[71] K. Lee, K.-S. Kim, Y. Tsukada, K. Suganuma, K. Yamanaka, S. Kuritani, and M. Ueshima. Effects of the crystallographic orientation of Sn on the electromigration of Cu/Sn-Ag-Cu/Cu ball joints. *Journal of Materials Research*, 26(3):467, 2011.

[72] T.-K. Lee, B. Zhou, L. Blair, K.-C. Liu, and T. R. Bieler. Sn-Ag-Cu solder joint microstructure and orientation evolution as a function of position and thermal cycles in ball grid arrays using orientation imaging microscopy. *Journal of Electronic Materials*, 39(12):2588–2597, 2010.

[73] Y.-M. Lin, C.-J. Zhan, J.-Y. Juang, J. H. Lau, T.-H. Chen, R. Lo, M. Kao, T. Tian, and K.-N. Tu. Electromigration in Ni/Sn intermetallic microbump joint for 3D IC chip stacking. In *IEEE Proceedings of Electronic Components and Technology Conference*, pages 351 – 357, 2011.

[74] C. Y. Liu, C. Chen, and K. N. Tu. Electromigration in Sn-Pb solder strips as a function of alloy composition. *Journal of Applied Physics*, 88(10):5703 – 5709, 2000.

[75] M. Lu, P. Lauro, D.-Y. Shih, R. Polastre, C. Goldsmith, D. W. Henderson, H. Zhang, and M. G. Cho. Comparison of electromigration performance for Pb-free solders and surface finishes with Ni UBM. In *IEEE Proceedings of Electronic Components and Technology Conference*, pages 360 – 365, 2008.

[76] M. Lu, D.-Y. Shih, P. Lauro, C. Goldsmith, and D. W. Henderson. Effect of Sn grain orientation on electromigration degradation mecha-

nism in high Sn-based Pb-free solders. *Applied Physics Letters*, 92(21):211909, 2008.

[77] M. Lu, D.-Y. Shih, P. Lauro, S. Kang, C. Goldsmith, and S.-K. Seo. The effects of Ag, Cu compositions and Zn doping on the electromigration performance of Pb-free solders. In *IEEE Proceedings of Electronic Components and Technology Conference*, pages 922–929, 2009.

[78] J. Maria, B. Dang, S. L. Wright, C. K. Tsang, P. Andry, R. Polastre, Y. Liu, L. Wiggins, and J. U. Knickerbocker. 3D chip stacking with 50 µm pitch lead-free micro-C4 interconnections. In *IEEE Proceedings of Electronic Components and Technology Conference*, pages 268 – 273, 2011.

[79] T. B. Massalski, J. L. Murray, L. H. Bennett, and H. Baker. *Binary alloy phase diagrams*. Number 2. American Society for Metals, 1986.

[80] R. J. McCabe and M. E. Fine. Athermal and thermally activated plastic flow in low melting temperature solders at small stresses. *Scripta materialia*, 39(2):189 – 195, 1998.

[81] Z. Mei, M. Ahmad, M. Hu, and G. Ramakrishna. Kirkendall voids at Cu/solder interface and their effects on solder joint reliability. In *IEEE Proceedings of Electronic Components and Technology Conference*, pages 415 – 420, 2005.

[82] Z. Mei, A. J. Sunwoo, and J. W. Morris. Analysis of low-temperature intermetallic growth in copper-tin diffusion couples. *Metallurgical*

Transactions A, 23(3):857 – 864, 1992.

[83] R. von Meibom and E. Rupp. Elektronenbeugung in weiten winkeln. *Zeitschrift fr Physik*, 82(11-12):690 – 696, 1933.

[84] N. Metropolis, A. W. Rosenbluth, M. N. Rosenbluth, A. H. Teller, and E. Teller. Equation of state calculations by fast computing machines. *The Journal of Chemical Physics*, 21:1087, 1953.

[85] L. F. Miller. Controlled collapse reflow chip joining. *IBM Journal of Research and Development*, 13(3):239 – 250, 1969.

[86] M. Onishi and H. Fujibuchi. Reaction-diffusion in the Cu-Sn system. *Transactions JIM*, 16:539 – 547, 1975.

[87] A. Paul, C. Ghosh, and W. J. Boettinger. Diffusion parameters and growth mechanism of phases in the Cu-Sn system. *Metallurgical and Materials Transactions A*, 42(4):952 – 963, 2011.

[88] M. Pharr, K. Zhao, Z. Suo, F.-Y. Ouyang, and P. Liu. Concurrent electromigration and creep in lead-free solder. *Journal of Applied Physics*, 110(8):083716, 2011.

[89] K. J. Puttlitz and K. A. Stalter. *Handbook of Lead-Free Solder Technology for Microelectronic Assemblies*. Dekker Mechanical Engineering. Taylor & Francis, 2004.

[90] P. Ramm, A. Klumpp, J. Weber, N. Lietaer, M. Taklo, W. De Raedt, T. Fritzsch, and P. Couderc. 3D integration technology: Status and application development. In *IEEE Proceedings of the ESSCIRC*, pages 9 – 16, 2010.

[91] K. Sakuma, K. Sueoka, S. Kohara, K. Matsumoto, H. Noma, T. Aoki, Y. Oyama, H. Nishiwaki, P. S. Andry, C. K. Tsang, et al. IMC bonding for 3D interconnection. In *IEEE Proceedings of Electronic Components and Technology Conference*, pages 864 – 871, 2010.

[92] C. Schmetterer, H. Flandorfer, K. W. Richter, U. Saeed, M. Kauffman, P. Roussel, and H. Ipser. A new investigation of the system Ni-Sn. *Intermetallics*, 15(7):869 – 884, 2007.

[93] S.-K. Seo, S. K. Kang, D.-Y. Shih, and H. M. Lee. The evolution of microstructure and microhardness of Sn-Ag and Sn-Cu solders during high temperature aging. *Microelectronics Reliability*, 49(3):288 – 295, 2009.

[94] T. Shoji, M. Fujiyoshi, K. Sato, K. N. Tu, et al. Impact reliability of solder joints. In *IEEE Proceedings of Electronic Components and Technology Conference*, volume 1, pages 668 – 674, 2004.

[95] W. Soboyejo. *Mechanical Properties of Engineered Materials*. Taylor & Francis, 2002.

[96] H.-Y. Son, S.-K. Noh, H.-H. Jung, W.-S. Lee, J.-S. Oh, and N.-S. Kim. Reliability studies on micro-bumps for 3-D TSV integration. In *IEEE Proceedings of Electronic Components and Technology Conference*, pages 29 – 34, 2013.

[97] K. Subramanian. *Lead-free Solders: Materials Reliability for Electronics*. Wiley Series in Materials for Electronic & Optoelectronic Applications. Wiley, 2012.

[98] Z. Suo, D. V. Kubair, A. G. Evans, D. R. Clarke, and V. K. Tolpygo. Stresses induced in alloys by selective oxidation. *Acta Materialia*, 51(4):959 – 974, 2003.

[99] A. Syed, K. Dhandapani, R. Moody, L. Nicholls, and M. Kelly. Cu pillar and μ-bump electromigration reliability and comparison with high Pb, SnPb, and SnAg bumps. In *IEEE Proceedings of Electronic Components and Technology Conference*, pages 332 – 339, 2011.

[100] C. M. Tan and F. He. 3D circuit model for 3D IC reliability study. In *International Conference on Thermal, Mechanical and Multi-Physics simulation and Experiments in Microelectronics and Microsystems*, pages 1 – 7, 2009.

[101] A. Tarantola. *Inverse problem theory: Methods for data fitting and model parameter estimation*. Elsevier Science, 2002.

[102] K. N. Tu. Interdiffusion and reaction in bimetallic Cu-Sn thin films. *Acta Metallurgica*, 21(4):347 – 354, 1973.

[103] K. N. Tu. *Solder Joint Technology: Materials, Properties, and Reliability*. Springer Series in Materials Science. Springer London, Limited, 2007.

[104] K. N. Tu, H.-Y. Hsiao, and C. Chen. Transition from flip chip solder joint to 3D IC microbump: Its effect on microstructure anisotropy. *Microelectronics Reliability*, 2012.

[105] K. N. Tu and R. D. Thompson. Kinetics of interfacial reaction in bimetallic Cu-Sn thin films. *Acta Metallurgica*, 30(5):947 – 952, 1982.

[106] A. VanBeek, A. Stolk, and J. J. VanLoo. Multiphase diffusion in the systems Fe-Sn and Ni-Sn. *Zeitschrift fur Metallkunde*, 73(7):439 – 444, 1982.

[107] Y. Wang, K.-H Lu, V. Gupta, L. Stiborek, D. Shirley, S.-H. Chae, J. Im, and P. S. Ho. Effects of Sn grain structure on the electromigration of Sn-Ag solder joints. *Journal of Materials Research*, 27(8):1131–1141, 2012.

[108] L. Xie, W. K. Choi, C. S. Premachandran, C. S. Selvanayagam, K. W. Bai, Y. Z. Zeng, S. C. Ong, E. Liao, A. Khairyanto, V. N. Sekhar, et al. Design, simulation and process optimization of AuInSn low temperature TLP bonding for 3D IC stacking. In *IEEE Proceedings of Electronic Components and Technology Conference*, pages 279 – 284, 2011.

[109] D. C. Yeh and H. B. Huntington. Extreme fast-diffusion system: Nickel in single-crystal tin. *Physical Review Letters*, 53(15):1469 – 1472, 1984.

[110] L. Yina and P. Borgesen. On the root cause of kirkendall voiding in Cu_3Sn. *J. Mater. Res.*, 26(3):455 – 466, 2011.

[111] A. Yu, J. H. Lau, S. W. Ho, A. Kumar, W. Y. Hnin, D.-Q. Yu, M. C. Jong, V. Kripesh, D. Pinjala, and D.-L. Kwong. Study of 15 µm pitch solder microbumps for 3D IC integration. In *IEEE Proceedings of Electronic Components and Technology Conference*, pages 6 – 10, 2009.

[112] K. Zeng and K. N. Tu. Six cases of reliability study of Pb-free solder joints in electronic packaging technology. *Materials Science and Engineering: R: Reports*, 38(2):55 – 105, 2002.

[113] C.-J. Zhan, C.-C. Chuang, J.-Y. Juang, S.-T. Lu, and T.-C. Chang. Assembly and reliability characterization of 3D chip stacking with 30 µm pitch lead-free solder micro bump interconnection. In *IEEE Proceedings of Electronic Components and Technology Conference*, pages 1043 – 1049, 2010.

[114] C.-J. Zhan, J.-Y. Juang, Y.-M. Lin, Y.-W. Huang, K.-S. Kao, T.-F. Yang, S.-T. Lu, J. H. Lau, T.-H. Chen, R. Lo, et al. Development of fluxless chip-on-wafer bonding process for 3D IC chip stacking with 30 µm pitch lead-free solder micro bumps and reliability characterization.

In *IEEE Proceedings of Electronic Components and Technology Conference*, pages 14 – 21, 2011.

[115] W. Zhang, B. D. P. Limaye, A. L. Manna, P. Soussan, and E. Beyne. Ni/Cu/Sn bumping scheme for fine-pitch micro-bump connections. In *IEEE Proceedings of Electronic Components and Technology Conference*, pages 109 – 113, 2011.

[116] X. Zhang. *Chip-Package Interaction (CPI) and its Impact on the Reliability of Flip Chip Packages*. PhD thesis, University of Texas at Austin, 2009.

[117] K. Zhao, M. Pharr, Q. Wan, W. L. Wang, E. Kaxiras, J. J. Vlassak, and Z. Suo. Concurrent reaction and plasticity during initial lithiation of crystalline silicon in lithium-ion batteries. *Journal of The Electrochemical Society*, 159(3):A238 – A243, 2012.

[118] B. Zhou, T. R. Bieler, T.-K. Lee, and K.-C. Liu. Crack development in a low-stress PBGA package due to continuous recrystallization leading to formation of orientations with [001] parallel to the interface. *Journal of Electronic Materials*, 39(12):2669–2679, 2010.